Title
Hyperdynamic Spatiotemporal Cerebral Dynamics in Response to Cardiac Arrest and Resuscitation

Permalink
https://escholarship.org/uc/item/01r9g9jw

Author
Crouzet, Christian

Publication Date
2018

UNIVERSITY OF CALIFORNIA,
IRVINE

Hyperdynamic Spatiotemporal Cerebral Dynamics in Response to Cardiac Arrest and Resuscitation

DISSERTATION

submitted in partial satisfaction of the requirements
for the degree of

DOCTOR OF PHILOSOPHY

in Biomedical Engineering

by

Christian Jean-Paul Crouzet

Dissertation Committee:
Professor Bernard Choi, Chair
Professor Bruce J. Tromberg
Professor Yama Akbari

2018

DEDICATION

To my parents for giving me the foundation to succeed

To Sister Catalina for giving me a passion for science

To Jasmine for always being there and supporting me

TABLE OF CONTENTS

LIST OF FIGURES

LIST OF TABLES

ACKNOWLEDGMENTS

I would like to thank my family, especially my parents, mom and papa (Shelly and Christian), and my siblings, Chantal and Pierre. My parents have instilled in me habits of hard work and perseverance to enable my journey through graduate school. They have continually been loving and encouraging with unwavering support. I would also like to thank my wonderful wife, Jasmine, for putting up with me, keeping me going, and always believing that I can succeed.

To my friends that I have grown to know at UCI. I would especially like to thank the morning basketball crew for allowing me to use my body, stay in somewhat decent shape, and rest my mind. Specifically, I would like to thank Ben Lertsakdadet, Griffin Lentsch, Robert Wilson, Sarkis Daglian, Hector Lemon, Lee Swindlehurst, and Edwin Amenta for continually playing. I would also like to thank our coed BME intramural flag football team that won two championships. Especially the girls who played, including Jessica Hsieh, Esther Chen, Frances McWhorter, Caitlin Regan, and Ellen Hong.

I would like to acknowledge my advisor, Dr. Bernard Choi. From the moment I met Dr. Choi when I was an undergraduate student and throughout my graduate studies, I could not have asked for a more supportive, positive, encouraging, and knowledgeable advisor. Dr. Choi has let me explore many different research interests and expand my scientific understanding. From academics to my personal life, Dr. Choi has always been there and provided his expert guidance.

I would also like to acknowledge my committee members Dr. Bruce Tromberg and Dr. Yama Akbari. Dr. Tromberg has a never ending reach across time and space that is incredible. I appreciate the never ending questions that Dr. Tromberg asks to test one's intellectual capabilities and critical thinking on the spot. Dr. Akbari is a go-getting neurointensivist that continually brings his passion and excitement to each and every interaction.

Furthermore, I would like to acknowledge Dr. Akabari's lab. Specifically, I would like to thank Afsheen Bazrafkan, Dr. Niki Maki, and Dr. Maryam Farahabadi for their time, energy, and expertise in performing all the surgeries for our experiments. Furthermore, I would like to thank Donald Lee for his help in EEG signal analysis and scientific discussions.

I would like to thank all of my colleagues at the Beckman Laser Institute and the Microvasculature Therapeutics and Imaging (MTI) Lab for creating a wonderful work environment. Specifically, I would like to thank Dr. Robert Wilson for working in the trenches and having countless hours of discussion. I would also like to thank Dr. Caitlin Regan for challenging me to think and push myself, Ben Lertsakdadet for continued questions to examine data in different ways and being a great friend, Cody Dunn for bringing new and fresh youth, blood, and perspective to the lab, Dr. Bruce Yang for exuberant scientific and non-scientific discussions, and Dr. Sean White for always having an answer to my problems. Lastly, I would like to thank the entire MTI lab for listening to my lengthy lab presentations and providing feedback.

I would like to acknowledge the National Science Foundation for their generous financial support of my work through the Graduate Research Fellowship Program, which allowed me to freely pursue my interests.

I also thank the Optical Society of America for permission to include portions of Chapters 1 and 2 of my dissertation, which were originally published in Biomedical Optics Express. Financial support was provided by the National Science Foundation Graduate Research Fellowship Program (DGE-1321846), Associated Graduate Students, the NIH Laser Microbeam and Medical Program (P41 EB015890), the National Institute of Health R21 (EB024793), and the Arnold and Mabel Beckman Foundation.

CURRICULUM VITAE

Christian Jean-Paul Crouzet

2013	B.S., Biomedical Engineering, University of California, Irvine
2016	M.S., Biomedical Engineering, University of California, Irvine
2018	Ph.D., Biomedical Engineering, University of California, Irvine

PUBLICATIONS

J.1. John Quan M. Nguyen, **Christian Crouzet**, Tuan Mai, Kathleen Riola, Daniel Uchitel, Lih-Huei Liaw, Nicole Bernal, Adrien Ponticorvo, Bernard Choi, Anthony J. Durkin, *Spatial frequency domain imaging of burn wounds in a preclinical model of graded burn severity*, Journal of Biomedical Optics, 18(6), 066010, 2013.

J.2. Robert H. Wilson, Kyle P. Nadeau, Frank B. Jaworski, Rebecca Rowland, John Q. Nguyen, **Christian Crouzet**, Rolf B. Saager, Bernard Choi, Bruce J. Tromberg, and Anthony J. Durkin, *Quantitative short-wave infrared (SWIR) multispectral imaging of in-vivo tissue optical properties*, Journal of Biomedical Optics, 19(8), 86011, 2014.

J.3. **Christian Crouzet**, John Q. Nguyen, Adrien Ponticorvo, Nicole P. Bernal, Anthony J. Durkin, and Bernard Choi, *Acute discrimination between superficial-partial and deep-partial thickness burn injuries in a preclinical model with laser speckle imaging*, Burns, 41(5), 1058-1063, 2015.

J.4. Bruce Yang, Owen Yang, John Guzman, Paul Nguyen, **Christian Crouzet**, Kathryn E. Osann, Kristen M. Kelly, J. Stuart Nelson, and Bernard Choi, *Intraoperative, Real-Time Monitoring of Blood Flow Dynamics Associated With Laser Surgery of Port Wine Stain Birthmarks*, Lasers in Surgery and Medicine, 47(6), 469-475, 2015.

J.5. Patrick Lo, **Christian Crouzet**, Vitaly Vasilevko, and Bernard Choi, *Visualization of Microhemorrhages with Optical Histology in Mouse Model of Cerebral Amyloid Angiopathy*, Microvascular Research, 105, 109-113, 2016.

J.6. **Christian Crouzet**, Robert H. Wilson, Afsheen Bazrafkan, Maryam H. Farahabadi, Donald Lee, Juan Alcocer, Bruce J. Tromberg, Bernard Choi, and Yama Akbari, *Cerebral Blood Flow is decoupled from blood pressure and linked to EEG bursting after resuscitation from cardiac arrest,* Biomedical Optics Express, 7(11), 4660-4673, 2016.

J.7. Robert H. Wilson, **Christian Crouzet**, Mohammad Torabzadeh, Afsheen Bazrafkan, Maryam H. Farahabadi, Babak Jamasian, Dishant Donga, Juan Alcocer, Shuhab M. Zaher, Bernard Choi, Yama Akbari, and Bruce J. Tromberg, *High-speed spatial frequency domain imaging of rat cortex detects dynamic optical and physiological properties following cardiac arrest and resuscitation,* Neurophotonics, 4(4), 045008, 2017.

J.8. Ben Lertsakdadet, Bruce Y. Yang, Cody E. Dunn, Adrien Ponticorvo, **Christian Crouzet**, Nicole Bernal, Anthony J. Durkin, and Bernard Choi, *Correcting for Motion Artifact in Handheld Laser Speckle Images*, Journal of Biomedical Optics 23(3), 1-7, 2018.

J.9. Cody Dunn, Ben Lertsakdadet, **Christian Crouzet**, Adrian Bahani, and Bernard Choi, *A comparison of speckleplethysmographic (SPG) and photoplethysmographic (PPG) imaging by Monte Carlo simulations and in vivo measurements*, Biomedical Optics Express, 9(9), 4306-4316, 2018.

J.10. **Christian Crouzet**, Robert H. Wilson, Donald Lee, Afsheen Bazrafkan, Bruce J. Tromberg, Yama Akbari, and Bernard Choi, *Influence of cerebral blood flow and femoral artery pulsatility on short-term neurological outcome following resuscitation from cardiac arrest in a rat model*, In preparation

CONFERENCE PRESENTATIONS AND PROCEEDINGS

C.1. John Quan M. Nguyen, Tuan Mai, **Christian Crouzet**, Kathleen Riola, Daniel Uchitel, Lih-Huei Liaw, Nicole Bernal, Adrien Ponticorvo, Bernard Choi, Anthony J. Durkin, *Quantitative longitudinal measurement in a rat model of controlled burn severity using spatial frequency domain imaging* in Photonic Therapeutics and Diagnostics IX, Proceedings of SPIE Vol. 8565, 2013. (Conference Proceeding)

C.2. Patrick Lo, **Christian Crouzet**, Vitaly Vasilevko, and Bernard Choi, *Visualization of Microhemorrhages with Optical Histology in Mouse Model of Cerebral Amyloid Angiopathy*, in Clinical and Translational Neurophotonics at SPIE Photonics West, California, February 2016.

C.3. Robert H. Wilson, **Christian Crouzet**, Maryam H. Farahabadi, Afsheen K. Bazrafkan, Donald Lee, Anthony J. Durkin, Bernard Choi, Yama Akbari, and Bruce J. Tromberg, *Multimodal optical platform for functional monitoring of cerebral response to cardiac arrest and resuscitation*, in Optical Techniques in Neurosurgery, Brain Imaging, and Neurobiology at SPIE Photonics West, California, February 2016.

C.4. Adrien Ponticorvo, Rebecca A. Rowland, Bruce Yang, Ben Lertsakdadet, **Christian Crouzet**, Nicole Bernal, Bernard Choi, and Anthony J. Durkin, *Quantitative assessment of* *graded burn wounds using a commercial and research grade laser speckle imaging (LSI) system*, in Photonics in Dermatology and Plastic Surgery at SPIE Photonics West, California, January 2017.

C.5. Robert H. Wilson, **Christian Crouzet**, Afsheen Bazrafkan, Maryam H. Farahabadi, Mohammad Torabzadeh, Juan Alcocer, Tin Dinh, Babak Jamasian, Dishant Donga, Donald Lee, Anthony J. Durkin, Bernard Choi, Bruce J. Tromberg, and Yama Akbari, *Multimodal optical imaging platform enables spatiotemporal mapping of cerebral blood flow and metabolism during cardiac arrest and resuscitation*, in Clinical and Translational Neurophotonics at SPIE Photonics West, California, January 2017.

C.6. Ben Lertsakdadet, Ryan Farraro, Bruce Yang, **Christian Crouzet**, Adrien Ponticorvo, Anthony J. Durkin, Bernard Choi, *Handheld laser speckle imaging for point-of-care blood-flow measurements*, in Basic Science and Translational Research at ASLMS Annual Conference, California, April 2017.

C.7. Robert H. Wilson, **Christian Crouzet**, Mohammad Torabzadeh, Afsheen Bazrafkan, Yama Akbari, Bernard Choi, and Bruce J. Tromberg, *Spatio-temporal propagation of changes in cerebral blood flow and tissue scattering in response to cardiac arrest and resuscitation*, in Neural Imaging and Sensing at SPIE Photonics West, California, January 2018.

C.8. **Christian Crouzet**, Robert H. Wilson, Afsheen Bazrafkan, Juan Alcocer, Bruce J. Tromberg, Yama Akbari, and Bernard Choi, *Global cerebral ischemia induces spatial propagation of cerebral blood flow during cardiac arrest and after resuscitation,* in Neural Imaging and Sensing at SPIE Photonics West, California, January 2018.

POSTER PRESENTATIONS

P.1. **Christian Crouzet**, John Quan Nguyen, Tuan Mai, Kathleen Riola, Anthony J. Durkin, and Bernard Choi, *Preclinical Model of Burn Wound Severity Using Laser Speckle Imaging*, poster presented at University of California, Irvine Undergraduate Research Symposium, May 2013.

P.2. Bernard Choi, Bruce Yang, Owen Yang, Hyeoungho Bae, Yu-Shan Hsiao, **Christian Crouzet**, John Nguyen, Sari Mahon, Matthew Brenner, Anthony Durkin, Pai Chou, *Camera-based optical imaging of tissue blood flow,* poster presented at Military Health System Research Symposium, Florida, August 2013.

P.3. John Quan M. Nguyen, **Christian Crouzet**, Tuan Mai, Kathleen Riola, Daniel Uchitel, Lih-Huei Liaw, Nicole Bernal, Adrien Ponticorvo, Bernard Choi, Anthony J. Durkin, *Non-*

invasive assessment of burn wound severities in an acute rat model, poster presented at Military Health System Research Symposium, Florida, August 2013.

P.4. **Christian Crouzet**, Robert H. Wilson, Maryam H. Farahabadi, Afsheen Bazrafkan, Bruce J. Tromberg, Yama Akbari, Bernard Choi, *Monitoring acute cerebral blood flow dynamics during cardiac arrest and resuscitation with laser speckle imaging*, poster presented at SPIE/NIH Biophotonics from Bench to Bedside, Maryland, September 2015.

P.5. Robert H. Wilson, **Christian Crouzet**, Afsheen Bazrafkan, Maryam H. Farahabadi, Juan Alcocer, Babak Jamasian, Danny Siu, Lauren Lee, Dishant Donga, Donald Lee, Anthony J. Durkin, Bernard Choi, Bruce J. Tromberg, and Yama Akbari, *Concurrent assessment of cerebral blood flow, oxygenation, and electrical activity following cardiac arrest and cardiopulmonary resuscitation*, poster presented at 2016 Pathways to Cures: Clinical Translational Research Day at University of California, Irvine, June 2016.

P.6. **Christian Crouzet**, Robert H. Wilson, Maryam H. Farahabadi, Afsheen Bazrafkan, Donald Lee, Juan Alcocer, Bruce J. Tromberg, Yama Akbari, and Bernard Choi, *Cerebral blood flow is linked to EEG bursting after cardiac arrest and resuscitation*, poster presented at Lasers in Medicine and Biology, Gordon Research Conference, Vermont, July 2016.

P.7. **Christian Crouzet**, Robert H. Wilson, Maryam H. Farahabadi, Afsheen Bazrafkan, Donald Lee, Juan Alcocer, Bruce J. Tromberg, Yama Akbari, and Bernard Choi, *Cerebral blood flow is linked to EEG bursting after cardiac arrest and resuscitation*, poster presented at Biomedical Engineering Society 2016 Annual Meeting, Minnesota, October 2016.

P.8. **Christian Crouzet**, Robert H. Wilson, Afsheen Bazrafkan, Shuhab M. Zaher, Bruce J. Tromberg, Yama Akbari, and Bernard Choi, *Spatial propagation of cerebral hemodynamics during and after resuscitation from cardiac arrest*, poster presented at Engineering Conferences International: Advances in Optics for Biotechnology, Medicine and Surgery XV, Colorado July 2017.

P.9. Ben Lertsakdadet, Bernard Choi, Anthony J. Durkin, Rebecca Rowland, **Christian Crouzet**, Cody E. Dunn, Adrien Ponticorvo, Bruce Y. Yang, and Nicole Bernal, *In-vitro validation and quantitative measurements of graded burn wounds on a porcine model using handheld laser speckle imaging*, poster presented at Engineering Conferences International: Advances in Optics for Biotechnology, Medicine and Surgery XV, Colorado July 2017.

P.10. Cody E. Dunn, Ben Lertsakdadet, **Christian Crouzet**, Adrian Bahani, and Bernard Choi, *A comparison of speckleplethysmographic imaging (SPGI) and photoplethysmographic imaging (PPGI) by in silico and in vivo measurements*, poster presented at Lasaers in Medicine and biology, Gordon Research Conference, Maine, July 2018.

NOTABLE AWARDS AND HONORS

National Science Foundation – Graduate Research Fellowship Program (2015)

ABSTRACT OF THE DISSERTATION

Hyperdynamic Spatiotemporal Cerebral Dynamics
in Response to Cardiac Arrest and Resuscitation

By

Christian Jean-Paul Crouzet

Doctor of Philosophy in Biomedical Engineering

University of California, Irvine, 2018

Professor Bernard Choi, Chair

Annually, over 550,000 people in the United States suffer cardiac arrest (CA) and initial survival rates remain low (10-30%). Approximately 85 to 90% of survivors have impaired cognitive function, which leads to decreased quality of life for survivors, increased burden on caregivers, and direct costs of over $6 billion/year. To improve neurological recovery and understand how the brain recovers following CA, a critical need exists to investigate physiological processes that impact the brain. In collaboration with Dr. Yama Akbari's lab, we developed a multi-modal platform with high temporal (10s of milliseconds) and spatial (~50μm) resolution. The platform combined laser speckle imaging (LSI), arterial blood pressure (ABP), and electroencephalography (EEG) to monitor cerebral blood flow (CBF), peripheral blood pressure, and brain electrophysiology, respectively. We applied this platform to an asphyxial CA and resuscitation preclinical model established in Dr. Akbari's lab and characterized the hyperdynamic spatiotemporal cerebral dynamics that occur before, during, and after asphyxial CA and resuscitation.

The beginning of neurological recovery post-CA is the moment at which brain electrical activity resumes. We assessed the temporal evolution of CBF prior to this time

point, and found two distinct CBF phases. The first phase is a hyperemic (increase in CBF) period that occurs 5-10min after resuscitation, which is followed by a period of prolonged, stabilized hypoperfusion (decrease in CBF). We found that brain electrical activity resumes after the CBF hyperemic period, but before CBF stabilizes hypoperfused. CBF and MAP data were then used to develop an empirical model to predict when brain electrical activity resumes to within 10% accuracy. The link between hemodynamics and the resumption of brain electrical activity, suggests that clinicians may be able to utilize and develop hemodynamic-altering therapeutics that modify the beginning of neurological recovery.

Next, we analyzed pulsatile CBF and femoral ABP waveforms in response to CA and resuscitation. Pulsatile blood flow is important due to its impact on oxygen uptake, vascular tone, and cellular metabolism. Our study revealed that CBF pulsatility is altered significantly from baseline within 2h after resuscitation, but ABP pulsatility changes little. Interestingly, ABP pulsatility and not CBF pulsatility correlates with short-term neurological outcome. These results suggest that simultaneous monitoring of CBF and ABP pulsatility is necessary, and therapeutic modulation of pulsatility post-CA may lead to changes in neurological outcome.

Lastly, we analyzed spatiotemporal CBF changes during three hyperdynamic periods: (1) entering CA, (2) within 5min after resuscitation, and (3) from hyperemia to hypoperfusion (i.e., 5 to 20min after resuscitation). Spreading CBF waves were visualized during each phase. We found that an increase in total CBF prior to the onset of spreading wave (1) was associated with *worse* neurological outcome, waves (1) and (3) propagated in opposite directions, and waves (2) and (3) resembled a well-known phenomenon called

cortical spreading depression. These spatiotemporal characteristics are complex, yet may have clinical importance to neurological outcome.

Collectively, these findings highlight the complex nature of the hyperdynamic cerebral response to CA and resuscitation. The multi-modal platform and results suggest a novel therapeutic approach involving modulation of hemodynamics during hyperdynamic periods of CA may improve neurological outcome.

INTRODUCTION

Annually, over 550,000 people in the United States suffer cardiac arrest (CA) while initial survival rates remain poor (10-30%)[1]. Approximately 85 to 90% of survivors have impaired cognitive function, which leads to decreased quality of life for survivors, increased burden on caregivers, and direct costs of over $6 billion/year[1,2]. CA causes inadequate cerebral blood flow (CBF), which results in a cascade of events that lead to neuronal cell death within three minutes[3–5]. Reperfusion after resuscitation from CA leads to further neuronal damage, due to reactive oxygen species and potential decoupling between CBF and metabolism[6]. Figure 0.1 is a schematic that describes neuronal injury during periods of ischemia (absence of CBF) and following resuscitation (CBF reperfusion).

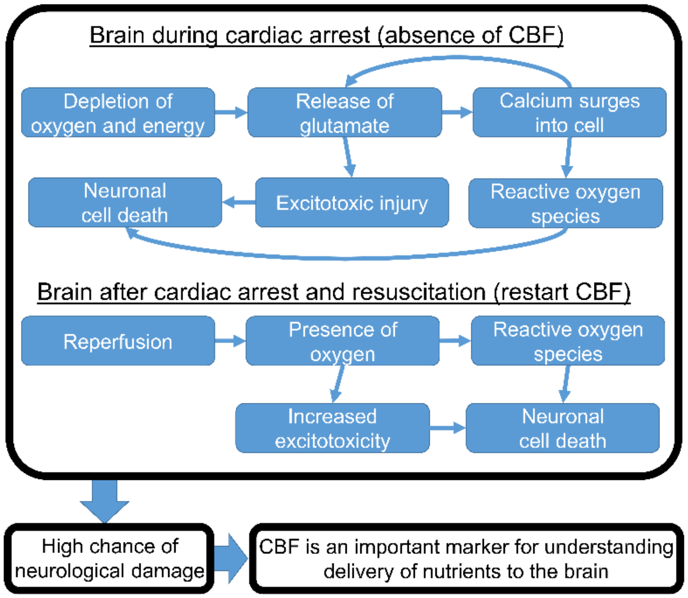

Figure 0.1: Role of CBF in neuronal cell death. Periods of minimal or absent CBF lead to a lack of oxygen and therefore loss of ATP production. This leads to a release of the excitotoxic neurotransmitter glutamate into the extracellular space, which leads to excitoxic injury and calcium surging into the cell. Calcium surging into the cell leads to a feedback loop that further releases more glutamate into the extracellular space. Free radicals lead to oxidative stress. Upon successful resuscitation and resumption of CBF, the presence of oxygen leads to increased excitotoxicity and acts as a substrate for free radicals that lead to more neuronal injury. The periods of absent CBF and CBF reperfusion both lead to a high chance of neurological damage, and CBF is critical to understand how nutrients, including oxygen are delivered to the brain.

In patients, monitoring brain electrical activity is the most common examination method, other than clinical evaluation[7]. Numerous studies have extensively examined brain electrophysiology through the use of electroencephalography (EEG) following resuscitation from CA. The evolution of the EEG signal during ischemic periods and following reperfusion, and their relationship to neurological outcome is outlined in Figure 0.2. EEG studies have made advances at understanding the relationship between brain electrical activity and neurological outcome[8–12]. Furthermore, these studies have investigated normothermic, hypothermic and hyperthermic treatments that resulted in hypothermic treatments leading to better neurological outcome[8,13–15]. However, the sole use of EEG limits the understanding between the interplay between cerebral hemodynamics and electrophysiology.

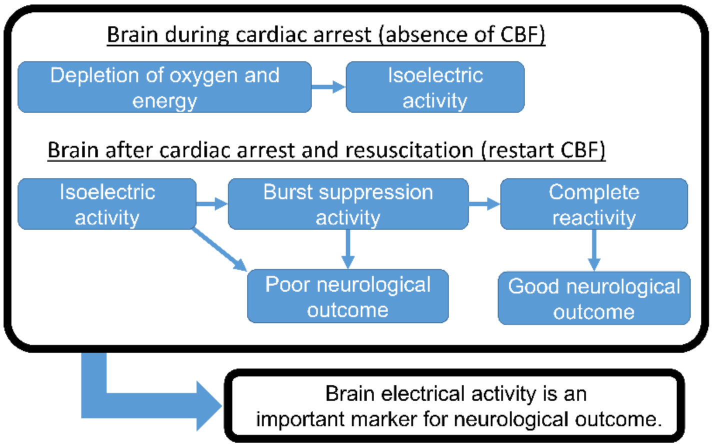

Figure 0.2: Evolution of EEG signal during and after CA. In the absence of CBF, the brain is depleted of oxygen and energy which leads to a silent EEG signal. After CBF reperfusion, the EEG signal may remain silent, which leads to poor neurological outcome, or can transition into burst suppression activity. If the EEG signal remains in burst suppression activity, poor neurological outcome is the result. However, if the EEG signal transitions to complete reactivity, the patient will typically have good neurological outcome, which shows the importance of monitoring brain electrical activity through EEG.

A number of studies have also examined cerebral hemodynamic changes in response to CA and resuscitation, using a variety of different technologies. These technologies include Doppler techniques[16–18], positron emission tomography (PET)[19,20], and magnetic resonance imaging (MRI)[21,22]. Hemodynamic studies, in particular with relation to CBF, have reported a hyperemic phase about 10min after resuscitation, followed by a stabilized hypoperfusion phase, before CBF steadily increases toward baseline over 24h[23]. Luxury reperfusion 24h after resuscitation has been reported to be associated with worse neurological outcome[24]. Although these technologies provide an overall, global view of brain hemodynamics, they are limited by their spatial and temporal (~5-30min) resolution to resolve hyperdynamic, spatiotemporal changes of entering CA and immediately after resuscitation.

Under normal conditions, the brain is highly regulated as CBF is constant over a wide range of mean arterial pressures (MAP)[25]. Typically, clinical monitoring does not perform direct measurement of CBF. However, after CA and resuscitation, CBF and MAP may become dysregulated[26], and a need for direct measurement of CBF becomes critical. Since MAP is a parameter clinicians depend on to indirectly monitor cerebral perfusion after resuscitation, there is a dire need to understand the relationship between CBF and MAP during periods of dysregulation.

To understand the complex neurovascular response to CA, a multimodal approach is needed to investigate the relationship between brain electrophysiology and hemodynamics, and peripheral blood pressure. The current lack of multimodal approaches hinder the development of new therapeutic strategies to improve neurological outcome after resuscitation from CA. Furthermore, the lack of high temporal resolution technologies limits the ability to identify therapeutic time windows that may improve neurological outcome following resuscitation from CA. Although previous studies have vastly expanded our understanding of brain functional dynamics following CA, they have two main shortcomings: 1) hemodynamic techniques have poor temporal resolution (~5–30min); and 2) lack of simultaneous multi-modal approaches to relate CBF, MAP, and brain electrophysiology.

To address these shortcomings, this work utilized a multi-modal instrument that combined laser speckle imaging (LSI), arterial blood pressure, and EEG to simultaneously and concurrently monitor CBF, peripheral blood pressure, and brain electrical activity before, during, and after CA and resuscitation with high temporal resolution (~20ms). Due to the multimodal approach, several key questions regarding the relationship between brain electrophysiology and hemodynamics, and their relationship to peripheral blood pressure have been investigated.

What are the temporal characteristics of CBF data and the resumption of EEG activity after resuscitation from CA (Chapter 1)?

Previous EEG studies have found that an isoelectric period occurs immediately after resuscitation, until bursting (defined as a sharp increase in EEG amplitude interspersed between isoelectric periods) begins. Furthermore, continuous brain electrical activity 24h post-ROSC is associated with improved neurological outcome[27]. However, few studies have examined the initial moment the brain transitions from a silence period to resumption of EEG activity after resuscitation from CA[28].

Previous CBF studies have observed different phases associated with CBF after resuscitation from CA [23]. The first phase is a hyperemic response immediately after resuscitation, followed by a stabilized hypoperfusion phase, and eventually a recovery back towards baseline where CBF remains hypo-perfused, returns to normal, or a secondary hyperemic phase occurs. However, studies have lacked the temporal resolution to quantify each phase in terms of time and magnitude.

The lack of temporal knowledge about the evolution of CBF phases and EEG data with respect to brain resumption after resuscitation from CA limits the opportunity to develop clinical interventions during the acute recovery period. In this chapter we characterized the time and magnitude of the hyperemic peak and stabilized hypoperfusion periods from the CBF data. Furthermore, we characterized the exact timing the resumption of EEG activity begins using the initial EEG burst. Later in Chapter 1, we use this information to develop a predictive algorithm relating the CBF data to the initial EEG burst.

Can we use CBF and MAP data to develop a predictive model for the resumption of EEG activity after resuscitation from CA (Chapter 1)?

Although CBF reperfusion occurs during resuscitation, the EEG signal typically remains silent for a period of time. The EEG signal can transition into burst suppression activity, which is the beginning of EEG recovery after CA. However, due to limited multimodal monitoring and poor hemodynamic temporal resolution, scientists and clinicians have been unable to understand how brain electrical activity resumes following resuscitation from CA, which hinders the development of interventions to help patients transition from EEG silence.

Using the multimodal platform of LSI, arterial blood pressure, and EEG we were able to better elucidate some of the mechanisms associated with the resumption of brain electrical activity after resuscitation from CA. Through the quantification of the temporal characteristics of the CBF data and initial EEG burst, we were able to investigate the role of hemodynamics on resuming brain electrical activity. We then were able to develop two models to predict the resumption of brain electrical activity using CBF and MAP data.

How does the pulsatile evolution of CBF and femoral artery blood pressure influence short-term neurological recovery (Chapter 2)?

Pulsatile blood flow is important due to its impact on oxygen uptake, vascular tone, and cellular metabolism. Studies have shown that pulsatile flow (compared to non-pulsatile flow) during cardiac bypass surgery and extracorporeal membrane life support (ECMO) is associated with improved neurological and physiological outcomes[29–32]. Furthermore, modulation of pulsatility through mechanically controlled devices is associated with reduced cerebrovascular resistance (CVR) and improved oxygen uptake during post-ischemic reperfusion, which can improve neurological outcome[33].

To better understand the relationship between pulsatility and neurological outcome following CA, several gaps in the knowledge base must be addressed. First, low frequency (<0.4Hz) studies have only examined survivors or non-survivors of CA, and not neurological function or outcome after CA[34,35]. Second, studies of the pulsatile waveform typically focus on CBF and not peripheral hemodynamics associated with the aorta or femoral artery. Third, the influence of CVR on CBF and the peripheral pulsatile waveform has not been investigated. Finally, clinical studies begin upon hospital admission followed by measurements on subsequent days after CA, and hence do not enable study of immediate pulsatile signal changes after resuscitation (during ischemia-induced hyperemia and hypoperfusion) and their relationship to neurological outcome.

To address these gaps, we used an established preclinical model of asphyxial CA (ACA) to continuously monitor pulsatile CBF and femoral arterial blood pressure (ABP) waveforms associated with the heartbeat. We used CBF and ABP data to obtain a measurement of CVR, and electroencephalography (EEG) to measure short-term neurological outcome 90min after resuscitation. Using these measurements, we quantified CBF and ABP pulsatility immediately after resuscitation and compared changes among different phases in the experiment. We also quantified the relationship between CBF and ABP pulsatility to CVR, and compared CBF and ABP pulsatility to short-term neurological outcome.

What are the spatiotemporal CBF changes during CA, immediately after resuscitation, and from the hyperemia to hypoperfusion phase (Chapter 3)?

Chapters 1 and 2 assessed the temporal evolution of cerebral blood flow (CBF), arterial blood pressure, and brain electrophysiology. Specifically, we examined how CBF evolved prior to the moment brain electrical activity resumes after resuscitation (Chapter 1)[36]. Furthermore, we examined the effects of pulsatile CBF and femoral arterial blood pressure (ABP) waveforms in response to CA and resuscitation, and how they affect short-term neurological outcome (Chapter 2). However, both these studies lacked the analysis of spatiotemporal CBF changes that occur before, during, and after CA and resuscitation.

Previous studies have shown that a wave of spreading depolarization (SD) occurs in rats and humans. These waves are caused by the breakdown of ion channels and are visualized using voltage-sensitive dyes and multiple DC and AC electrodes[37,38]. Furthermore, *in vitro* studies using optical intrinsic signal imaging (OISI) have shown SDs occur in brain sections[39]. However, to my knowledge, no study has reported visualization of spatial CBF changes that occur during SD in global ischemia models, which may be due to a lack of capable technologies or insufficient signal-to-noise.

SDs are important for a wide-range of different clinical applications. Not only do SDs occur during CA, but also during focal-ischemic stroke, traumatic brain injury, and migraines. In non-global ischemia studies, spatial changes in CBF have been reported that are characterized as a wave of increased CBF that is followed by a wave of decreasing CBF.

To determine if spatial CBF changes occurred in relation to ACA, we focused on three main time-periods based on our previous data: (1) during the same time interval that typical SDs occur, (2) immediately after resuscitation prior to the hyperemic peak, and (3) from the hyperemic peak to the stabilized hypoperfusion period.

CHAPTER 1: Cerebral blood flow is decoupled from blood pressure and linked to EEG bursting after resuscitation from cardiac arrest

This work was originally published in Biomedical Optics Express[36].

1.1 Abstract

In the present study, we developed a multi-modal instrument that combines laser speckle imaging, arterial blood pressure, and electroencephalography (EEG) to quantitatively assess cerebral blood flow (CBF), mean arterial pressure (MAP), and brain electrophysiology before, during, and after asphyxial cardiac arrest (CA) and resuscitation. Using the acquired data, we quantified the time and magnitude of the CBF hyperemic peak and stabilized hypoperfusion after resuscitation. Furthermore, we assessed the correlation between CBF and MAP before and after stabilized hypoperfusion. Finally, we examined when brain electrical activity resumes after resuscitation from CA with relation to CBF and MAP, and developed two empirical predictive models to predict when brain electrical activity resumes after resuscitation from CA. Our results show that: 1) more severe CA results in longer time to stabilized cerebral hypoperfusion; 2) CBF and MAP are coupled before stabilized hypoperfusion and uncoupled after stabilized hypoperfusion; 3) EEG activity (bursting) resumes after the CBF hyperemic phase and before stabilized hypoperfusion; 4) CBF predicts when EEG activity resumes for 5-min asphyxial CA, but is a poor predictor for 7-min asphyxial CA using a fixed predictive model; 5) CBF and MAP accurately predict when EEG activity resumes for 5- and 7-min asphyxial CA using a robust predictive model. Together, these novel findings highlight the importance of using multi-modal approaches to investigate CA recovery to better understand physiological processes and ultimately improve neurological outcome.

1.2 Introduction

According to the American Heart Association, over 500,000 Americans suffer a cardiac arrest (CA) per year[40]. Although resuscitation efforts have improved[41], poor neurological outcome is the leading cause of morbidity in CA survivors, and only 8.3% of out-of-hospital CA survivors have good neurological recovery[42,43]. To improve neurological outcome and understand how the brain recovers following CA, a critical need exists to investigate physiological processes that impact the brain, such as cerebral blood flow (CBF), arterial blood pressure, and brain electrophysiology.

Many clinical and preclinical studies have investigated the dynamics of brain physiology. These studies have used a multitude of techniques to examine cerebral blood flow and electrophysiology following CA, such as Doppler techniques[16–18], positron emission tomography (PET)[19,20], magnetic resonance imaging (MRI)[21,22], and electroencephalography (EEG)[8,9,11,44]. CBF studies have reported a hyperemic phase, followed by a stabilized hypoperfusion phase, before CBF steadily increases toward baseline over 24h[23]. A common metric clinicians use to determine if the brain receives an adequate amount of CBF is cerebral perfusion pressure (CPP)[45]. CPP is defined as the difference between mean arterial pressure (MAP) and intracranial pressure (ICP), which represents the pressure gradient that drives CBF. Studies have examined the impact that CBF autoregulation has on patient outcome[17], and the dysregulation of CBF from MAP after return of spontaneous circulation (ROSC) or resuscitation[26]. EEG studies have found that an isoelectric period occurs immediately after resuscitation, until bursting (defined as a sharp increase in EEG amplitude interspersed between isoelectric periods) begins. Furthermore, continuous brain electrical activity 24h post-ROSC is associated with improved neurological outcome[27]. Although these studies have vastly expanded our understanding of brain functional dynamics following CA, they have two main shortcomings: 1) hemodynamic techniques have poor temporal resolution (~5–30min); and 2) lack of simultaneous multi-modal approaches to relate CBF, MAP, and brain electrophysiology.

To address these shortcomings, we developed a multi-modal instrument design that combines laser speckle imaging (LSI), arterial blood pressure, and EEG to simultaneously acquire data before, during, and after CA and resuscitation. Due to the relatively high temporal resolution (~seconds) of our instrument, our results quantify the time and magnitude of the hyperemic peak and stabilized hypoperfusion post-ROSC. Furthermore, we assess the correlation between CBF and MAP before and after stabilized hypoperfusion. Finally, we show that initial EEG bursting begins after the CBF hyperemic phase and before stabilized hypoperfusion. We also show that one predictive model can accurately predict the initial EEG burst occurs for less severe CA, while a different and more robust predictive model performs equally well for different severities of CA. Collectively, our findings indicate the importance of using multi-modal approaches to better understand the physiological processes of CA recovery and ultimately improve neurological outcome.

1.3 Materials and Methods

1.3.1 Animal Model

We performed experiments on 16 male Wistar rats (351 ± 39g in mass). The asphyxial CA model and study protocol (no. 2013-3098) were approved in accordance with the Institutional Animal Care and Use Committee at University of California, Irvine. After applying the inclusion criterion that chest compressions lasted shorter than 1min, the final number of rats included for data analysis was 13 (n = 7, 5-min asphyxia; and n = 6, 7-min asphyxia).

1.3.2 Animal Preparation and Surgery

We developed an asphyxial CA model similar to those used in previous studies[8,21]. Rats were calorically restricted the night prior to CA experiments. On the day of CA, rats were anesthetized and intubated using a 14-gauge endotracheal tube (B. Braun Melsungen AG, Melsungen, Germany), which was connected to a TOPO mechanical ventilator (Kent Scientific, Torrington, CT) and isoflurane vaporizer. During surgery, isoflurane was maintained at 2% and ventilation settings were maintained at 70 breaths per min (BPM), with 12–14cmH_2O peak inspiration pressure (PIP) and 3cmH_2O peak end expiratory pressure (PEEP) in a 50%/50% N_2/O_2 mixture at 2LPM. Rectal temperature (Kent Scientific, Torrington, CT) was continuously measured and maintained between 36.5 and 37.5^{o}C. The rat was then mounted onto a stereotaxic frame (Kopf Instruments, Tujunga, CA) to stabilize the head position for surgery.

A midline incision was performed over the scalp and the scalp retracted to expose the skull for EEG electrode implantation (Plastics One Inc., Roanoke, VA). Two frontal electrodes were implanted (2mm anterior and 2.5mm lateral to bregma), and one electrode was implanted over the visual cortex (5.5mm posterior to bregma and 4mm left of bregma). A reference electrode was placed 3mm posterior to lambda. Following the implantation of EEG electrodes, a 4mm x 6mm craniectomy was performed over the right sensory and visual cortex using a power micro-drill (Roboz Surgical Instrument Co., Gaithsburg, Maryland) to enable subsequent optical imaging. Saline was applied periodically to ensure the brain stayed hydrated. Following the craniectomy, the femoral artery and vein were cannulated using PE-50 tubing (Becton, Dickinson and Company, Franklin Lakes, NJ). Invasive arterial blood pressure was measured continuously using a transducer (CWE Inc., Ardmore, PA). Baseline arterial blood gas (ABG) measurements (Abaxis, Union City, CA) were obtained within 30min prior to initiation of asphyxia.

1.3.3 Asphyxial Cardiac Arrest and Resuscitation

A timeline of the CA experiments is depicted in Figure 1.1A. At experiment start time, rats were placed on 100% O_2, while isoflurane was reduced to 0.5–1% to prepare for anesthesia wash out. At 2min into the experiment, room air (21% O_2) was given, isoflurane was turned off to wash out anesthesia, and neuromuscular blockade initiated with 1mL of intravenous Vecuronium (2mg/kg), flushed with 1mL of heparinized saline. At 5min, asphyxia was initiated by turning the ventilator off and tubing clamped. Rats were subjected to a period of either 5- or 7-min asphyxia. CA was defined as a systolic blood pressure <30mmHg and pulse pressure <10mmHg. Thirty seconds prior to chest compressions, mechanical ventilation was re-initiated at 100% O_2 with respiratory rate of 75–85BPM, PIP of 17.5–18.5 cmH_2O, and PEEP of 3cmH_2O at 2.5LPM. Epinephrine (0.01mg/kg) and sodium bicarbonate (1mmol/kg) were administered intravenously, followed by 2mL of heparinized saline prior to initiation of chest compressions. Chest compressions continued until return of spontaneous circulation (ROSC). ABGs were obtained 10-min post-ROSC and 40 min thereafter, to assess ventilation and modify ventilator settings as necessary.

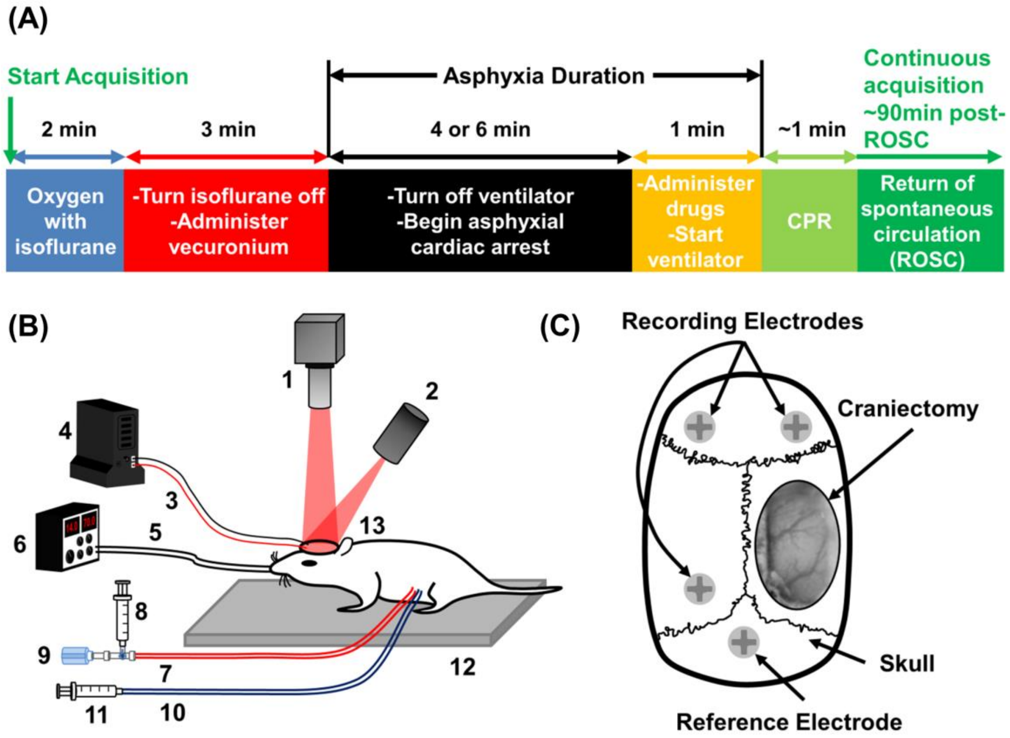

Figure 1.1: Cardiac arrest (CA) experimental design and setup. (A) Diagram of CA timeline. Experiment began (t = 0) with an isoflurane/oxygen mix. At t = 2min, isoflurane was turned off, Vecuronium administered, and animal exposed to room air. The ventilator was then turned off to initiate the asphyxial CA period that lasted 5- or 7-min. Approximately 1min prior to initiation of cardiopulmonary resuscitation (CPR), epinephrine, sodium bicarbonate and saline were administered and the ventilator restarted. CPR was then performed for ~1min until ROSC, after which data acquisition continued for ~90min post-ROSC. (B) Schematic of multi-instrument design to perform laser speckle imaging (LSI), arterial blood pressure measurements, and electroencephalography (EEG). (1) LSI camera with laser line filter and adjustable camera lens; (2) 809nm light source for LSI to display speckle pattern on rat cortex; (3) EEG wire that connected EEG screw electrodes to EEG preamplifier; (4) EEG preamplifier with 0.35Hz high pass filter; (5) intubation tubing connected to ventilator; (6) ventilator with adjustable settings; (7) femoral artery catheter; (8) syringe to administer fluids for dehydration and remove blood for arterial blood gas (ABG) measurements; (9) blood pressure transducer; (10) femoral vein catheter; (11) syringe to administer epinephrine, sodium bicarbonate and saline prior to CPR and ROSC; (12) stereotaxic frame with rat mounted; (13) brain illuminated by laser light with EEG screw electrodes. (C) Magnified view of animal head that shows location of EEG electrodes and craniectomy.

1.3.4 Multi-modal Instrument Design and Data Acquisition

To accomplish our multi-modal approach of monitoring CBF, arterial blood pressure, and brain electrophysiology before, during, and after CA and resuscitation, we combined LSI, arterial blood pressure, and EEG, as shown in Figure 1.1B. All technologies were simultaneously recorded throughout the entire experiment.

To measure CBF, LSI was used. As an excitation source we used a stabilized 809nm laser (Ondax, Monrovia, CA) with a long coherence length. The laser was sent through expansion optics and a ground glass diffuser (ThorLabs, Inc., Newton, NJ) to achieve near-uniform illumination over the craniectomy region (Figure 1.1C). The remitted light was sent through a laser line filter and raw speckle images were sampled at ~10fps using a Point Grey camera (Point Grey Research Inc., Richmond, BC, Canada) with a 10ms exposure time.

To measure arterial blood pressure, systolic and diastolic blood pressures were recorded from the femoral artery (Figure 1.1B) at 1Hz. MAP was calculated from the extracted systolic and diastolic blood pressures.

To perform EEG, screw electrodes were used (Figure 1.1C). EEG data acquisition was recorded from each implanted electrode at 1526Hz with a PZ2 preamplifier (Tucker-Davis Technologies Inc., Alachua, FL) equipped with a first-order high-pass filter (0.35Hz). Acquired data were extracted and further filtering and analysis performed as described in the next section.

1.3.5 Data Processing and Statistical Analysis

LSI processing used custom-written MATLAB code to process each raw speckle image and obtain CBF information. We used a sliding 5 x 5 square structuring element to convert each raw speckle image to a corresponding speckle contrast image. Eq. 1.1 was performed at each location of the structuring element:

$$K = \frac{\sigma}{<I>} \qquad \text{(Eq. 1.1)}$$

We then converted each speckle contrast image to a speckle flow index (SFI) map using a simplified speckle imaging equation[46]:

$$SFI = \frac{1}{2TK^2} \qquad \text{(Eq. 1.2)},$$

where K is the speckle contrast and T is the exposure time of the camera in seconds. A representative region of interest (ROI) was then selected within the craniectomy to obtain an average SFI value and create time-resolved CBF curves. We then calculated relative SFI curves (Eq. 1.3), and applied a sliding median filter of 10s in length.

$$relative\ SFI = 100 \times \frac{SFI(t)}{baseline\ SFI} \qquad \text{(Eq. 1.3)}$$

Baseline was defined as the mean SFI value the minute prior to asphyxia (to minimize isoflurane effects) and thus the relative SFI at baseline was 100. One minute prior to asphyxia was chosen as baseline due to post-anesthesia emergence and consequent cerebral hyperemia[47,48]. The median-filtered relative SFI curves were used for further statistical analyses. Relative SFI maps were also created by dividing the baseline SFI from Eq. 1.3 at each pixel of the SFI map, and a median filter was then applied to images taken over a 10s interval.

We evaluated several CBF characteristics post-ROSC using LSI data. For LSI, these included percent SFI above baseline at hyperemic peak, time from ROSC to hyperemic peak, percent SFI below baseline at the onset of stabilized hypoperfusion, and time from ROSC to the onset of stabilized hypoperfusion. Stabilized hypoperfusion was defined as the initial time when the relative SFI had less than a $\pm 1\%$ change for at least one min post-ROSC. For each CBF characteristics, we compared the 5- and 7-min asphyxial groups using a Student's t-test, where $p<0.05$ was considered statistically significant and results displayed as mean ± STD.

To assess the correlation between CBF and MAP, we performed a Spearman correlation test for data collected before stabilized hypoperfusion. To quantify the dysregulation between CBF and MAP, we calculated the median difference between relative SFI and relative MAP before and after stabilized hypoperfusion. The difference before and after stabilized hypoperfusion were compared using a paired t-test, where $p<0.05$ was considered statistically significant and results are displayed as mean ± STD.

Raw EEG data were filtered in the following fashion using custom written MATLAB (Mathworks Inc., Natick, MA) code. Data were detrended to remove DC bias and common averaged reference to reduce noise and artifacts across channels[49]. A finite impulse response (FIR) notch filter at 60Hz was used to remove electrical noise, followed by a FIR bandpass filter from 1–150Hz. Signals were then downsampled to 600Hz to reduce computational cost.

To detect the initial EEG burst, we developed an automated algorithm using custom-written MATLAB code. Peaks above 20μV were detected the minute prior to asphyxia and the mean peak value was calculated. Following resuscitation, when the EEG amplitude exceeded 50% of the mean peak value from baseline in the frontal electrodes, a burst was detected. To identify the presence of the initial EEG burst and minimize the effect of noise artifacts, we applied a selection criterion that bursting for five consecutive minutes was necessary. Once bursting occurred for this period, the algorithm reported the initial EEG burst time relative to ROSC, which was used in subsequent analysis. We compared the time from ROSC to initial EEG burst for 5- and 7-min asphyxial groups using a Student's t-test, where $p<0.05$ was considered statistically significant and results are displayed as mean ± STD.

To quantify the total amount of brain perfusion from ROSC to the initial EEG burst, we integrated over time the relative SFI time-course signal from ROSC to initial EEG burst.

We used a Spearman correlation test to determine the correlation between total brain perfusion and initial EEG burst time. We then compared the total perfusion from ROSC to initial EEG burst for 5- and 7-min asphyxial groups using a Student's t-test, where $p<0.05$ was considered statistically significant and results are displayed as mean ± STD. We performed the same correlation and statistical comparison using MAP time-course data.

To predict when the initial EEG burst occurred, we calculated a predictive burst ratio that utilized the total perfusion from ROSC to initial EEG burst and normalized to the asphyxial duration (Eq. 1.4).

$$predictive\ burst\ ratio = \frac{\int_{ROSC}^{Burst}(relative\ SFI\ or\ MAP)}{asphyxia\ duration}dt \qquad \text{(Eq. 1.4)}$$

The predictive burst ratio was calculated for each experiment and the median predictive burst ratio obtained from all experiments for relative SFI and MAP, separately. The predictive burst ratios for 5- and 7-min asphyxial groups were compared using a Student's t-test, where $p<0.05$ was considered statistically significant, and results are displayed as mean ± STD. For relative SFI and MAP individually, the median predictive burst ratio was used to predict when the initial EEG burst would occur. To predict the initial EEG burst we created time plots as a function of the predictive burst ratio, which we called the cumulative predictive burst ratio. To determine the cumulative predictive burst ratio, the upper bound of the integral in Eq. 1.4 was replaced with time, and incremented by each measurement time point. We then optimized the bounds of a linear fit to the cumulative predictive burst ratio. To obtain the optimal bounds of the linear fit, a range of lower and upper bounds were chosen from 0- to 6-min post-ROSC in 0.25min increments. All possible combinations for the linear fit were tested for each experiment. The bound combination that minimized the median predicted burst time error from all experiments was extracted. This analysis determined the bounds of the linear fit would be from 0.25- to 6-min post-ROSC. The slope (m) and y-intercept (b) were obtained from the linear fit. Using Eq. 1.5, we extrapolated and predicted the initial EEG burst time.

$$predicted\ burst\ time = m \times (median\ predictive\ burst\ ratio) + b \quad \text{(Eq. 1.5)}$$

To analyze the performance of the model using CBF and MAP, we computed the percent error of the predicted burst time to the actual burst time and compared the 5- and 7-min asphyxial groups. Results are displayed as median (range).

A second fitting algorithm, we called the robust predictive model, was used to predict the initial EEG burst. The second algorithm used a dynamic fitting method for the bounds of the linear fit to the cumulative predictive burst ratio, instead of the fixed bounds used in the original algorithm. To determine the bounds of the linear fit, a linear fit was applied from immediate post-ROSC to 5min post-ROSC. If the R^2 of the fit was greater than 0.98, then the fit was accepted. If the R^2 was below 0.98, then the lower bound was incremented by one time-point and another 5min linear fit was performed. This process was repeated in an iterative fashion, until the R^2 was greater than 0.98 for a 5min linear fit period. The slope (m) and y-intercept (b) were then extracted and used in Eq. 1.5 to extrapolate to the predicted initial EEG burst time. Similar to the previous model, we computed the percent error of the predicted burst time to the actual burst time and compared the 5- and 7-min asphyxial groups for both CBF and MAP data. Results are displayed as median (range).

1.4 Results

1.4.1 More severe CA results in longer time to stabilized hypoperfusion

To quantify the precise magnitude (relative to baseline) and time of the hyperemic peak and stabilized hypoperfusion, LSI data were used. An example of relative SFI maps from baseline (Figure 1.2A), CA (Figure 1.2B), hyperemia (Figure 1.2C), and stabilized hypoperfusion (Figure 1.2D) are shown. We quantified each of the four characteristics (Figure 1.2E) for both 5- and 7-min asphyxial groups and performed a Student's t-test to compare the groups. The percent change in SFI above baseline (Figure 1.2F) was non-significant between 5-and 7-min asphyxia (44.13 ± 11.06% vs 37.11 ± 28.80%, p = 0.28). The time from ROSC to hyperemic peak (Figure 1.2G) trended shorter for 5-min asphyxia than 7-min asphyxia, but the difference was non-significant (5.19 ± 1.10min vs 5.99 ± 1.26min, p = 0.12). The percent change in SFI below baseline (Figure 1.2H) was equivalent for 5- and 7-min asphyxial groups (44.95 ± 9.50% vs 42.26 ± 11.40%, p = 0.33). The time from ROSC to stabilized hypoperfusion (Figure 1.2I) was significantly shorter for 5-min asphyxia than 7-min asphyxia (15.60 ± 3.67min vs 23.76 ± 5.12min, p = 0.003).

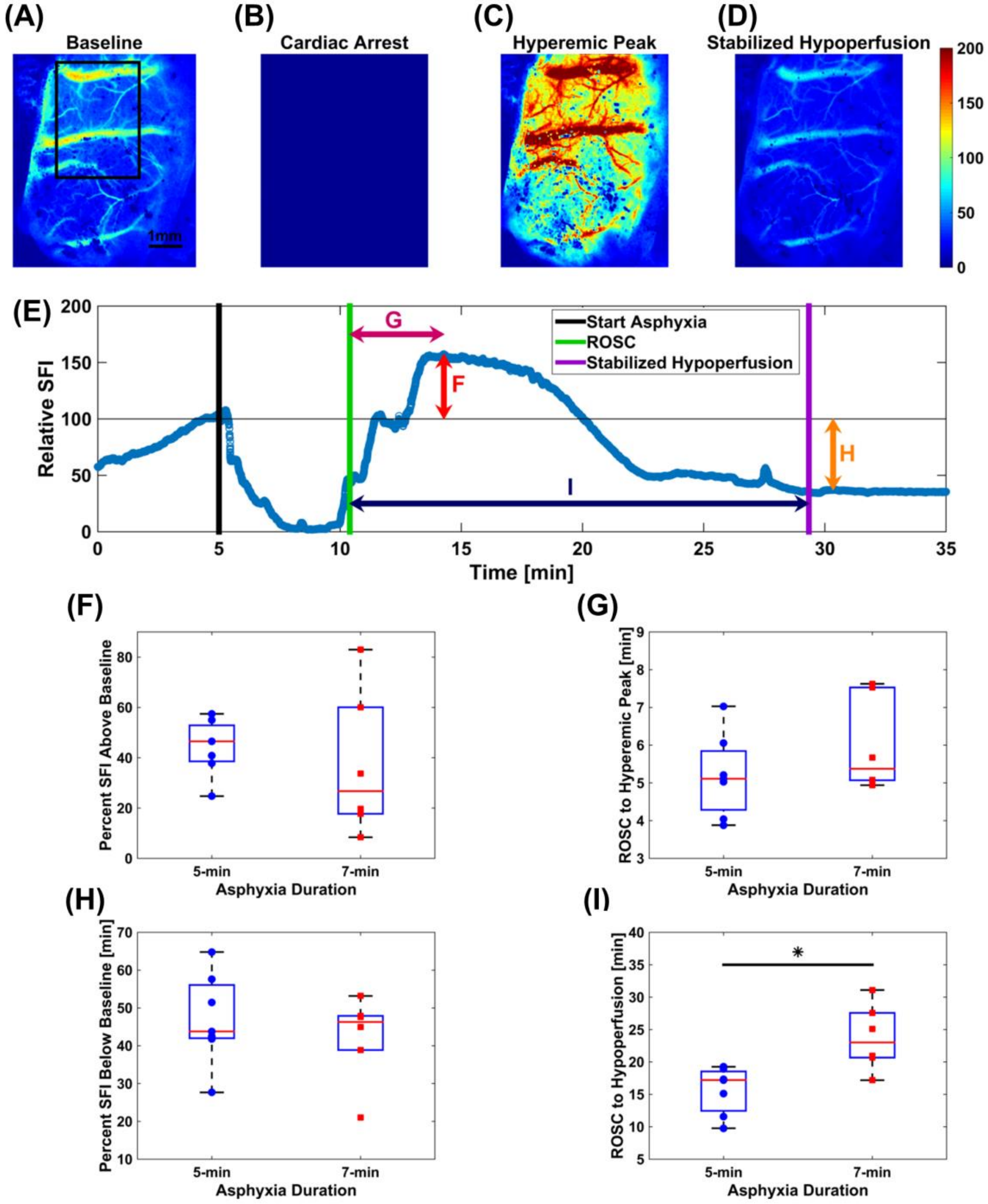

Figure 1.2: CBF characteristics. Median-filtered relative SFI maps from a representative 5-min asphyxia experiment acquired during (A) baseline, where black rectangle represents ROI selected to avoid specular reflection, and a 1mm scale bar, (B) cardiac arrest, (C) hyperemic peak, and (D) stabilized hypoperfusion. The vertical color bar indicates relative SFI units. (E) A representative 5-min asphyxia experiment that shows relative SFI time course plot with schematic of CBF characteristics. Black vertical line represents start of asphyxia, green vertical line represents ROSC, and purple vertical line represents stabilized hypoperfusion. Double-arrowed red line with letter F represents percent SFI above baseline at hyperemic peak, double-arrowed dark magenta line with letter G represents time from ROSC to hyperemic peak, double-arrowed orange line with letter H represents percent SFI below baseline at stabilized hypoperfusion, double-arrowed navy blue line with letter I represents time from ROSC to stabilized hypoperfusion. Comparison between 5- and 7-min asphyxial durations for (F) percent SFI above baseline at hyperemic peak (44.13 ± 11.06% vs 37.11 ± 28.80%, $p = 0.28$), (G) time from ROSC to hyperemic peak (5.19 ± 1.10min vs 5.99 ± 1.26min, $p = 0.12$), (H) percent SFI below baseline at stabilized hypoperfusion (44.95 ± 9.50% vs 42.26 ± 11.40%, $p = 0.33$), (I) time from ROSC to stabilized hypoperfusion (15.60 ± 3.67min vs 23.76 ± 5.12min, $p = 0.003$). Asterisk represents significant differences ($p < 0.05$).

1.4.2 CBF and MAP are coupled before stabilized hypoperfusion and uncoupled after stabilized hypoperfusion

To investigate the coupling between CBF and MAP, we examined differences between the relative SFI and MAP time courses (Figure 1.3A). Both relative SFI and MAP had a sharp decrease as the asphyxial period began (t = 5min), and each had an overshoot phase post-ROSC (t ~ 15min). After the hyperemic phase, the relative SFI time-course was at a large deficit compared to baseline (~70% below baseline), while the MAP returned to near baseline (~100mmHg). To quantify the similarities, we used a Spearman correlation test before stabilized hypoperfusion (Figure 1.3B). Our results show that MAP and CBF are highly correlated before stabilized hypoperfusion for each experiment, with highly statistically significant correlation coefficients ($R = 0.75 \pm 0.1$, $p < 1.4 \times 10^{-92}$). To quantify the dysregulation between CBF and MAP, we calculated the median difference between relative SFI and relative MAP before and after stabilized hypoperfusion. The median difference between relative SFI and relative MAP before stabilized hypoperfusion was significantly higher (CBF and MAP are more close) than after stabilized hypoperfusion (-16.67 ± 9.13 vs -68.06 ± 11.72, $p = 1.5 \times 10^{-8}$).

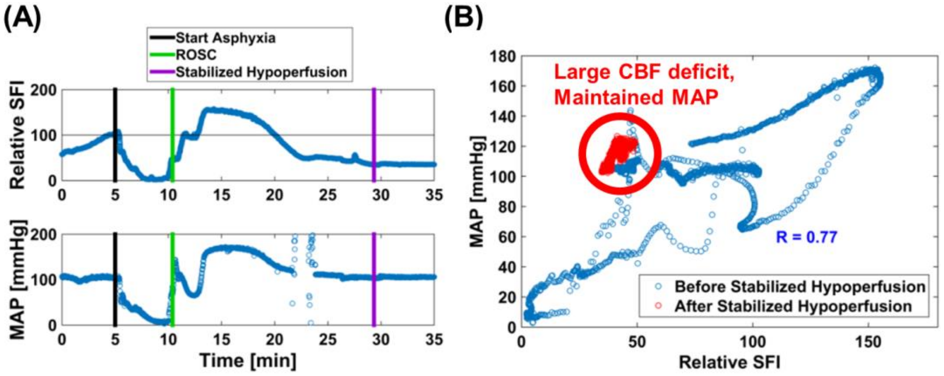

Figure 1.3: CBF and MAP comparison. (A) A representative 5-min asphyxia experiment that shows relative SFI (top) and MAP (bottom) time-course plots. Black vertical line represents start of asphyxia, green vertical

line represents ROSC, and purple vertical line represents stabilized hypoperfusion. The relative SFI time-course shows that CBF is much lower than baseline at stabilized hypoperfusion, while the MAP is nearly 100mmHg at stabilized hypoperfusion. The gap from ~21- to 23-min on the MAP time-course is due to ABG being taken. (B) The same 5-min asphyxia experiment from (A) that compares MAP and relative SFI before stabilized hypoperfusion (blue) and after stabilized hypoperfusion (red). Before stabilized hypoperfusion MAP and relative SFI are significantly correlated for the representative rat ($R = 0.77$, $p = 1 \times 10^{-93}$). After stabilized hypoperfusion, CBF is at a major deficit compared to baseline, while MAP is maintained near baseline, circled in red.

1.4.3 Initial EEG burst begins after CBF hyperemic phase and before stabilized hypoperfusion

To investigate the relationship between restarting brain electrical activity to CBF after resuscitation, we studied the timing of the initial EEG burst with respect to the CBF time-course. First, we determined when the initial EEG burst occurred for 5- and 7-min asphyxial durations (Figure 1.4A). We compared the performance of our automated detection algorithm to visual detection of the initial EEG burst. The mean percent error was less than 1% for all experiments. The time from ROSC to initial EEG burst (Figure 1.4B) was significantly shorter for 5-min asphyxia than 7-min asphyxia (12.17 ± 2.17min vs 16.97 ± 3.67min, $p = 0.007$).

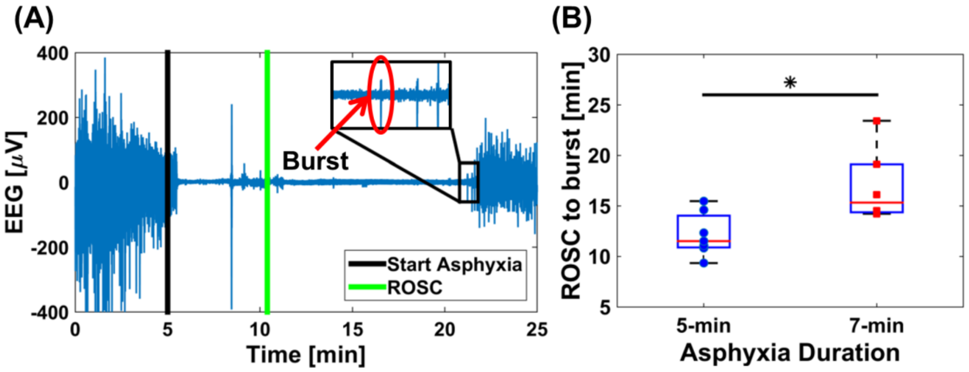

Figure 1.4: Initial EEG burst. (A) A representative 5-min asphyxia experiment that shows EEG time-course to illustrate detection of initial EEG burst post-ROSC. EEG data shown was recorded from the upper-left electrode in Figure 1.1C. Black vertical line represents start of asphyxia, green vertical line represents ROSC, and red circle of inset is the first EEG burst detected by automated algorithm post-ROSC. (B) Comparison between 5-min and 7-min asphyxial durations for the time from ROSC to initial EEG burst (12.17 ± 2.17min vs 16.97 ± 3.67min, $p = 0.007$). Asterisk represents significant difference ($p < 0.05$).

We observed the initial EEG burst always occurred as CBF decreased toward stabilized hypoperfusion (Figure 1.5A), which led to the hypothesis that a threshold amount of CBF is necessary to restart brain electrical activity following resuscitation from CA. We quantified total brain perfusion from ROSC to initial EEG burst as the time-integrated relative SFI. We also performed this analysis with MAP, as our previous results show MAP and relative SFI are correlated before stabilized hypoperfusion (Figure 1.3B). Using the Spearman correlation test, our results show a significant positive correlation between time-integrated relative SFI and time to initial EEG burst (R = 0.84, p = 0.0003; Figure 1.5B). Similarly, our results show a significant positive correlation between time-integrated MAP and time to initial EEG burst (R = 0.80, p = 0.001; Figure 1.5C).

We then compared 5- and 7-min asphyxial groups. Our results show that significantly less time-integrated relative SFI (1290 ± 140 vs 1781 ± 286, p = 0.002) and non-significantly less time-integrated MAP (1331 ± 257 vs 1645 ± 378, p = 0.1) is necessary to initiate EEG bursting for 5-min asphyxia than 7-min asphyxia (Figure 1.5D and 1.5E, respectively). These results indicate there is not a threshold of CBF to restart brain electrical activity following resuscitation from different severities of asphyxial CA, and thus our initial hypothesis was incorrect. Therefore, based on these results, we normalized the time-integrated relative SFI and MAP to the asphyxial duration to create an asphyxial invariant threshold; we call this term the predictive burst ratio (Eq. 1.4). The predictive burst ratio had less spread using CBF (256 ± 33) than MAP (252 ± 53). The predictive burst ratio was not significantly different between 5- and 7-min asphyxial durations (Figure 1.5F and 1.5G, respectively) for relative SFI (258.0 ± 28.1 vs 254.5 ± 40.8, p = 0.86) and MAP

(269.7 ± 47.5 vs 249.7 ± 43.3, p = 0.45). These calculations suggest that normalizing the total perfusion to the asphyxial duration is an appropriate normalization term.

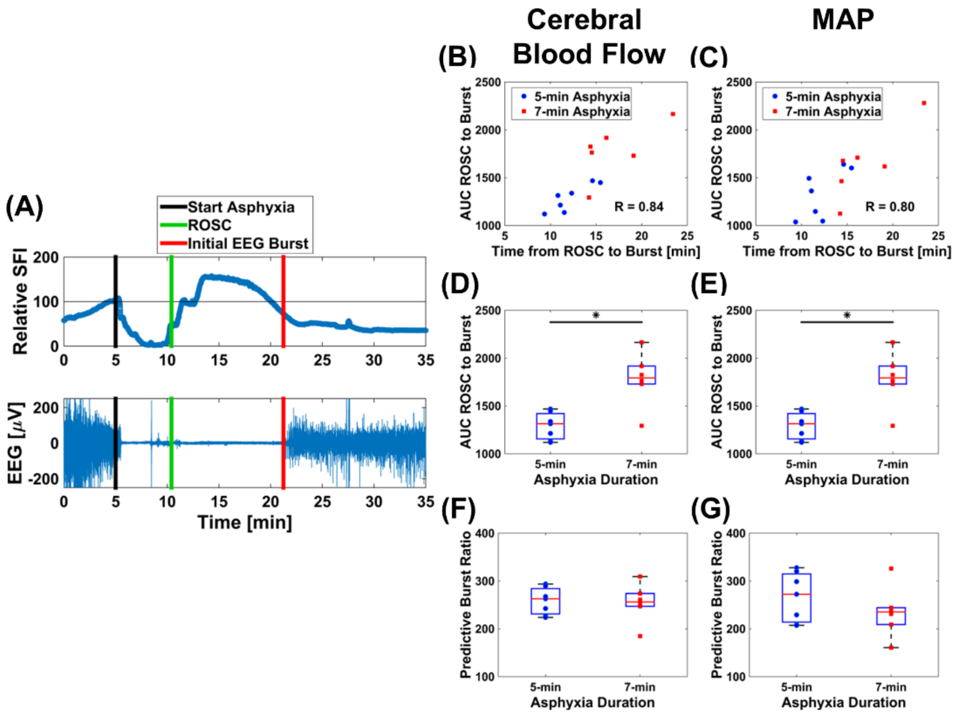

Figure 1.5: Initial EEG burst begins after CBF hyperemic phase and before stabilized hypoperfusion. (A) Representative relative SFI and EEG time-courses to illustrate initial EEG burst occurs after CBF hyperemic phase and before stabilized hypoperfusion. EEG data shown was recorded from the upper-left electrode in Figure 1.1C. Black vertical line represents start of asphyxia, green vertical line represents ROSC, and red vertical line represents initial EEG burst. (B and C) AUC from ROSC to burst vs time to burst after ROSC shows a significant positive correlation for relative SFI (left) (R = 0.84, p = 0. 0003) and MAP (right) (R = 0.80, p = 0. 001). (D and E) AUC from ROSC to burst is significantly less for 5-min asphyxia than 7-min asphyxia for relative SFI (left) (1290 ± 140 vs 1781 ± 286, p = 0.002) and non-significantly time-integrated MAP (right) (1331 ± 257 vs 1645 ± 378, p = 0.1). (F and G) The predictive burst ratio was non-significant comparing 5- and 7-min asphyxial durations for relative SFI (left) (258.0 ± 28.1 vs 254.5 ± 40.8, p = 0.86) and MAP (right) (269.7 ± 47.5 vs 249.7 ± 43.3, p = 0.45). Asterisks represent significant differences (p <0.05).

1.4.4 CBF predicts initial EEG burst for 5-min asphyxia, but is a poor predictor for 7-min asphyxia

To assess the accuracy of the predictive burst ratio, we performed linear regression to the cumulative predictive burst ratio from 0.25- to 6-min post-ROSC and extrapolated the linear fit using the median predictive burst ratio to predict the initial EEG burst time (Eq. 1.5). Examples of the predictive model using CBF and MAP for 5- and 7-min asphyxia are shown in Figure 1.6. The median percent error for relative SFI and MAP were 8.21% (range = 1.57% – 80.97%) and 12.10% (range = 3.39% – 133.92%), respectively. Since the percent error range of predicting the initial EEG burst was large, we assessed how 5- and 7-min asphyxial groups compared. The 5-min asphyxial group was associated with a considerably lower median percent error than the 7-min asphyxial group for relative SFI [3.46% (range = 1.57% – 17.22%) vs 31.22% (range = 7.95% – 80.97%), Figure 1.6C] and for MAP [8.01% (range = 3.39% – 23.40%) vs 40.80% (range = 9.34% – 133.92%), Figure 1.6F], respectively. These results suggest that CBF and MAP more accurately predict onset of EEG bursting for 5-min asphyxia than for 7-min asphyxia, and that CBF predicts better than MAP for both 5- and 7-min asphyxial durations.

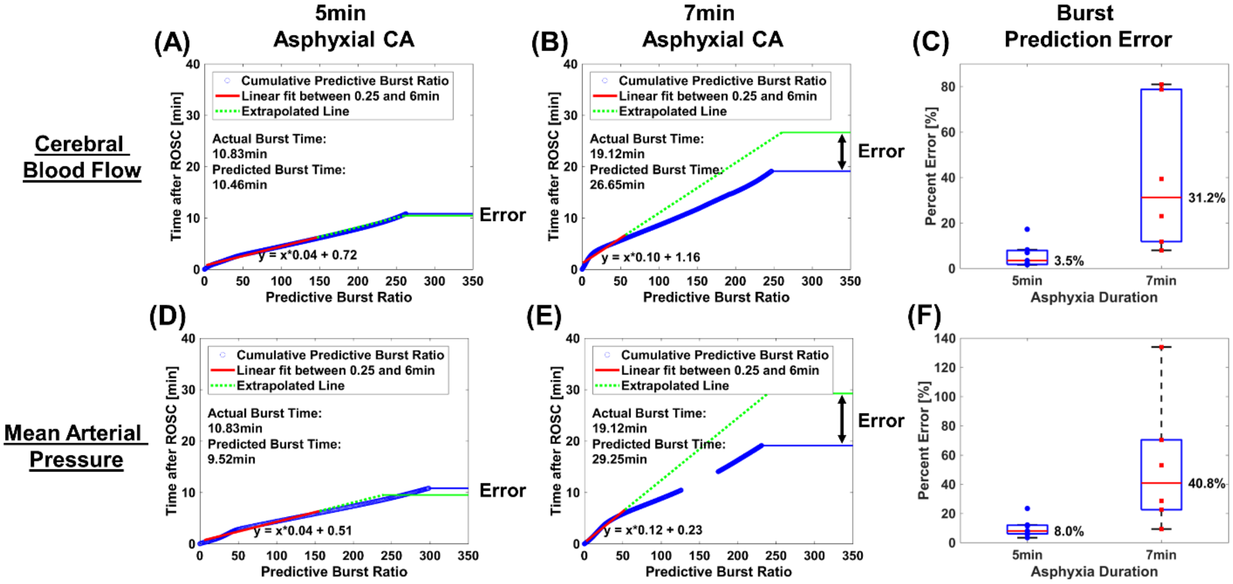

Figure 1.6: Representative predictive burst times for initial EEG burst using predictive burst model. (A) A representative 5-min asphyxial experiment that used CBF data to predict the initial EEG burst time, percent error of 3.42% obtained. (B) A representative 7-min asphyxial experiment that used relative SFI to predict initial EEG burst time, a percent error of 39.37% obtained. (C) Burst prediction error for 5- and 7-min asphyxial CA using CBF data. Median percent error for 5- and 7-min asphyxia are 3.5% and 31.2%, respectively. (D) Same 5-min asphyxial experiment used as (A), but used MAP to predict initial EEG burst time, percent error of 12.10% obtained. (A-D) the distance between the green and blue horizontal solid lines represent the time error in predicting the initial EEG burst. (E) Same 7-min asphyxial experiment used as (B), but used MAP to predict initial EEG burst time, percent error of 52.96% obtained. Gap from ~140 to ~170 of predictive burst ratio is due to ABG being taken. (F) Burst prediction error for 5- and 7-min asphyxial CA using MAP data. Median percent error for 5- and 7-min asphyxia are 8.0% and 40.8%, respectively.

Using the predictive model with fixed bounds of the linear fit results in large errors when predicting the initial EEG burst, as is shown in Figure 1.7. MAP and more severe CA are typically characterized by a sharp increase immediately post-ROSC, followed by a decrease, before eventually increasing to the large overall hyperemic peak. Due to these characteristics, and non-linear changes, the linear fit to the cumulative predictive burst ratio results in an over-estimation of the predicted burst time. To overcome this limitation, a revised predictive algorithm was developed to minimize the effects of the non-linear changes associated with MAP and more severe CA.

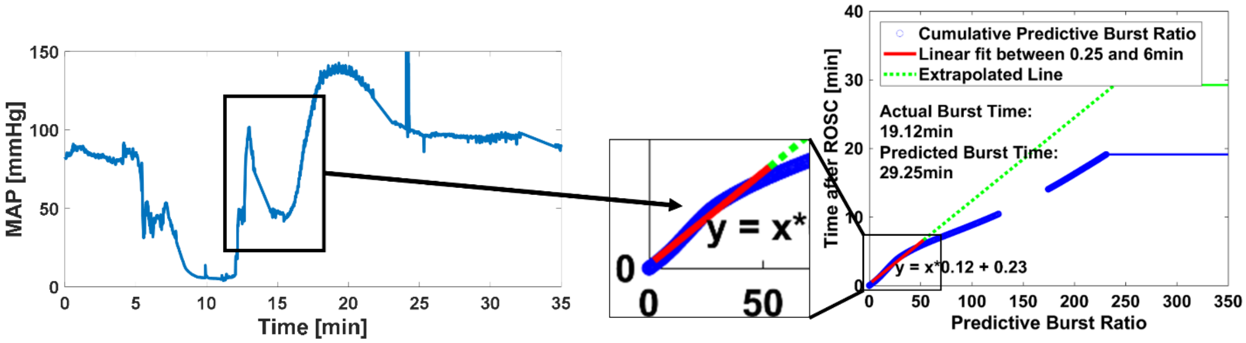

Figure 1.7: Representative example of MAP that leads to large error in fixed bounds predictive algorithm. (Left) Representative MAP time course for a 7-min asphyxial CA. Boxed region shows the non-linear changes associated with MAP and more severe CA immediately post-ROSC. Arrowed to the non-linear change in the zoomed-in version (middle) of the predictive burst ratio that leads to large prediction error.

1.4.5 Revised predictive algorithm performs just as well for CBF and MAP and 5- and 7-min asphyxial CA at predicting initial EEG burst

To assess the accuracy of the new predictive model, we used the same predictive burst ratio. We performed linear regression to the cumulative predictive burst ratio for a 5min period post-ROSC and extrapolated the linear fit using the median predictive burst ratio to predict the initial EEG burst time (Eq. 1.5). Examples of the predictive model using CBF and MAP for 5- and 7-min asphyxia are shown in Figure 1.8. The median percent error using the CBF and MAP were 8.57% (range = 1.21% – 28.31%) and 9.72% (range = 7.04% – 33.59%), respectively. We also assessed how the 5- and 7-min asphyxial groups compared. The 5- and 7-min asphyxial groups had very similar percent errors using the CBF data [8.57% (range = 1.21% – 18.69%) vs 9.91% (range = 2.45% – 28.31%)] and using MAP data [19.02% (range = 7.07% – 26.53%) vs 9.03% (range = 7.04% – 33.59%)], respectively. These results show that the new predictive model is more robust at accurately predicting both the 5- and 7-min asphyxial durations, as well as the CBF and MAP data.

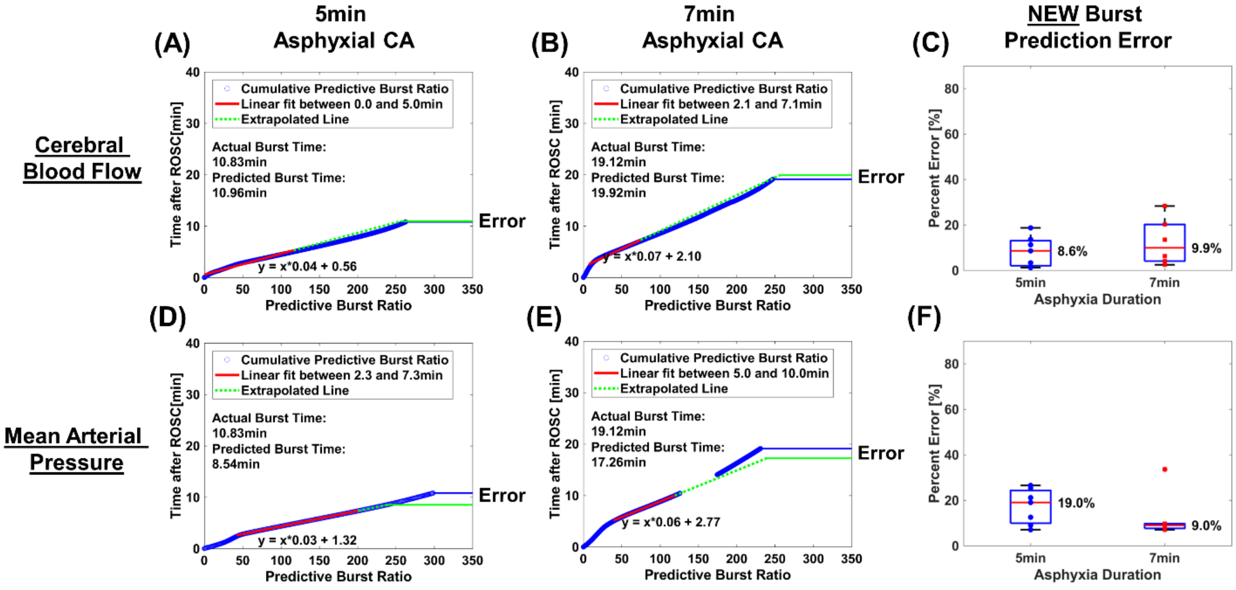

Figure 1.8: Representative predictive burst times for initial EEG burst using NEW predictive burst model. (A) A representative 5-min asphyxial experiment that used CBF data to predict the initial EEG burst time, percent error of 1.21% obtained. (B) A representative 7-min asphyxial experiment that used relative SFI to predict initial EEG burst time, a percent error of 4.18% obtained. (C) Burst prediction error for 5- and 7-min asphyxial CA using CBF data. Median percent error for 5- and 7-min asphyxia are 8.57% and 9.91%, respectively. (D) Same 5-min asphyxial experiment used as (A), but used MAP to predict initial EEG burst time, percent error of 21.14% obtained. (A-D) the distance between the green and blue horizontal solid lines represent the time error in predicting the initial EEG burst. (E) Same 7-min asphyxial experiment used as (B), but used MAP to predict initial EEG burst time, percent error of 9.73% obtained. Gap from ~140 to ~170 of predictive burst ratio is due to ABG being taken. (F) Burst prediction error for 5- and 7-min asphyxial CA using MAP data. Median percent error for 5- and 7-min asphyxia are 19.02% and 9.03%, respectively.

1.5 Discussion and Conclusion

Using a multi-modal platform, we demonstrate a number of novel findings elucidating the relationship between brain electrical activity and hemodynamics during CA and resuscitation. Our platform combined LSI, arterial blood pressure, and EEG to quantitatively assess CBF, MAP, and brain electrophysiology dynamics during CA and resuscitation.

CBF is known to have distinct phases following resuscitation from CA[23]. In this study we quantified the precise magnitude (relative to baseline) and time of the hyperemic peak and stabilized hypoperfusion post-ROSC (Figure 1.2E-I), due to our system's relatively high temporal resolution (~seconds). Previous studies have not been able to identify the exact time and magnitude of the hyperemic peak and stabilized hypoperfusion post-ROSC due to the relatively poor temporal resolution (~5–30min) [19,22,50]. Interestingly, in a pediatric model of asphyxial CA, Manole et al.[21] and Shaik et al.[51] both did not observe a hyperemic peak in cortical CBF using MRI and LSI, respectively. Their results suggest that post-ROSC cerebral hemodynamics vary between adults and children. These varying dynamics, may suggest the need to treat adults and children differently following resuscitation from asphyxial CA.

Under normal conditions, the brain is highly regulated as CBF is constant over a wide range of MAP. Previous studies have examined cerebrovascular autoregulation following CA. These studies have generally reported that the lower limit of autoregulation increases post-ROSC[17]. Our results are in line with these findings, as MAP returned to near baseline post-ROSC, while CBF was at a major deficit after the onset of stabilized hypoperfusion (Figure 1.3B). Furthermore, to assess which asphyxial duration had more cerebrovascular dysregulation, we compared the median difference between relative SFI and relative MAP for 5- and 7-min asphyxial durations after stabilized hypoperfusion. We observed that CBF more closely resembled MAP for 7-min than 5-min asphyxial duration (-

62.70 ± 14.58 vs -72.65 ± 6.67, p = 0.13). This result suggests that more severe CA is associated with increased cerebrovascular dysregulation, as CBF more closely resembles MAP. Since MAP is a parameter clinicians depend on to indirectly monitor cerebral perfusion post-ROSC, our results suggest that direct CBF measurement may be necessary to adequately assess and optimize cerebral perfusion for different severities of CA.

Many studies have investigated the evolution of brain electrical activity post-ROSC[7,52], while few have reported the time point at which EEG activity resumes post-ROSC[8,28]. To our knowledge, only one study analyzed the onset of EEG bursting with relation to neurological outcome. Chen et al. showed a faster onset of EEG bursting in hypothermia-treated rats, which also had better neurological outcome at 96h post-ROSC[28]. Our results show that more severe CA, which results in worse neurological outcome[9], resulted in longer time to initial EEG burst (Figure 1.4B). However, the mechanism that drives the brain to restart following resuscitation is not well understood. Our data suggests that CBF is a key component of this mechanism.

We observed that the initial EEG burst occurred after the hyperemic peak, but prior to stabilized hypoperfusion (Figure 1.5A). We then investigated whether a threshold of CBF is necessary to restart brain electrical activity. Our results suggest that more perfusion is necessary to restart brain electrical activity for 1) a longer time to initial EEG burst (Figure 1.5B) and 2) more severe CA (Figure 1.5D). Due to this, we normalized the total perfusion by the asphyxial duration to develop an empirical predictive burst ratio (Figure 1.5F). We plan to use the median predictive burst ratio from these experiments to predict when the initial EEG burst occurs in future experiments.

In the present study, we used two different predictive models to predict the initial EEG burst. The first model used rigid bounds for a linear fit from 0.25- to 6-min post-ROSC. The median predictive burst ratio from CBF data was then used with the linear fit, which performed well at predicting the initial EEG burst for 5-min asphyxia (3.46% error) (Figure 1.6A), but poorly for 7-min asphyxia (31.22% error) (Figure 1.6B). These results suggest that a threshold of cerebral reperfusion is both necessary and sufficient to restart brain electrical activity following 5-min asphyxia, but this condition alone is not sufficient for brain electrical activity to resume following 7-min asphyxia. However, upon visualizing non-linear changes in more severe CA and MAP, a second predictive model was used, which was more robust and used non-uniform bounds for the linear fit.

Using the robust predictive model, the same median predictive burst ratio from CBF data was then used with the linear fit, which performed equally well at predicting the initial EEG burst for 5- (8.57% error) and 7-min (9.91% error) asphyxial CA (Figure 1.8C). Furthermore, the median predictive burst ratio from MAP data was then used with the linear fit, which also performed equally well at predicting the initial EEG burst for 5- (19.02% error) and 7-min (9.03% error) asphyxial CA (Figure 1.8F). Using this predictive model shows that either that CBF or MAP can be used to predict the resumption of brain electrical activity following resuscitation from CA. Due to the residual error that is still present with the robust predictive model, we hypothesize cerebral metabolic deficiency, cerebrovascular dysregulation, and an imperfect linear fitting method may be responsible for the continued error. To test this hypothesis, future studies will be focused on developing a revised empirical predictive model that utilizes the cerebral metabolic rate of oxygen to describe the initial EEG burst[53–55].

In short, knowledge of when EEG activity will recover may potentially equip clinicians with more accurate prognostication, better treatments for post-CA coma, and improve neurological outcome.

Limitations exist in our study. Despite the statistically significant results and trends identified in this study, the power of these findings is limited due to a small sample size. In addition, these experiments used a full craniectomy, which may change the intracranial pressure. In the future we plan to perform experiments with a thinned-skull cranial window to minimize this effect.

In conclusion, we have developed a multi-modal approach to quantify CBF, MAP, and brain electrophysiology dynamics with high temporal resolution, in an asphyxial CA model. Our multi-modal approach combines LSI, arterial blood pressure, and EEG into a preclinical monitoring setup that effectively mimics an intensive care unit. Our results quantify the time and magnitude of the hyperemic peak and stabilized hypoperfusion post-ROSC. Furthermore, we show that CBF and MAP are well correlated before stabilized hypoperfusion, but CBF is at a large deficit after stabilized hypoperfusion, despite normal MAP. Finally, we demonstrate that EEG bursting begins after the CBF hyperemic phase and before stabilized hypoperfusion. We demonstrated that we can predict when the initial EEG burst occurs for less severe CA well using a fixed predictive model, but using a robust predictive model is able to predict the initial EEG burst for both severities of CA. Together, these results indicate the importance of using multi-modal approaches to investigate CA recovery to better understand physiological processes and ultimately allow for novel therapeutic approaches that improve neurological outcome.

1.6 Acknowledgements

We gratefully acknowledge support from the Arnold and Mabel Beckman Foundation, the United States National Institutes of Health (grant number P41EB015890), the National Science Foundation Graduate Research Fellowship Program under Grant No. DGE-1321846 to Christian Crouzet, the Hewitt Foundation for Medical Research and ICTS 1TL1TR001415-01 to Dr. Robert H. Wilson, and KL2 grant via NIH CTSA UL1 TR001414 and funds from the Department of Neurology, School of Medicine to Dr. Yama Akbari.
We would like to thank the Beckman Laser Institute Microvascular Therapeutics and Imaging lab and Akbari lab for their support and input in this work.

CHAPTER 2: Influence of cerebral blood flow and femoral artery pulsatility on short-term neurological outcome following resuscitation from cardiac arrest in a rat model

2.1 Abstract

Background—Impaired neurological function affects 85 to 90% of cardiac arrest (CA) survivors. Pulsatile blood flow may play an important role on neurological recovery post-CA due to its effects on oxygen uptake, vascular tone, and cellular metabolism. In this study, we characterized the effects of asphyxial CA (ACA) on acute (<2h post-CA) cerebral blood flow (CBF) and femoral arterial blood pressure (ABP) pulsatility and their relationship to cerebrovascular resistance (CVR) and neurological outcome.

Methods and Results—Male Wistar rats were subjected to either 5- or 7-min of ACA followed by cardiopulmonary resuscitation. A multi-modal platform that combined laser speckle imaging (LSI), ABP, and electroencephalography (EEG) was used to monitor CBF, peripheral blood pressure, and brain electrophysiology, respectively. CVR and pulsatile CBF and ABP were assessed during baseline, CA, hyperemia (~10min post-resuscitation), early hypoperfusion (~20min post-resuscitation), and late hypoperfusion (~60min post-resuscitation). Short-term neurological outcome was assessed using quantitative EEG 90min post-resuscitation. We found that CBF pulsatility is significantly altered from baseline at all experimental time-points, while ABP pulsatility changes little. The alteration of CBF pulsatility is inversely correlated with changes in CVR, but ABP pulsatility had no association to CVR. Interestingly, we found that CBF pulsatility is not associated to short-term neurological outcome, but increased ABP pulsatility is associated with worse short-term neurological outcome.

Conclusions—Our data suggests that simultaneous monitoring of immediate changes in CBF and ABP pulsatility may provide early prognostic information and that the use of therapeutics to modify pulsatility within 2h post-CA may alter neurological outcome.

2.2 Introduction

Annually, over 550,000 people in the United States suffer cardiac arrest (CA) while initial survival rates remain poor (10-30%)[1]. Approximately 85 to 90% of survivors have impaired cognitive function, which leads to decreased quality of life for survivors, increased burden on caregivers, and direct costs of over $6 billion/year[1,2]. To improve neurological recovery and understand how the brain recovers following CA, a critical need exists to investigate physiological processes that impact the brain, such as cerebral blood flow (CBF), arterial blood pressure, and brain electrophysiology.

A key physiological process that has been shown to be extremely important is pulsatile blood flow. Studies have shown that pulsatile flow (compared to non-pulsatile flow) during cardiac bypass surgery and extracorporeal membrane life support (ECMO) is associated with improved neurological and physiological outcomes[29–32]. Furthermore, modulation of pulsatility through mechanically controlled devices is associated with reduced cerebrovascular resistance (CVR) and improved oxygen uptake during post-ischemic reperfusion, which can improve neurological outcome[33].

The binary case of pulsatile versus non-pulsatile flow strongly supports that pulsatile flow is better than non-pulsatile flow[29–33]. However, aging[56,57], stroke[58], acute brain injury[59], small vessel disease[60] and CA[35] all modulate pulsatile blood flow to a different degree. Results from these studies suggest conflicting associations between pulsatility and neurological outcome.

To better understand the relationship between pulsatility and neurological outcome following CA, several gaps in the knowledge base must be addressed. First, low frequency (<0.4Hz) studies have only examined survivors or non-survivors of CA, and not neurological function or outcome after CA[34,35]. Second, studies of the pulsatile waveform typically focus on CBF and not peripheral hemodynamics associated with the aorta or femoral artery. Third, the influence of CVR on CBF and the peripheral pulsatile waveform has not been investigated. Finally, clinical studies begin upon hospital admission followed by measurements on subsequent days after CA, and hence do not enable study of immediate pulsatile signal changes after resuscitation (during ischemia-induced hyperemia and hypoperfusion) and their relationship to neurological outcome.

To address these gaps, we used an established preclinical model of asphyxial CA (ACA) to continuously monitor pulsatile CBF and femoral arterial blood pressure (ABP) associated with the heartbeat. We used CBF and ABP data to obtain a measurement of changes in CVR, and electroencephalography (EEG) to measure short-term neurological outcome 90min after resuscitation. Using these measurements, we quantified CBF and ABP pulsatility immediately after resuscitation and compared changes among different phases in the experiment. We also quantified the relationship between CBF and ABP pulsatility to CVR, and compared CBF and ABP pulsatility to short-term neurological outcome. We hypothesized that increased CBF pulsatility was associated with improved short-term neurological outcome. However, our key finding showed that increased pulsatile ABP is associated with worse short-term neurological outcome, and pulsatile CBF is not associated with short-term neurological outcome. Collectively, our findings indicate the importance of investigating immediate CBF and ABP pulsatility following resuscitation from CA to determine potentially modifiable factors that improve neurological outcome.

2.3 Materials and Methods

The ACA model and study protocol (no. 2013-3098) were approved by the Institutional Animal Care and Use Committee at University of California, Irvine.

2.3.1 Animal Preparation

We used our ACA model to perform experiments on 11 adult male Wistar rats (baseline characteristics shown in Table 2.1)[36,61,62]. Rats were calorically restricted 12-16h prior to onset of CA. On the day of CA induction, rats were anesthetized, intubated, and connected to a mechanical ventilator via tubing (Kent Scientific, Torrington, CT). During surgery, isoflurane was maintained at 2% with a 50%/50% N_2/O_2 mixture at 2LPM. The ventilation settings were maintained at 70 breaths per min (BPM), with 12–14cmH_2O peak inspiration pressure (PIP) and 3cmH_2O peak end expiratory pressure (PEEP). Animal temperature was continuously measured with a rectal thermometer (Kent Scientific, Torrington, CT) and maintained between 36.5 and 37.5^{o}C. The rat was then positioned on a stereotactic frame (Kopf Instruments, Tujunga, CA).

A midline incision was performed over the scalp and the scalp retracted to expose the skull for EEG electrode implantation (Plastics One Inc., Roanoke, VA). Two frontal electrodes were implanted 2mm anterior and 2.5mm lateral to bregma, and one electrode was implanted over the visual cortex 5.5mm posterior and 4mm left of bregma. A reference electrode was implanted 3mm posterior to lambda. Following EEG electrode implantation, a 4mm x 6mm craniectomy was created over the right sensory and visual cortices to create a window for optical imaging. Saline was applied periodically to ensure the brain remained hydrated. Following the craniectomy, the femoral artery and vein were cannulated. Invasive arterial blood pressure from the femoral artery was measured continuously at ~200Hz. Baseline arterial blood gas (ABG) measurements (Abaxis, Union City, CA) were obtained within 30min prior to initiation of ACA.

2.3.2 Experimental Protocol

At experiment start time, rats were placed on 0.5–1% isoflurane (balance 100% O_2). After 2min, inhaled air was changed to room air (21% O_2), isoflurane administration turned off to wash out anesthesia, and neuromuscular blockade initiated with 1mL of intravenous Vecuronium (2mg/kg), flushed with 1mL of heparinized saline. At 5min, asphyxia was initiated by turning the ventilator off and clamping the tubing. Rats were subjected to a period of either 5- or 7-min asphyxia. Thirty seconds prior to end of asphyxial period, mechanical ventilation was re-initiated at 100% O_2 with respiratory rate of 75–85BPM, PIP of 17.5–18.5 cmH_2O, and PEEP of 3cmH_2O at 2.5LPM. Epinephrine (0.01mg/kg) and sodium bicarbonate (1mmol/kg), followed by 2mL of heparinized saline, were administered intravenously. Chest compressions were started at end of asphyxial period until return of spontaneous circulation (ROSC) was achieved. ABGs were obtained 10-min post-ROSC and every 40 min thereafter, to assess and modify ventilator settings as necessary.

Table 2.1: Baseline Characteristics

	5-min ACA (n=6)	7-min ACA (n=5)	p-value
Preparation Time [h]	6.19±1.14	5.46±0.79	0.26
Weight [g]	356.50±44.07	347.60±33.64	0.72
Temperature [^{0}C]	37.02±0.39	37.04±0.23	0.91
pH	7.41±0.04	7.44±0.03	0.29
pCO_2 [mmHg]	40.13±4.67	35.74±6.04	0.21
pO_2 [mmHg]	159.33±38.17	135.20±25.26	0.26
HCO_3^- [mmol/L]	25.32±1.24	23.88±2.92	0.30
Hb [g/dL]	12.05±1.92	11.96±1.40	0.93

2.3.3 Data Acquisition

As previously described in detail[36], we used a multi-modal approach that combined laser speckle imaging (LSI), arterial blood pressure, and electroencephalography (EEG) to monitor CBF, femoral arterial blood pressure (ABP), and brain electrophysiology before, during, and after ACA and resuscitation. Briefly, LSI data was obtained using an 809nm laser as the excitation source and images acquired at ~60fps using a Point Grey camera with a 10ms exposure time. To measure ABP, systolic and diastolic blood pressures were recorded from the femoral artery at ~200Hz. The mean arterial pressure (MAP) was calculated at 1Hz from the extracted systolic and diastolic blood pressures waveforms. EEG data acquisition was recorded from each implanted electrode at 1526Hz with a first-order high-pass filter (0.35Hz).

2.3.4 Initial Data Processing

LSI processing used custom-written MATLAB code to process each raw speckle image and obtain CBF data. A sliding 5 x 5 square sliding window was used to convert each raw speckle image to a corresponding speckle contrast (K) image using the equation K =

σ/<I>, where σ is the standard deviation of the intensity and <I> is the average intensity within each window. Each speckle contrast image was then converted to a cerebral blood flow (CBF) map using a simplified speckle imaging equation $CBF = 1/2TK^2$, where K is the speckle contrast and T is the exposure time of the camera in seconds[46]. A representative region of interest (ROI) was then selected within the craniectomy to obtain an average SFI value and create time-resolved pulsatile CBF curves.

Raw EEG data were filtered using custom written MATLAB (Mathworks Inc., Natick, MA) code. Data were detrended and common average referencing was performed using each electrode[49]. A finite impulse response (FIR) notch filter at 60Hz was used, followed by a FIR bandpass filter from 1 to 150Hz. Signals were then downsampled to 600Hz to reduce memory and computational time.

2.3.5 Pulsatile Signal Analysis

To quantify CBF and ABP pulsatile waveform changes in response to ACA, two methods were used. The first method used the maximum value of the power spectrum (peak power), and the second the difference between the peak and trough values (peak-to-trough) of the pulsatile waveform signal (shown in Figure 2.3B). CBF and ABP data from each experiment were analyzed. Time periods during signal artifact due to bleeding, movement and noise, and ABG measurements were removed from further analysis.

To use the peak power from the power spectrum, an accurate measurement of heart rate is needed. Previous papers have used LSI to quantify the heart rate and pulsatile blood flow waveform flow from the skin[63] and teeth[64]. However, to our knowledge, LSI has not been used to obtain pulsatile CBF data. To ensure accurate CBF peak power quantification from the power spectrum, the CBF heart rate was compared to the gold standard ABP heart rate. See results (Figure 2.4) for comparison.

To obtain the heart rate and extract the peak power from the power spectrum, the following steps were performed for both the pulsatile CBF and ABP time courses. First, a bandpass filter from 0.5 to 10Hz was used to remove the DC component and very low and high frequency content. Next, the time-resolved power spectrum was computed using 10s intervals with 2s of overlap. During non-asphyxial periods, the maximum power in the 4 to 9Hz (240—540 beats/min, typical rat heart rate values) frequency band was extracted within each interval. During the asphyxial period, the maximum power from all frequencies was extracted within each interval. Time courses of peak power were then normalized to the baseline peak power, which is defined as the mean during a one-minute period immediately preceding the onset of asphyxia. The heart rate was computed by extracting the frequency that corresponded to the peak power. The heart rate calculated from the CBF data was compared to the heart rate calculated from the ABP data. The main steps to obtain the time courses of peak power are shown in Figure 2.1.

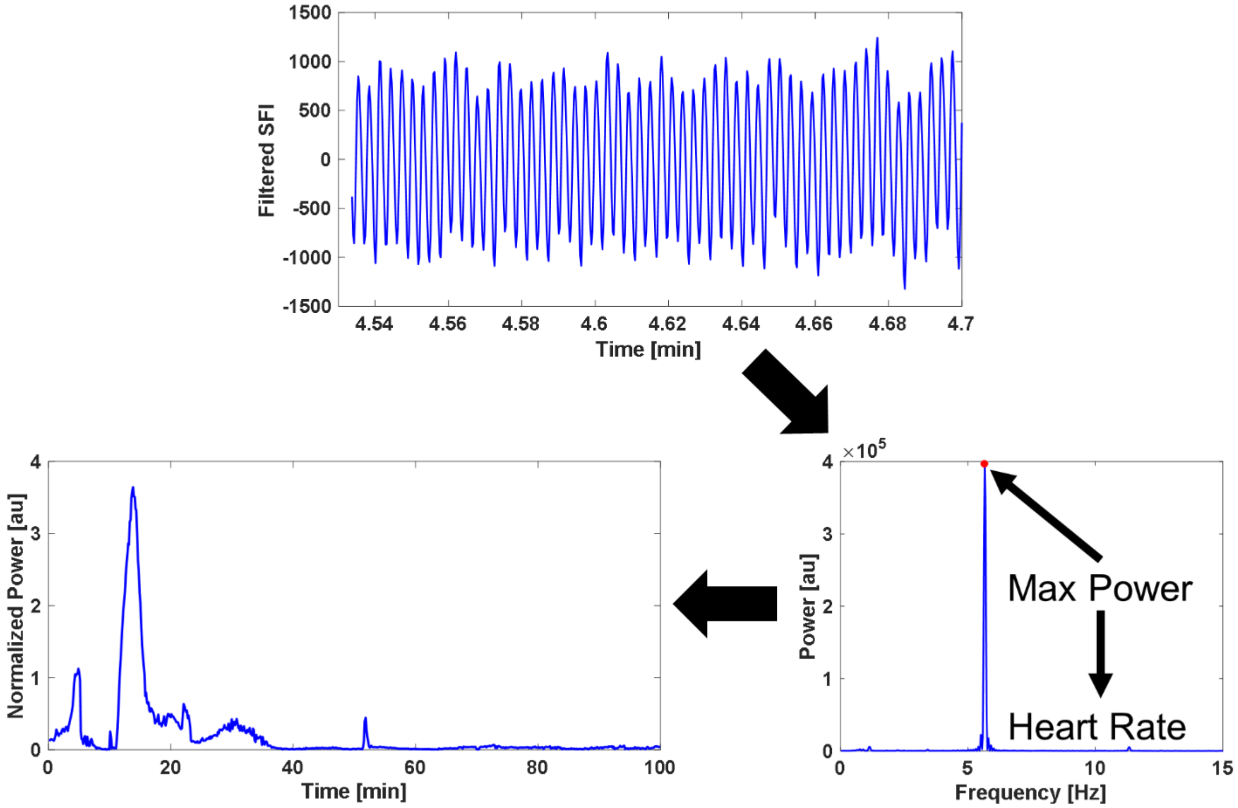

Figure 2.1: Data flow to extract normalized power time courses. After obtaining the filtered SFI time course, the power spectrum is computed. The max power is obtained, and the corresponding frequency is used to calculate the heart rate. Performing these two steps using a sliding window enables the time course of the power to be calculated, which is then normalized to the baseline power.

To calculate the peak-to-trough time courses from the pulsatile CBF and ABP signals, the following steps were performed. First, a bandpass filter from 0.5 to 10Hz was used to remove the DC component and very low and high frequency content. Next, peaks and troughs were determined over 1s intervals using the pulsatile signals for the entire time course. A 10s sliding average filter was applied to the peak and trough time courses separately. The difference between the filtered peak and trough time courses was calculated to obtain the peak-to-trough data. Time courses of peak-to-trough were then normalized to the baseline peak-to-trough, which is defined as the mean during a one-minute period immediately preceding the onset of asphyxia.

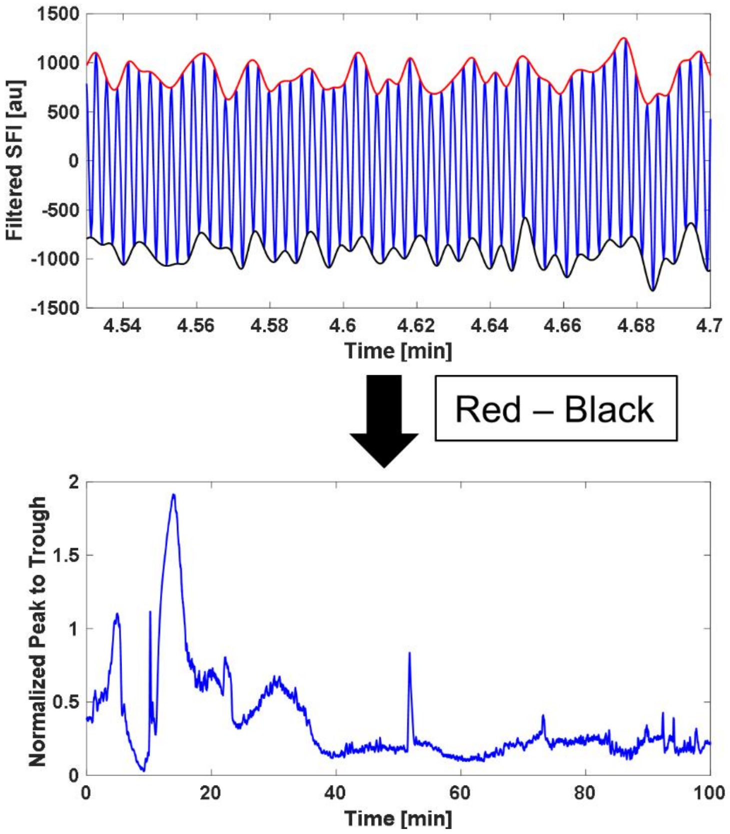

Figure 2.2: Data flow to extract normalized peak-to-trough time courses. After obtaining the filtered SFI time course, the peaks (red) and troughs (black) are found for the entire time course. The difference between the peaks and troughs is computed to obtain the peak-to-trough time course data. The peak-to-trough time course data is then normalized to the baseline peak-to-trough.

2.3.6 Cerebrovascular Resistance

Relative cerebrovascular resistance (rCVR) is defined as[65,66]:

$$rCVR(t) = rMAP(t)/rCBF(t) \qquad \text{(Eq. 2.1)}$$

rMAP is the MAP normalized by the baseline MAP, which is defined as the mean MAP calculated over a one-minute interval immediately prior to onset of asphyxia. rCBF, the relative CBF, was calculated as follows. A 10s sliding median filter was applied to the pulsatile CBF time courses to remove the pulsatile component. The filtered waveform was then normalized to the mean median-filtered CBF calculated over a one-minute interval immediately prior to onset of asphyxia. The rCBF data was then downsampled to 1Hz to match the rMAP data, and the rCVR calculated as the quotient of the two waveforms.

2.3.7 EEG IQ

To obtain a measurement of short-term neurological outcome, we used a quantitative EEG method called information quantity (IQ). The following steps were performed to obtain EEG IQ as a function of time. Using a temporal sliding window of 10s with 20% overlap, a 5-level discrete wavelet transform (DWT) was applied to the filtered EEG data to extract DWT coefficients. From the baseline EEG immediately one minute prior to onset of asphyxia, 20 fixed microstates were obtained that encompassed the mean ±3 standard deviations of the DWT coefficients. A histogram of the continuous EEG recording was created using the DWT coefficients with the 20 microstates. The probability distribution function was calculated, from the histogram, and the Shannon entropy was calculated using the equation: $SE = -\sum_{m=1}^{M} pdf(m) \log_2(pdf(m))$. SE is the Shannon entropy, M is the number of microstates, and pdf is the probability distribution function from the histogram. We used this equation within each window to calculate EEG IQ as a function of time. The EEG IQ was then normalized to the baseline EEG IQ, which is defined as the mean EEG IQ calculated over a one-minute interval immediately prior to onset of asphyxia. An EEG IQ of 0 indicates no brain electrical activity, while an EEG IQ of 1 indicates normal brain electrical activity.

2.3.8 Extracted Parameters and Statistical Analysis

To assess changes in CBF and ABP pulsatility, the peak power and peak-to-trough data was extracted over one minute intervals during baseline, CA, hyperemia, early hypoperfusion, and late hypoperfusion. These periods are labeled in Figure 2.3 as B-F and

G-K for the CBF and ABP data, respectively. Similarly, rCVR was extracted during the same time intervals. To determine the effects of asphyxial duration on peak power, peak-to-trough, and rCVR, a two-sided Wilcoxon ranked sum test was used to compare 5- and 7-min ACA at baseline, CA, hyperemia, early hypoperfusion and late hypoperfusion. To determine the response of peak power, peak-to-trough, and rCVR following ACA, a two-sided, paired Wilcoxon signed rank test was used. To determine the association between pulsatility and rCVR, a Spearman ranked correlation was used.

To obtain a metric of short-term neurological recovery, the median EEG IQ from 90 to 100min post-ROSC was determined[67,68]. To assess the relationship between pulsatility and short-term neurological recovery, a Spearman ranked correlation was used.

2.4 Results

Following resuscitation from asphyxial cardiac arrest, cerebral blood flow and femoral artery, pulsatility characteristics vary considerably (Figure 2.3). Figure 2.3A shows representative time courses of CBF (top) and ABP (bottom) following ACA and resuscitation experiment. Figure 2.3B-F shows representative 1.5s periods of CBF data during specific phases labeled in Figure 2.3A (top). The y-axis of Figure 2.3B-F is rescaled to keep the same CBF range in each sub-figure. Figure 2.3B shows baseline (B) pulsatile CBF waveform with example of the peak and trough labeled. Figure 2.3C shows CBF pulsatility during cardiac arrest (CA) with low amplitude and overall low flow. Figure 2.3D shows CBF pulsatility during hyperemia (H). Compared to B, the CBF waveform in this phase is higher in amplitude and consists of narrower features. Figure 2.3E shows CBF pulsatility during early hypoperfusion (EH). The CBF pulsatility has a lower amplitude than during both H and B, with overall lower flow. Figure 2.3F shows CBF pulsatility during late hypoperfusion (LH). The CBF pulsatility has a lower amplitude than during both H and B, with overall lower flow. During B, H, and EH respiratory variations are observed as a slow frequency oscillation in the CBF data which are not observed during CA and are difficult to visualize during LH.

Figure 2.3G-K shows representative 1.5s periods of ABP data during the same specific phases labeled in Figure 2.3A (bottom). The y-axis of Figure 2.3G-K is rescaled to keep the same blood pressure range in each sub-figure. Figure 2.3G shows the pulsatile ABP waveform during B. Figure 2.3H shows the pulsatile ABP during CA, with a nearly featureless waveform. Figure 2.3I shows ABP pulsatility during H, with a return in pulsatility and a slightly higher amplitude than during B. Figure 2.3J shows ABP pulsatility during EH. Unlike the decreased CBF pulsatility during EH, the ABP pulsatility is near baseline levels. Figure 2.3K shows ABP pulsatility during LH, with similar pulsatility to EH. During B, H, EH, and LH, respiratory variations are observed as a slow frequency oscillation in the ABP data which are not observed during CA.

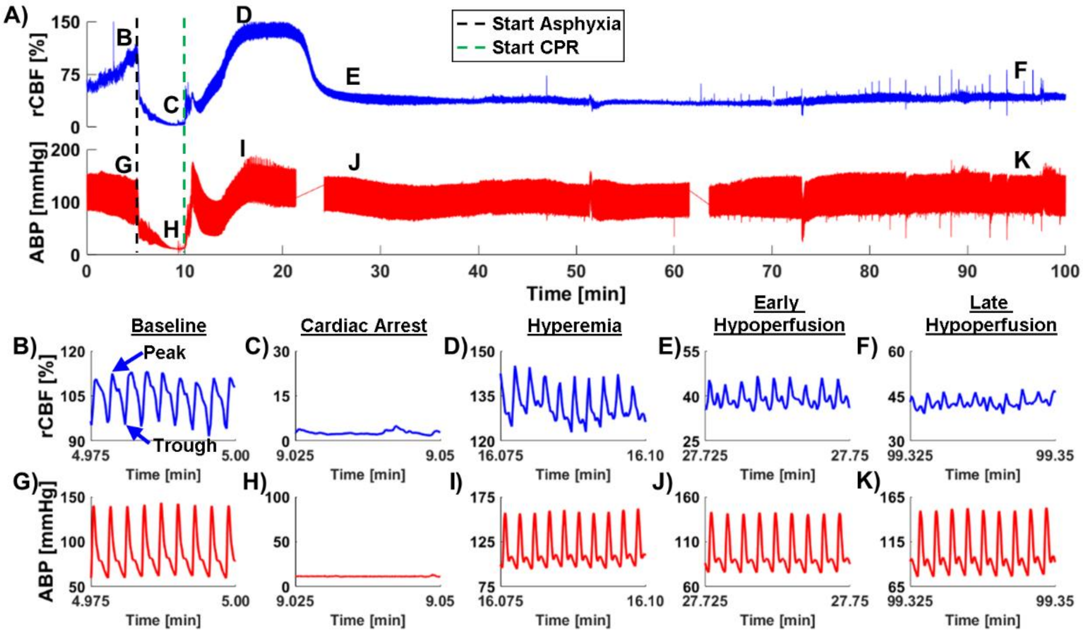

Figure 2.3: Qualitative assessment of pulsatile CBF and ABP changes following resuscitation from ACA. (A) CBF (top, blue) and ABP (bottom, red) time courses during a representative ACA and resuscitation experiment. (B-F) 1.5s periods of CBF data of phases labeled in (A, top), and the y-axis is rescaled to keep the same CBF range in B through F. (B) Baseline pulsatile CBF. (C) CA pulsatile CBF. (D) Hyperemia pulsatile CBF. (E) Early hypoperfusion pulsatile CBF. (F) Late hypoperfusion pulsatile CBF. (G-K) 1.5s of ABP data of zoomed-in plots labeled in (A, bottom) and the y-axis is rescaled to keep the same blood pressure range in G through K. (G) Baseline pulsatile ABP. (H) CA pulsatile ABP. (I) Hyperemia pulsatile ABP. (J) Early hypoperfusion phase of pulsatile ABP. (K) Late hypoperfusion phase of pulsatile ABP.

LSI enables accurate quantification of heart rate measured from the rodent brain (Figure 2.4). To determine if LSI is able to quantitatively resolve CBF heart rate changes, heart rate calculations measured from LSI data was compared to the ABP heart rate as the gold standard. Figure 2.4A shows time courses of heart rate calculations measured from each experiment using CBF data (blue) and ABP data (red). The data collectively show excellent agreement across all experiments. Figure 2.4B quantifies the linear relationship between the heart rate calculated using all CBF and ABP data. The linear relationship was examined in three periods: 1) only asphyxial time points (left), 2) only non-asphyxial time points (middle), and 3) combined asphyxial and non-asphyxial time points (right). Using only asphyxial time points (n = 358) the $R^2 = 0.80$, using only non-asphyxial time points (n = 4615) the $R^2 = 0.93$, and using all experimental time points (n = 4973) the $R^2 = 0.94$.

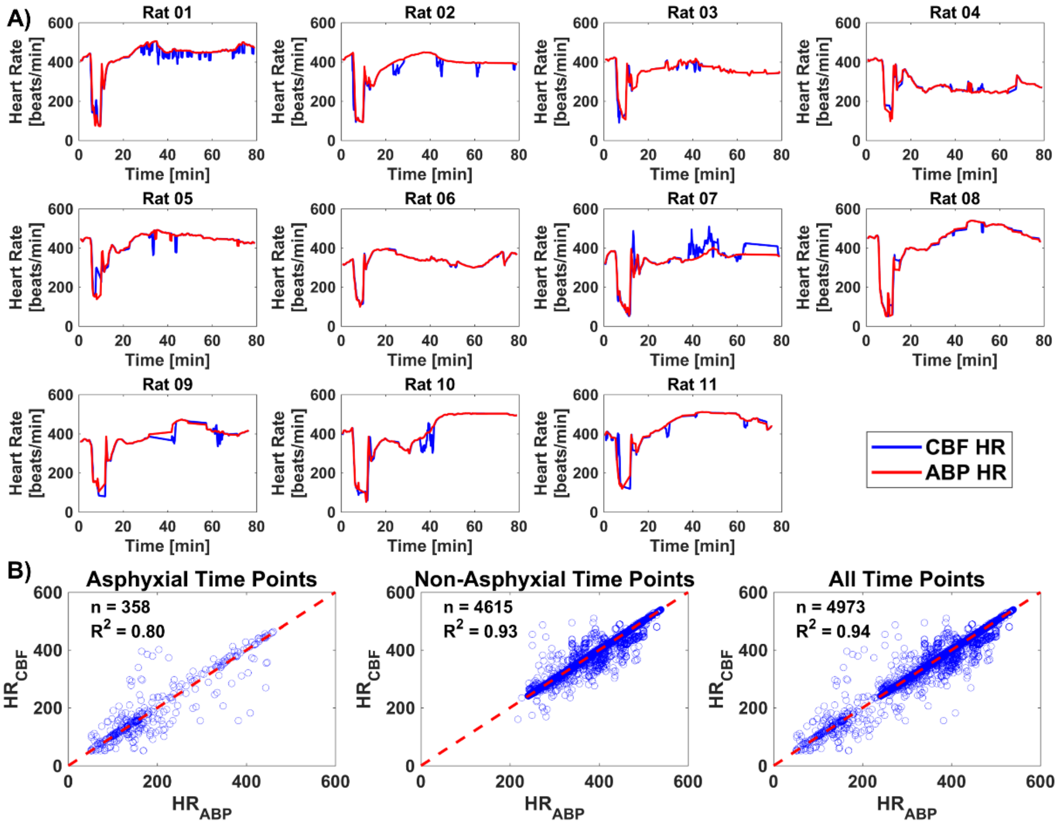

Figure 2.4: CBF heart rate calculations agree well with ABP heart rate calculations during all experimental phases. (A) Time courses from each experiment that compares ABP and CBF heart rate calculations. Data from LSI is in blue and data from peripheral ABP is in red (B) Comparison of ABP and CBF heart rate calculations from all experiments during asphyxial (left; n = 358, $R^2 = 0.80$), non-asphyxial (middle; n = 4615, $R^2 = 0.93$), and all experimental time points (right; n = 4973, $R^2 = 0.94$).

Asphyxial duration leads to differences in ABP pulsatility only during the late hypoperfusion phase (Figure 2.5). To assess the effects of asphyxial duration on CBF and ABP pulsatility, 5- and 7-min ACA were compared during CA, H, EH, and LH. There were no significant differences between the normalized peak power and peak-to-trough CBF pulsatility metrics for 5- and 7-min ACA experiments during all time points ($p > 0.05$) [Figure 3(A,B)]. There was no significant difference between the normalized peak power and peak-to-trough ABP pulsatility metrics for 5- and 7-min ACA experiments during CA, H, and EH ($p > 0.05$) [Figure 2.5(C,D)]. However, during LH, 7-min ACA experiments had significantly more ABP pulsatility than 5min ACA experiments, using both the normalized peak power (p = 0.03) and normalized peak-to-trough (p = 0.03) pulsatility metrics [Figure 2.5(C,D)].

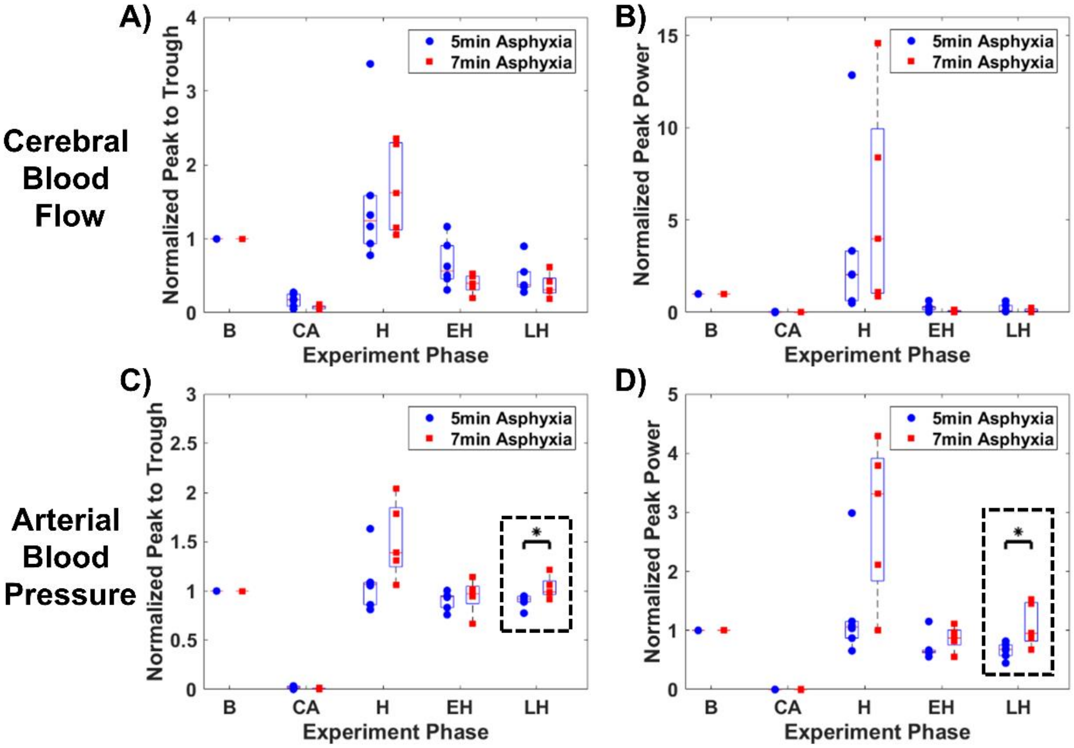

Figure 2.5: Asphyxial duration does not influence CBF pulsatility, but longer asphyxial duration leads to increased ABP pulsatility. (A and B) Two methods of CBF pulsatility (normalized peak to trough and peak power) demonstrate that there is no significant difference between 5- and 7-min ACA experiments during CA, hyperemia, and early and late hypoperfusion. (C and D) Two methods of ABP pulsatility (normalized peak to trough and peak power) demonstrate that there is no significant difference between 5- and 7-min ACA experiments during CA, hyperemia, and early hypoperfusion ($p > 0.05$). During late hypoperfusion, 7-min ACA experiments have significantly more pulsatility than 5-min experiments ($p = 0.03$). Experimental phases are baseline (B), cardiac arrest (CA), hyperemia (H), early hypoperfusion (EH), and late hypoperfusion (LH), respectively.

Response of CBF and ABP pulsatility to ACA and resuscitation differs (Figure 2.6). To assess differences between CBF and ABP pulsatility, the 5- and 7-min ACA groups were combined for further analysis. There is no significant difference between CBF and ABP pulsatility during H (peak-to-trough: $p = 0.15$; peak power: $p = 0.12$), but there is a significant difference between CBF and ABP pulsatility during EH (peak-to-trough: $p = 0.003$; peak power: $p < 0.001$) and LH (peak-to-trough: $p < 0.001$; peak power: $p < 0.001$).

We then compared baseline CBF and ABP pulsatility metrics to the same metrics during CA, hyperemia, early hypoperfusion, and late hypoperfusion pulsatility. CA ABP pulsatility is significantly less than baseline ABP pulsatility (peak-to-trough: $p < 0.001$; peak power: $p < 0.001$). CA CBF pulsatility is significantly less than baseline CBF pulsatility (peak-to-trough: $p < 0.001$; peak power: $p < 0.001$). CBF pulsatility at baseline is significantly less than CBF pulsatility during H (peak-to-trough: $p = 0.02$; peak power: $p = 0.03$), and significantly greater during EH (peak-to-trough: $p = 0.003$; peak power: $p < 0.001$) and LH (peak-to-trough: $p < 0.001$; peak power: $p < 0.001$). ABP pulsatility at baseline is significantly different than ABP pulsatility during EH (peak power: $p = 0.01$). During H and LH, ABP pulsatility is not significantly different from the baseline values.

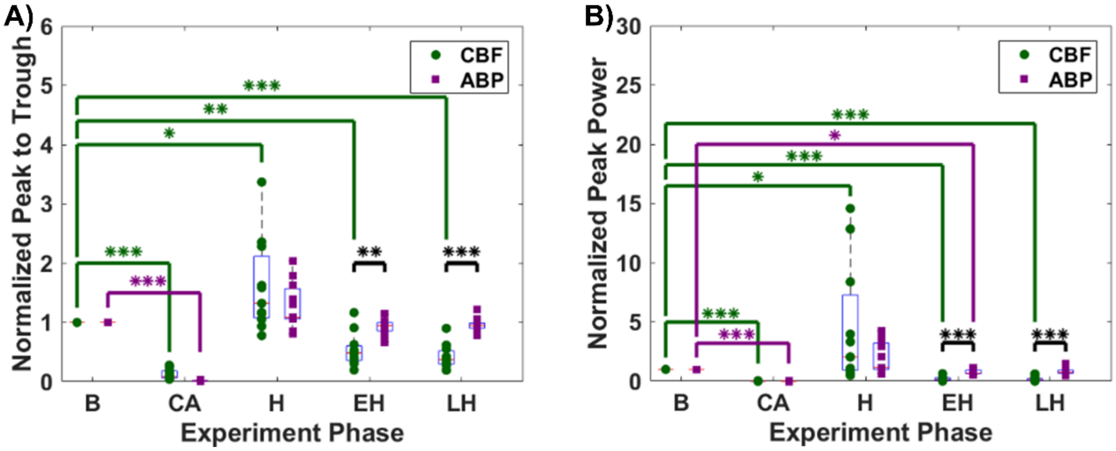

Figure 2.6: Resuscitation after ACA leads to decreased CBF pulsatility, but ABP pulsatility minimally changes. Comparison between CBF (green, circle) pulsatility and ABP (purple, square) pulsatility using normalized (A) peak-to-trough metric and (B) normalized peak power metric. Experimental phases are baseline, denoted with letter B, cardiac arrest, denoted with letters CA, hyperemia, denoted with letter H, early hypoperfusion, denoted with letters EH, and late hypoperfusion, denoted with letters LH. * signifies $p < 0.05$, ** signifies $p < 0.01$, and *** signifies $p < 0.001$

Cerebrovascular resistance is correlated to CBF pulsatility, but not ABP pulsatility (Figure 2.7). Figure 2.7A illustrates a representative experimental rCVR time course. Figure 2.7B demonstrates that baseline rCVR is significantly different from rCVR during CA ($p < 0.001$), EH ($p = 0.002$), and LH ($p < 0.001$). However, rCVR during baseline and H are non-significantly different.

There is a significant negative correlation between CBF pulsatility and rCVR during H ($R = -0.68$, $p = 0.025$) and LH ($R = -0.78$, $p = 0.007$). There is a non-significant correlation, but a negative trend between CBF pulsatility and rCVR, during EH ($R = -0.42$, $p = 0.20$). In contrast, there is no significant correlation between ABP pulsatility and rCVR during H ($R = 0.04$, $p = 0.92$), EH ($R = 0.34$, $p = 0.31$), and LH ($R = 0.16$, $p = 0.63$).

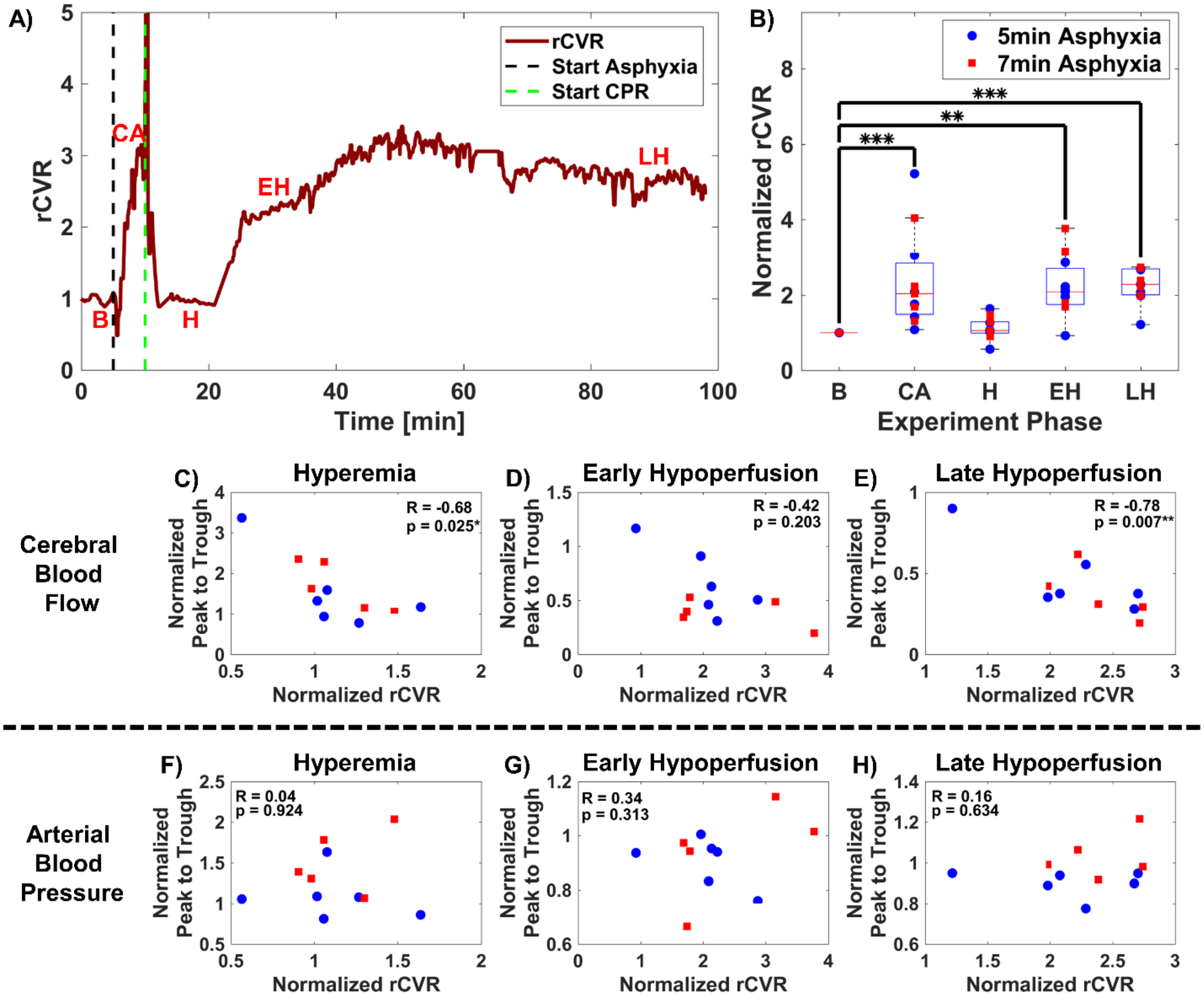

Figure 2.7: ACA increases rCVR after resuscitation and is correlated to CBF pulsatility but not ABP pulsatility. (A) Representative experiment illustrating temporal changes in rCVR. (B) rCVR is significantly elevated during CA ($p < 0.001$), and early ($p = 0.002$) and late hypoperfusion ($p < 0.001$), while rCVR remains at near baseline levels during hyperemia ($p = 0.17$). Experimental phases are baseline, denoted with letter B, cardiac arrest, denoted with letters CA, hyperemia, denoted with letter H, early hypoperfusion, denoted with

letters EH, and late hypoperfusion, denoted with letters LH. (C-E) Comparison between CBF normalized peak to trough data and rCVR during hyperemia, early hypoperfusion, and late hypoperfusion. (C) Comparison between CBF pulsatility and normalized rCVR during hyperemia (R = -0.68, p = 0.025). (D) Comparison between CBF pulsatility and normalized rCVR during early hypoperfusion (R = -0.42, p = 0.20). (E) Comparison between CBF pulsatility and normalized rCVR during late hypoperfusion (R = -0.78, p = 0.007). (F-H) Comparison between ABP normalized peak to trough data and normalized rCVR during hyperemia, early hypoperfusion, and late hypoperfusion. (F) Comparison between ABP pulsatility and normalized rCVR during hyperemia (R = 0.04, p = 0.92). (G) Comparison between ABP pulsatility and normalized rCVR during early hypoperfusion (R = 0.34, p = 0.31). (H) Comparison between ABP pulsatility and normalized rCVR during late hypoperfusion (R = 0.16, p = 0.63).

In general, CBF and ABP pulsatility metrics do *not* predict short-term neurological outcome (Figure 2.8). Figure 2.8A illustrates a representative experimental EEG IQ time course. As seen in Figure 2.8(B-D), there is no significant trend between EEG IQ 90min post-ROSC and CBF peak-to-trough during H (R = -0.20, p = 0.58), EH (R = 0.21, p = 0.56), and LH (R = 0.13, p = 0.73). There is no significant trend between EEG IQ 90min post-ROSC and ABP peak-to-trough during H (R = -0.32, p = 0.37) and EH (R = -0.52, p = 0.13). However, there is a significant negative trend comparing EEG IQ 90min post-ROSC and ABP peak-to-trough during late hypoperfusion (R = -0.76, p = 0.016) (Figure 2.8G).

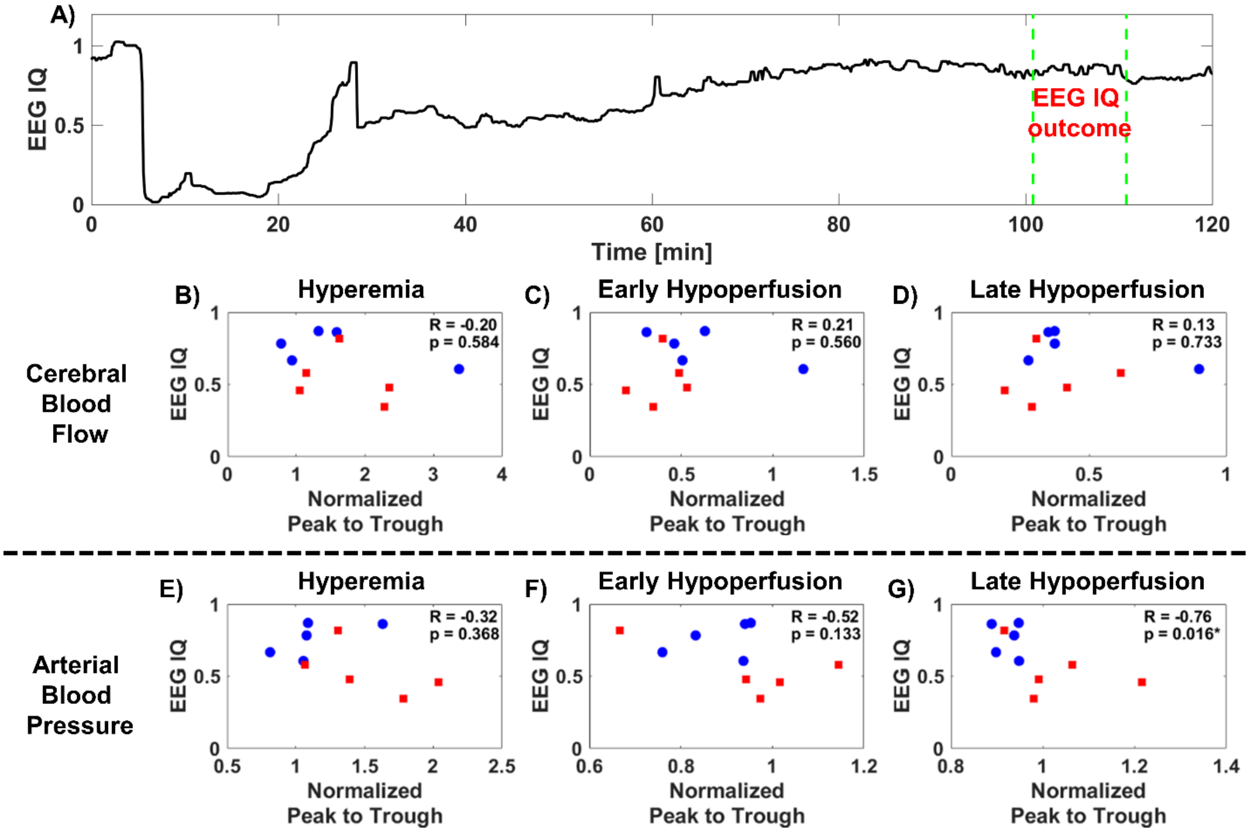

Figure 2.8: Changes in CBF pulsatility do not influence short-term neurological recovery, while increased ABP pulsatility is associated with worse short-term neurological recovery. (A) Representative experiment that shows temporal changes in EEG IQ. (B-D) Comparisons between CBF normalized peak to trough data during hyperemia, early hypoperfusion, and late hypoperfusion to EEG IQ 90min post-ROSC. (B) Comparison between CBF pulsatility during hyperemia and EEG IQ 90min post-ROSC (R = -0.20, p = 0.58). (C) Comparison between CBF pulsatility during early hypoperfusion and EEG IQ 90min post-ROSC (R = 0.21, p = 0.56). (D) Comparison between CBF pulsatility during late hypoperfusion and EEG IQ 90min post-ROSC (R = 0.13, p = 0.73). (E-G) Comparisons between ABP normalized peak-to-trough data during hyperemia, early hypoperfusion, and late hypoperfusion to EEG IQ 90min post-ROSC. (E) Comparison between ABP pulsatility during hyperemia and EEG IQ 90min post-ROSC (R = -0.32, p = 0.37). (F) Comparison between ABP pulsatility during early hypoperfusion and EEG IQ 90min post-ROSC (R = -0.52, p = 0.13). (G) Comparison between ABP pulsatility during late hypoperfusion and EEG IQ 90min post-ROSC (R = -0.76, p = 0.016).

2.5 Discussion

Pulsatile blood flow is important because of its impact on oxygen uptake, vascular tone, and cellular metabolism[69]. Previous studies have investigated pulsatility following CA[14,24,23,70]; however, they have examined patients after admission to the ICU, have not examined acute changes in CBF and ABP pulsatility, and have rarely compared CBF and ABP pulsatility to neurological outcome. In this study, we used a clinically-translatable preclinical model of ACA and multi-modal platform[36] to demonstrate several key associations between acute CBF and ABP pulsatility changes immediately after resuscitation from ACA and their relationship to rCVR and short-term neurological outcome. First, we show that different severities of ACA do not influence CBF pulsatility, but more severe ACA is associated with increased ABP pulsatility during late hypoperfusion (Figure 2.5). Next, we show that CBF and ABP pulsatility differ significantly during the hypoperfusion period after resuscitation from ACA (Figure 2.6). Furthermore, CBF pulsatility is significantly different from baseline during all points in the experiment, while ABP pulsatility is only significantly different from baseline during CA (Figure 2.6A). In addition, rCVR is associated with changes in CBF pulsatility, but not ABP pulsatility (Figure 2.7). Finally, the key result of the paper is that CBF pulsatility does not influence short-term neurological outcome, but increased ABP pulsatility is associated with worse short-term neurological outcome (Figure 2.8).

Poor neurological recovery remains a common occurrence for CA survivors. After resuscitation from CA it is known that overall CBF is diminished, while ABP recovers to baseline levels[35,36]. van den Brule et al[35], and others have shown that the low frequency pulsatile component of CBF and MAP is decreased after resuscitation from CA. Furthermore, these studies showed that increased variability in CBF and MAP signals 72h after admission to the ICU were associated with a higher chance of survival[35,34]. These studies suggested that alterations in low frequency variability is associated with impaired myogenic response and autonomic regulation[35], and excessive vasoactive components[51]. Our results demonstrate that the heartrate frequency of pulsatile CBF decreased after resuscitation, while ABP pulsatility remained similar to baseline levels (Figure 2.6). We postulate that the difference between CBF and ABP pulsatility is due to autonomic dysregulation and changes in CVR. Previous studies show that CVR is elevated during the hypoperfusion phase after resuscitation[71], which is in agreement with our data (Figure 2.7B). However, previous studies did not compare CVR to CBF and ABP pulsatility. Our imaging approach provided the requisite capabilities to demonstrate that CVR is associated with CBF pulsatility but not ABP pulsatility (Figure 2.7C-H). Collectively, these data suggest that the brain is attempting to minimize the pulsatile CBF it receives.

CA[14,24,70] and non-CA[60,72–74] studies have examined the heartrate frequency to quantify CBF and ABP pulsatility. Based on the collective published results, controversy exists regarding whether higher or lower pulsatility is related to better neurological outcome. For example, the following results have been reported: 1) CA studies have examined the MCA and showed that a lower PI is associated with good outcome[14], 2) there is no relationship between PI and survivability up to 72h after admission to the ICU[24], and 3) the good neurological outcome group had higher PIs in the initial 48h after admission to the ICU[70]. Results by van den Brule et al[35] and Lemiale et al[24] suggest that pulsatile CBF changes are due to increased level of vasoconstrictors and cerebral arterial resistance, but that mortality depends on the presence of luxury perfusion. However, the CA studies do not comment on how CBF pulsatility impacts neurological outcome. Non-CA studies showed that patients with higher pulse pressure, which is analogous to ABP peak-to-trough measured in this study, have 1) increased likelihood to develop restenosis after percutaneous transluminal coronary angioplasty[72], 2) increased central pulse pressure and carotid PI with higher prevalence of subcortical infarcts and worse cognitive function in the aging population[73], 3) increased aortic pulse pressure and MCA PI was associated with more severe forms of leukoaraiosis[60], and 4) higher carotid artery PI is associated with higher incidence of stroke[74].

Mitchell et al[73] and Webb et al[60] state that increased stiffening of the aorta is associated with reduced wave reflection and therefore, transmission of excessive pulsatility into the brain can lead to microvascular structural brain damage and impaired cognitive function[60,73]. The results in the present study are in agreement with this, as we show that increased ABP pulsatility is associated with worse short-term neurological outcome (Figure 2.8G). However, the findings these studies are due to chronic increases in pulsatility, which led to cerebral microvascular problems. The results presented in our study are related to short-term changes in ABP pulsatility that occur over the course of less than 2h. Upon examination of the correlation coefficient and p-values from Figure 2.8E through 2.8G, the correlation coefficient increases from hyperemia (Figure 2.8E) to late hypoperfusion (Figure 2.8G), suggesting that a further increase in measurement time may yield a stronger correlation. In sum, although the data shows that CBF pulsatility is not associated to short-term neurological outcome, potentially due to the influence of CVR (Figure 2.7), the data suggests that increased levels of ABP pulsatility worsen short-term neurological outcome. Future studies should focus on analyses of CBF and ABP pulsatility in conjunction with administration of different therapeutics to determine optimal drug selection during CPR and improve neurological recovery after resuscitation from CA.

Although the findings of this study warrant further investigations, there are several limitations. First, global ROIs over the craniectomy were chosen for the CBF data, and therefore did not separate between arteriolar and venular pulsatility. In separate analyses, ROIs were taken exclusively from arterioles, resulting in a decreased signal-to-noise ratio of the pulsatile waveform. Although the data analyses produce statistical significance and trends, the power of these findings is limited due to the small sample size and complexity of experiments. Furthermore, these experiments used a full craniectomy, which may change the intracranial pressure and affect pulsatile CBF changes. A chronic cranial window may mitigate such effects. In addition, the correlations in this study combined the 5-and 7-min ACA groups due to the small sample size. The correlations should be done in larger, separate groups and utilize linear regression models. Furthermore, our metric of neurological outcome, which has been correlated to more accepted outcomes[67,68], is not based on cognitive, behavioral, or histopathological outcomes. Finally, the results in this study only measured acute pulsatility changes. Use of a wearable imaging device[75] will enable chronic monitoring of CBF pulsatility.

2.6 Conclusions

In conclusion, we used our preclinical model of ACA and multi-modal platform to demonstrate several key associations between acute CBF and ABP pulsatility changes immediately after resuscitation from ACA and their relationship to rCVR and short-term neurological outcome. Our results demonstrate that rCVR is related to changes in CBF pulsatility, but not ABP pulsatility. We also demonstrate that CBF pulsatility does not influence short-term neurological outcome, but increased ABP pulsatility is associated with worse short-term neurological outcome. Collectively, our findings indicate the importance of investigating acute CBF and ABP pulsatility immediately following resuscitation from CA. However, future studies that modify and monitor CBF and ABP pulsatility are required to assess their effects on neurological outcome.

2.7 Acknowledgements

This work was supported by the Arnold and Mabel Beckman Foundation, the United States National Institutes of Health (P41EB015890), the National Science Foundation Graduate Research Fellowship Program (DGE-1321846, to C.C.), the National Center for Research Resources and National Center for Advancing Translational Sciences, National Institutes of Health, through the following grants: TL1TR001415-01 to R. H.W., R21 EB024793 to Y. A., and 5KL2TR000147 to Y.A. via UL1 TR001414. The content is solely the responsibility of the authors and does not necessarily represent the official views of the NIH.

CHAPTER 3: Spreading cerebral blood flow waves during cardiac arrest and after resuscitation

3.1 Abstract

Background— Our previous studies assessed cerebral blood flow (CBF), arterial blood pressure, and brain electrophysiology in a preclinical model of CA (global ischemia) and resuscitation. Dr. Akbari's lab has visualized spreading depolarizations (SDs) as ultra-slow potential waves (<1Hz) using AC-electrocorticography. An extremely powerful and potentially clinically translatable finding is that the earlier the onset of SD in rats that underwent 8-min ACA, the better the neurological outcome 24h following resuscitation. In this study we explored spatiotemporal CBF changes during three hyperdynamic periods: (1) entering CA, (2) within 5min after resuscitation, and (3) from hyperemia to hypoperfusion (i.e., 5 to 20min after resuscitation).

Methods and Results—Male Wistar rats were subjected to either 5- or 7-min of ACA followed by cardiopulmonary resuscitation. A multi-modal platform that combined laser speckle imaging (LSI), ABP, and electroencephalography (EEG) was used to monitor CBF, peripheral blood pressure, and brain electrophysiology, respectively. Spreading CBF waves were visualized during each phase. We found that an increase in total CBF prior to the onset of spreading wave (1) was associated with worse neurological outcome, waves (1) and (3) propagated in opposite directions, and waves (2) and (3) resembled a well-known phenomenon called cortical spreading depression.

Conclusions—Our results demonstrate that there are complex spatiotemporal changes in CBF that occur before, during, and after CA and resuscitation, and modifying the timing of these spatial CBF changes may lead to changes in neurological outcome.

3.2 Introduction

Our previous studies have assessed cerebral blood flow (CBF), arterial blood pressure, and brain electrophysiology. Specifically, we examined the temporal evolution of CBF prior to the moment brain electrical activity resumes after resuscitation (Chapter 1)[36]. Furthermore, we examined the effects of pulsatile CBF and femoral arterial blood pressure (ABP) waveforms in response to CA and resuscitation, and how they affect short-term neurological outcome (Chapter 2). However, both these studies lacked the analysis of spatiotemporal CBF changes that occur before, during, and after CA and resuscitation.

In animals, global cerebral ischemia leads to complete electrocerebral silence within ~30seconds[76,77]. This period has been called nonspreading depression, as brain electrical activity becomes silent everywhere, and does not propagate from multiple locations. After a period of 1 to 5min from the onset of nonspreading depression, the ion gradients across cellular membranes completely break down[78]. This is termed anoxic depolarization, which is a spreading depolarization (SD) that may begin in multiple locations and spatially spread in the tissue at a rate of 2-6mm/min[77]. Previous studies have shown the propagation of SDs in rats and humans through the use of voltage-sensitive dyes[79,37] and multiple DC and AC electrodes[76]. Furthermore, *in vitro* studies using optical intrinsic signal imaging (OISI) have shown SDs occur in brain sections[39]. However, to my knowledge, no study has reported visualization of spatial CBF changes that occur during SD in global ischemia models, which may be due to a lack of capable technologies or not enough signal-to-noise.

SDs are important for a wide-range of different clinical applications. Not only do SDs occur during CA, but also during focal-ischemic stroke[80,81], traumatic brain injury[38,82,83], subarachnoid hemorrhage[84] and migraines[85]. During CA, a single terminal SD occurs.

However, during focal-ischemic stroke, traumatic brain injury, and migraines, SDs can be recurrent. In non-global ischemia studies, spatial changes in CBF have been reported. These changes are characterized as a wave of increased CBF or hyperemia that is followed by a wave of decreasing CBF and remains in a decreased CBF or oligemic state for a period of time[84,86,87]. In these studies, recurrent SD events have typically been associated with worse neurological outcome[84]. However, the relationship between terminal SDs and neurological recovery is poorly understood, due to the limited ability to examine post-resuscitation dynamics following terminal SD.

Dr. Yama Akbari's lab has developed a preclinical model of CA (global ischemia) and resuscitation. Due to resuscitation being a critical component of the preclinical model, the relationship between features that occur during CA, such as terminal SDs, and neurological outcome can be investigated. During CA, Dr. Akbari's lab has visualized SDs as ultra-slow potential waves (<1Hz) using AC-electrocorticography. An extremely powerful and potentially clinically translatable finding is that earlier onset of SD in rats that underwent 8-min ACA, the better the neurological outcome 24h following resuscitation (Figure 3.1).

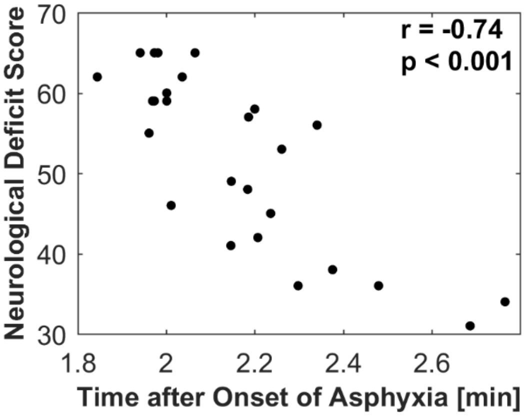

Figure 3.1: Earlier EEG slow-wave is correlated with better neurological outcome. The onset of the SD is plotted on the x-axis, and the neurological outcome on the y-axis. The neurological deficit score (NDS) is measured between 0-70, where 70 is the best neurological outcome, and 0 is the worst neurological outcome.

Although SDs, in general, have been fairly characterized, a large number of recent studies involving SDs highlight their importance. Based on previous studies and Dr. Akbari's preliminary data, we decided to conduct an exploratory study of spatiotemporal CBF changes that occur during hyperdynamic periods associated with CA and resuscitation. We focused on three main time-periods based on our previous data: (1) during the same time interval that typical SDs occur, (2) immediately after resuscitation prior to the hyperemic peak, and (3) from the hyperemic peak to the stabilized hypoperfusion period. Surprisingly, we visualized spreading CBF changes during each phase. A spreading wave during phase (1) was associated with a spatial decrease in CBF that resembled a "spreading ischemia" wave seen in stroke literature[88,89]. A spreading wave during phase (2) was associated with a spatial increase in CBF the resembled a "spreading hyperemia" wave. A spreading wave during phase (3) was associated with a spatial decrease in CBF that resembled the "spreading ischemia" wave, and we called the "spreading oligemia" wave due to CBF remaining at a higher level. Due to the novel preclinical CA and resuscitation model, these results show that there are complex spatiotemporal CBF changes that occur before, during, and after CA and resuscitation, and these spatial changes in CBF may have clinical importance to neurological outcome.

3.3 Materials and Methods

3.3.1 Animal Preparation

The ACA model and study protocol (no. 2013-3098) were approved by the Institutional Animal Care and Use Committee at University of California, Irvine.

We used our ACA model to perform experiments on 11 adult male Wistar rats[36,61,62]. Rats were calorically restricted 12-16h prior to onset of CA. On the day of CA induction, rats were anesthetized, intubated, and connected to a mechanical ventilator (Kent Scientific, Torrington, CT). During surgery, isoflurane was maintained at 2% with a 50%/50% N2/O2 mixture at 2LPM. The ventilation settings were maintained at 70 breaths per min (BPM), with 12–14cmH2O peak inspiration pressure (PIP) and 3cmH2O peak end expiratory pressure (PEEP). Animal temperature was continuously measured with a rectal thermometer (Kent Scientific, Torrington, CT) and maintained between 36.5 and 37.5oC. The rat was then positioned on a stereotactic frame (Kopf Instruments, Tujunga, CA).

A midline incision was performed over the scalp and the scalp retracted to expose the skull for EEG electrode implantation (Plastics One Inc., Roanoke, VA). Two frontal electrodes were implanted 2mm anterior and 2.5mm lateral to bregma, and one electrode was implanted over the visual cortex 5.5mm posterior and 4mm left of bregma. A reference electrode was implanted 3mm posterior to lambda. Following EEG electrode implantation, a 4mm x 6mm craniectomy was created over the right sensory and visual cortices to create a window for optical imaging. Saline was applied periodically to ensure the brain remained hydrated. Following the craniectomy, the femoral artery and vein were cannulated. Invasive arterial blood pressure from the femoral artery was measured continuously at ~200Hz. Baseline arterial blood gas (ABG) measurements (Abaxis, Union City, CA) were obtained within 30min prior to initiation of ACA.

3.3.2 Experimental Protocol

At experiment start time, rats were placed on 0.5–1% isoflurane (balance 100% O_2). After 2min, inhaled air was changed to room air (21% O_2), isoflurane administration turned off to wash out anesthesia, and neuromuscular blockade initiated with 1mL of intravenous Vecuronium (2mg/kg), flushed with 1mL of heparinized saline. At 5min, asphyxia was initiated by turning the ventilator off and clamping the tubing. Rats were subjected to a period of either 5- (n=6) or 7- (n=5) min asphyxia. Thirty seconds prior to end of asphyxial period, mechanical ventilation was re-initiated at 100% O_2 with respiratory rate of 75–85BPM, PIP of 17.5–18.5 cmH_2O, and PEEP of 3cmH_2O at 2.5LPM. Epinephrine (0.01mg/kg) and sodium bicarbonate (1mmol/kg), followed by 2mL of heparinized saline, were administered intravenously. Chest compressions were started at end of asphyxial period until return of spontaneous circulation (ROSC) was achieved. ABGs were obtained 10-min post-ROSC and every 40 min thereafter, to assess and modify ventilator settings as necessary.

3.3.3 Data Acquisition

As previously described in detail[36], we used a multi-modal approach that combined laser speckle imaging (LSI), arterial blood pressure, and electroencephalography (EEG) to monitor CBF, femoral arterial blood pressure (ABP), and brain electrophysiology before, during, and after ACA and resuscitation (Figure 3.2). Briefly, LSI data was obtained using an 809nm laser as the excitation source and images acquired at ~60fps using a Point Grey camera with a 10ms exposure time. The mean arterial pressure (MAP) was calculated at 1Hz from the extracted systolic and diastolic blood pressures waveforms. EEG data acquisition was recorded from each implanted electrode at 1526Hz with a first-order high-pass filter (0.35Hz).

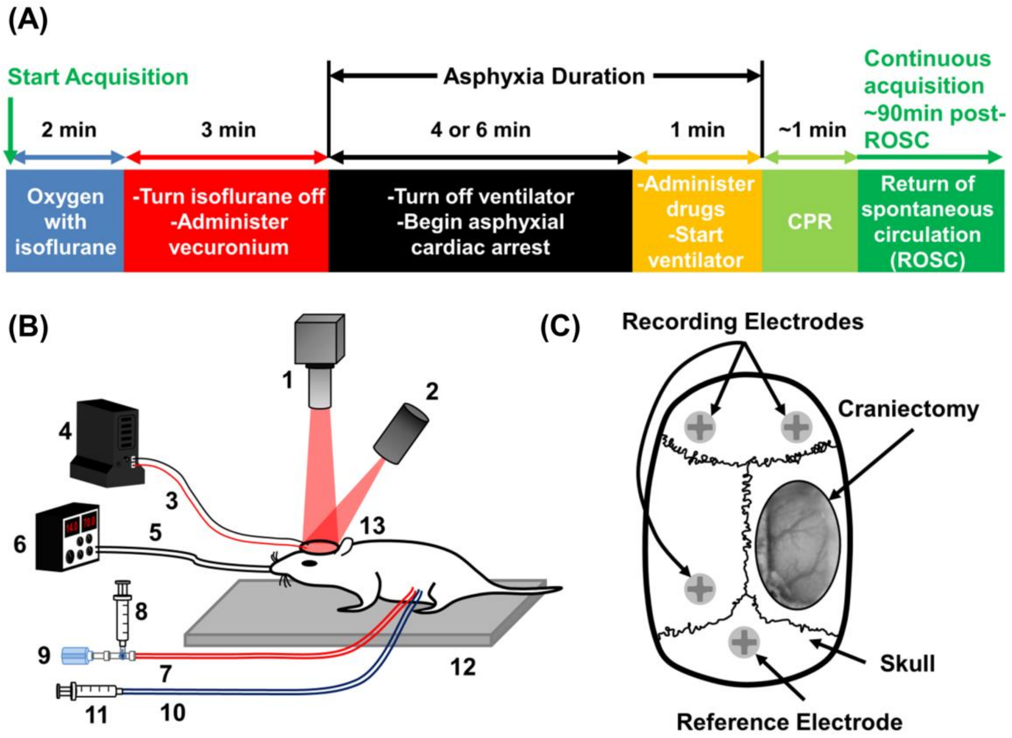

Figure 3.2: Cardiac arrest (CA) experimental design and setup. (A) Diagram of CA timeline. Experiment began (t = 0) with an isoflurane/oxygen mix. At t = 2min, isoflurane was turned off, Vecuronium administered, and animal exposed to room air. The ventilator was then turned off to initiate the asphyxial CA period that lasted 5- or 7-min. Approximately 1min prior to initiation of cardiopulmonary resuscitation (CPR), epinephrine, sodium bicarbonate and saline were administered and the ventilator restarted. CPR was then performed for ~1min until ROSC, after which data acquisition continued for ~90min post-ROSC. (B) Schematic of multi-instrument design to perform laser speckle imaging (LSI), arterial blood pressure measurements, and electroencephalography (EEG). (1) LSI camera with laser line filter and adjustable camera lens; (2) 809nm light source for LSI to display speckle pattern on rat cortex; (3) EEG wire that connected EEG screw electrodes to EEG preamplifier; (4) EEG preamplifier with 0.35Hz high pass filter; (5) intubation tubing connected to ventilator; (6) ventilator with adjustable settings; (7) femoral artery catheter; (8) syringe to administer fluids for dehydration and remove blood for arterial blood gas (ABG) measurements; (9) blood pressure transducer; (10) femoral vein catheter; (11) syringe to administer epinephrine, sodium bicarbonate and saline prior to CPR and ROSC; (12) stereotaxic frame with rat mounted; (13) brain illuminated by laser light with EEG screw electrodes. (C) Magnified view of animal head that shows location of EEG electrodes and craniectomy.

3.3.4 Initial Data Processing

LSI processing used custom-written MATLAB code to process each raw speckle image and obtain CBF data. A sliding 5 x 5 square sliding window was used to convert each raw speckle image to a corresponding speckle contrast (K) image using the equation $K = \sigma/\langle I\rangle$, where σ is the standard deviation of the intensity and $\langle I\rangle$ is the average intensity within each window. Each speckle contrast image was then converted to a cerebral blood flow (CBF) map using a simplified speckle imaging equation CBF = $1/2TK^2$, where K is the speckle contrast and T is the exposure time of the camera in seconds[90,46]. A representative region of interest (ROI) was then selected within the craniectomy to obtain an average SFI value and create time-resolved CBF curves. We then calculated relative CBF (rCBF) curves (Eq. 3.1), and applied a sliding median filter of 10s in length.

$$rCBF = 100 \times \frac{SFI(t)}{baseline\ SFI} \qquad \text{(Eq. 3.1)}$$

Baseline was defined as the mean SFI value the minute prior to asphyxia (to minimize isoflurane effects) and thus the rCBF at baseline was 100. One minute prior to asphyxia was chosen as baseline due to post-anesthesia emergence and consequent cerebral hyperemia[47,48]. The median-filtered relative CBF curves were used for further analyses. To create CBF images with increased signal to noise, each individual CBF map taken over a one-second interval was averaged. These CBF images were used for further spatiotemporal analysis.

Raw EEG data were filtered using custom written MATLAB (Mathworks Inc., Natick, MA) code. Data were detrended and common average referencing was performed using each electrode[49]. A finite impulse response (FIR) notch filter at 60Hz was used, followed by a FIR bandpass filter from 1 to 150Hz. Signals were then downsampled to 600Hz to reduce memory and computational time.

To detect the initial EEG burst, we developed an automated algorithm using custom-written MATLAB code. Peaks above 20μV were detected the minute prior to asphyxia and the mean peak value was calculated. Following resuscitation, when the EEG amplitude exceeded 50% of the mean peak value from baseline in the frontal electrodes, a burst was detected. To identify the presence of the initial EEG burst and minimize the effect of noise artifacts, we applied a selection criterion that bursting for five consecutive minutes was necessary. Once bursting occurred for this period, the algorithm reported the initial EEG burst time relative to ROSC, which was used in subsequent analysis. We compared the spreading oligemia wave in the last post-ROSC period to the timing of the initial EEG burst.

3.3.5 Spatiotemporal Analysis of CBF Maps

To determine if spatial changes in CBF occurred during ACA and resuscitation, videos of the second-averaged CBF images were made. The videos were used to characterize the periods of spreading CBF waves. The spatial onset and completion locations of each wave and their corresponding times were extracted after visual inspection of each video. To calculate the speed of the wave, the distance between the onset and completion locations and the duration of the waves were used. The rCBF values from the rCBF time-course curves at the onset and completion times were extracted. To assess directionality of the spreading waves, each wave was assigned one of six directions: 1) medial, 2) anterior, medial, 3) posterior, medial, 4) lateral, 5) anterior, lateral, or 6) posterior, lateral. To examine if there was a relationship between rCBF at the onset and the direction of wave propagation the directions were compared to the rCBF value at the onset of each spreading wave. To quantify the total amount of brain perfusion prior to the onset of spreading ischemia, we integrated over time the rCBF time-course signal from the onset of asphyxia to the onset of spreading ischemia.

3.3.6 Vessel Diameter

Custom-written MATLAB code was used to compute vessel diameter using the second-averaged CBF images. First, the user defined the centerline for a given vessel of interest. Next, the user defined the bounds for a line that was perpendicular to the centerline. For each time point, the CBF values from the perpendicular line were extracted, and a Gaussian was fitted through the CBF values. If the R-squared of the Gaussian fit was greater than 0.9, the full-width half-maximum (FWHM) was computed from the Gaussian fit, if the value was less than 0.9, the diameter was assigned a not-a-number value. This process is repeated for as many vessels as desired. A flow chart is shown in Figure 3.3.

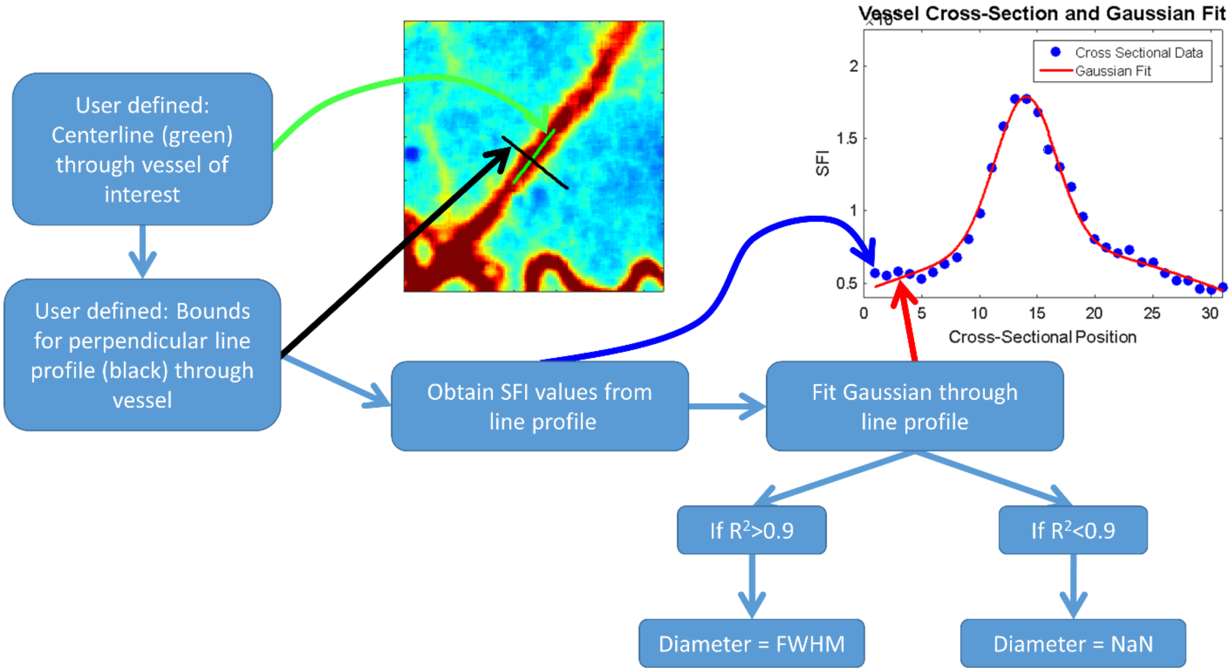

Figure 3.3: Method to compute vessel diameter from SFI maps. User defines the centerline for a given vessel of interest. Then, the user defines the bounds for a line that is perpendicular to the centerline. The CBF values from the perpendicular line are extracted, and a Gaussian is fit to the CBF values. If the R-squared of the Gaussian fit was greater than 0.9, the full-width half-maximum (FWHM) is computed from the Gaussian fit, if the value was less than 0.9, the diameter is assigned a not-a-number value.

3.3.7 EEG IQ

To obtain a measurement of short-term neurological outcome, we used a quantitative EEG method called information quantity (IQ). The following steps were performed to obtain EEG IQ as a function of time. Using a temporal sliding window of 10s with 20% overlap, a 5-level discrete wavelet transform (DWT) was applied to the filtered EEG data to extract DWT coefficients. From the baseline EEG immediately one minute prior to onset of asphyxia, 20 fixed microstates were obtained that encompassed the mean ±3 standard deviations of the DWT coefficients. A histogram of the continuous EEG recording was created using the DWT coefficients with the 20 microstates. The probability distribution function was calculated, from the histogram, and the Shannon entropy was calculated using the equation: $SE = -\sum_{m=1}^{M} pdf(m)\log_2(pdf(m))$. SE is the Shannon entropy, M is the number of microstates, and pdf is the probability distribution function from the histogram. We used this equation within each window to calculate EEG IQ as a function of time. The EEG IQ was then normalized to the baseline EEG IQ, which is defined as the mean EEG IQ calculated over a one-minute interval immediately prior to onset of asphyxia. An EEG IQ of 0 indicates no brain electrical activity, while an EEG IQ of 1 indicates normal brain electrical activity.

3.4 Results

During ACA, a wave of decreasing CBF was visualized in each experiment. Figure 3.4A shows a representative experiment of a spreading ischemia wave. A decrease in CBF propagates from the anterior, lateral region of the craniectomy towards the posterior, medial region of the craniectomy (Figure 3.4A). After combining the ACA durations, the onset and completion times of the spreading ischemia wave are 2.21 ± 0.29min and 3.21 ± 0.27min after the onset of asphyxia, respectively (Figure 3.4C). The speed of the spreading ischemia wave is 4.76 ± 1.10mm/min. A representative example of the rCBF time course with the spreading ischemia window labeled is shown in Figure 3.4B. From the onset to the completion of the spreading ischemia wave, the rCBF decreases from $20.80 \pm 11.85\%$ to $4.19 \pm 1.80\%$ (Figure 3.4D).

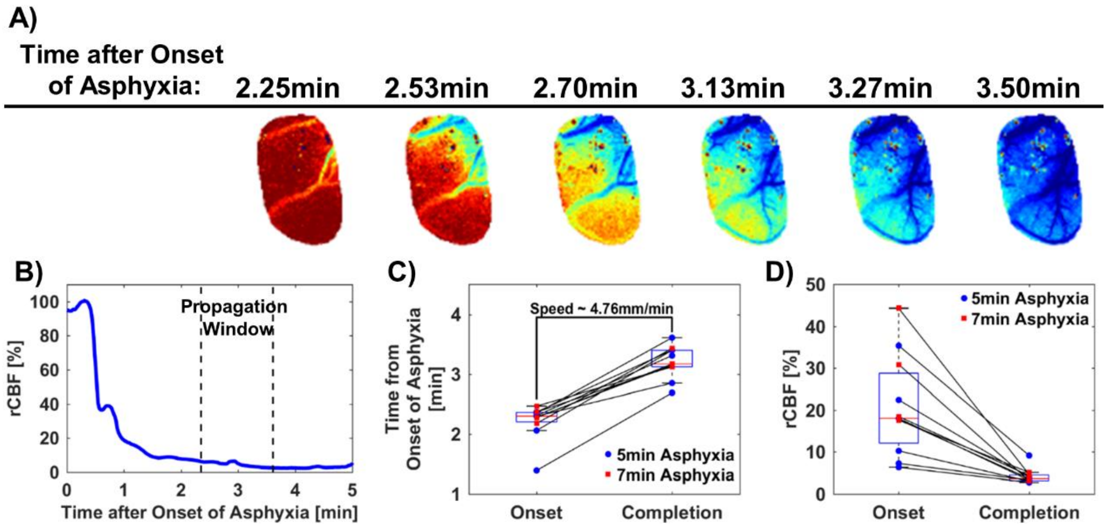

Figure 3.4: Characterization of spreading ischemia wave during CA. (A) A representative 5-min ACA experiment that shows a spreading ischemia (decrease in rCBF) wave propagate from the upper-right to the lower-left regions of the craniectomy. The time above each image is the time after the onset of asphyxia. (B) A representative rCBF time course with the window of spatial propagation labeled with dashed lines. (C) Characterization of the onset and completion times of the spreading ischemia wave (n=11). The average speed of the wave is 4.76mm/min. The 5-and 7-min asphyxial durations are represented by blue circles and red squares, respectively. (D) Characterization of the onset and completion rCBF values from the rCBF time course at the onset and completion of the spreading ischemia wave (n= 11). The 5-and 7-min asphyxial durations are represented by blue circles and red squares, respectively.

During the time period of spreading ischemia, vasoconstriction occurs. Figure 3.5A shows representative images of a single vessel being analyzed over time, with a line-scan through the vessel of interest. Figure 3.5B shows the percent change in vessel diameter for 9 vessels averaged from a single rat as a function of time during the asphyxial period. At ~2.45min after the onset of asphyxia, vasoconstriction is visualized, which coincides with the onset of spreading ischemia. The completion of the spreading ischemia wave occurs after the vessel diameter has decreased by ~15%.

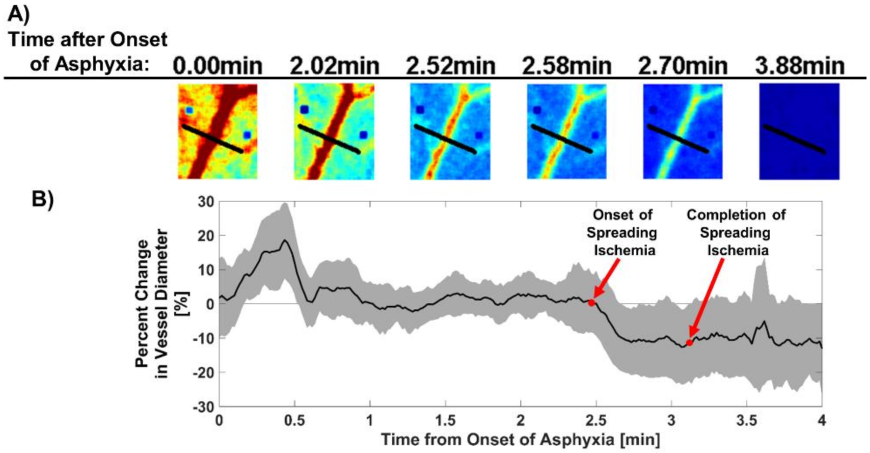

Figure 3.5: Spreading ischemia during CA coincides with vasoconstriction. (A) A representative 7-min ACA experiment that shows images of a single vessel being analyzed over time with a line-scan (black line) through the current vessel of interest. The time above each image is the time after the onset of asphyxia. (B) The same representative experiment as in (A) that shows the percent change in vessel diameter for 9 vessels averaged as a function of time during the asphyxial period. The onset and completion of the spreading ischemia wave are labeled with a red circle. The black solid line is the mean over the 9 vessels, and the gray is the standard deviation error bars.

More total CBF perfusion prior to the onset of spreading ischemia is associated with worse EEG signal recovery. Figure 3.6A shows that the 5- and 7-min ACA experiments exhibit a near-linear trend for each respective group. One data point in each group does not follow this trend and are labeled with orange arrows. Figure 3.6B shows two representative rCBF time courses from 7-min ACA experiments with good (green) and poor (black) neurological recovery.

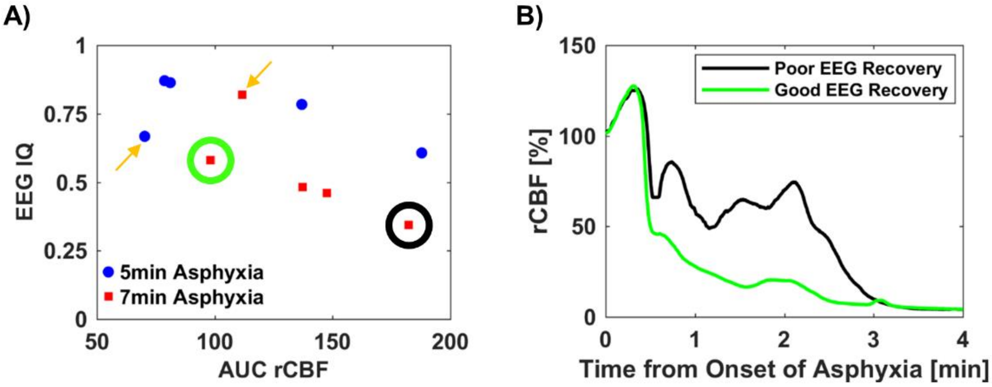

Figure 3.6: More total perfusion prior to onset of spreading ischemia is associated with worse EEG signal recovery. (A) 5- (n=5) and 7-min (n=5) ACA experiments that shows a near-linear trend for each

respective group. One data point in each group (5- or 7-min ACA) goes against the linear trend, highlighted with orange arrows. (B) Two representative 7min ACA rCBF time courses with good (green) and poor (black) neurological recovery. The green and black circles in (A) are the same green and black time courses in (B).

After resuscitation, a wave of increasing CBF was visualized in each experiment. Figure 3.7A shows a representative experiment of a spreading hyperemia wave. An increase in CBF propagates the anterior region of the craniectomy and has a circular-type pattern towards the posterior region of the craniectomy. The onset and completion times of the waves are 2.97±0.84min and 4.36±1.12min post-ROSC (Figure 3.4C). The speed of the propagating wave is 3.54±0.76mm/min. A representative example of an rCBF time course with the onset and completion marked with black-dashed vertical lines is shown in Figure 3.4B. rCBF increases from 83.91±33.53% at the onset to 134.91±33.50% at the completion of the spreading hyperemia wave (Figure 3.4D). The rCBF increases during the spreading hyperemia period by 51.00±18.91%.

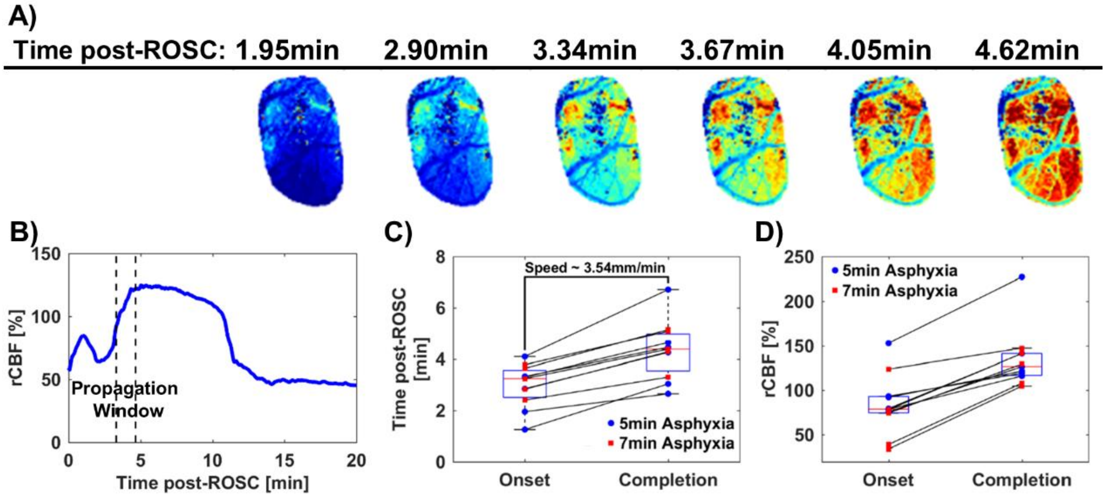

Figure 3.7: Characterization of spreading hyperemia wave during immediate post-ROSC phase. (A) A representative 5-min ACA experiment that shows a spreading hyperemia (increase in rCBF) wave propagate in a circular pattern from the top to the bottom region of the craniectomy. The time above each image is the time post-ROSC. (B) A representative rCBF time course with the window of spatial propagation labeled with black dashed vertical-lines. (C) Characterization of the onset and completion times of the spreading hyperemia wave (n=11). The average speed of the wave is 3.54mm/min. The 5-and 7-min asphyxial durations are represented by blue circles and red squares, respectively. (D) Characterization of the onset and completion rCBF values from the rCBF time course at the onset and completion of the spreading hyperemia

wave (n= 11). The 5-and 7-min asphyxial durations are represented by blue circles and red squares, respectively.

After the hyperemia period, but before the stabilized hypoperfusion period, a wave of decreasing CBF was visualized in 9 out of 11 experiments. Both cases were due to bleeding over the imaging area. Figure 3.8A shows a representative experiment of a spreading oligemia wave. A decrease in CBF propagates from the medial to the lateral region of the craniectomy. The onset, burst, and completion times are 11.14±2.62 min, 13.89±2.41min, and 15.08±3.08min post-ROSC, respectively (Figure 3.8C). The onset of the spreading oligemia wave always precedes the initial EEG burst. A representative example of an rCBF time course is shown in Figure 3.8B. rCBF decreases from 137.01±23.80% at the onset to 79.51±25.75% at the burst to 57.67±8.63% at the completion of the spreading oligemia wave (Figure 3.8D). From the onset to the completion of the spreading oligemia wave, a large drop in the rCBF occurs (79.34±25.11%).

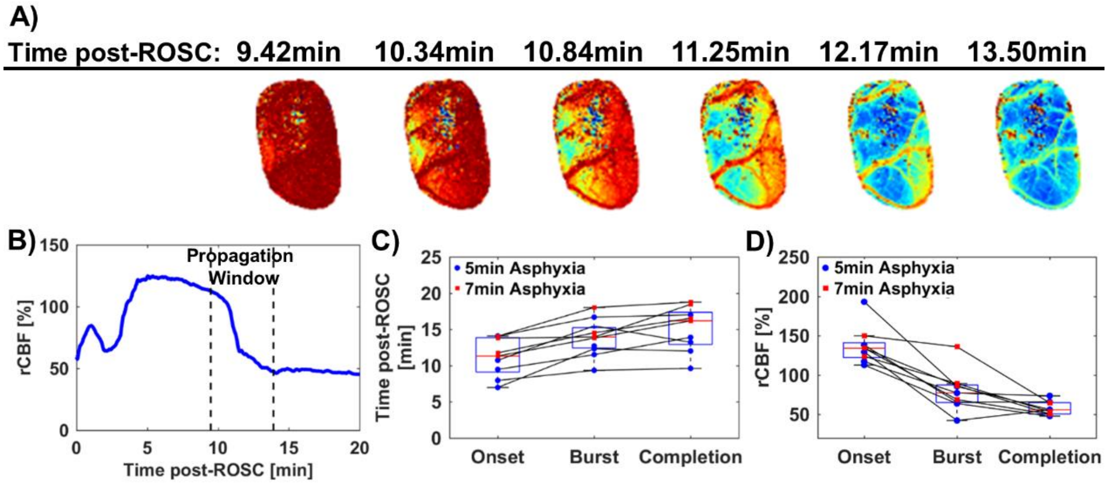

Figure 3.8: Characterization of spreading oligemia wave from hyperemia to stabilized hypoperfusion post-ROSC. (A) A representative 5-min ACA experiment that shows a spreading oligemia (decrease in rCBF) wave propagate from left to right within the craniectomy. The time above each image is the time post-ROSC. (B) A representative rCBF time course with the window of spatial propagation labeled with dotted lines. (C) Characterization of the onset, burst, and completion times of the spreading oligemia wave (n=9). The 5- and 7-min asphyxial durations are represented by blue circles and red squares, respectively. (D) Characterization of the onset, burst, and completion rCBF values from the rCBF time course at the onset, burst, and completion

of the spreading oligemia wave (n= 9). The 5-and 7-min asphyxial durations are represented by blue circles and red squares, respectively.

We found that the spreading ischemia and spreading oligemia waves propagate in opposite directions. The decrease in rCBF associated with the spreading ischemia waves all propagated towards the medial region of the brain with some anterior or posterior directionality (Figure 3.9C). However, the decrease in rCBF associated with the spreading oligemia waves all propagated towards the lateral region of the brain with some anterior or posterior directionality (Figure 3.9D). We also calculated the rCBF value at the onset of the spreading waves with respect to their directionality. We found that during both the spreading ischemia and oligemia waves, a higher rCBF at the onset of the wave was associated with an anterior, medial directionality (wave began in posterior, lateral region) [Figure 3.9E, F].

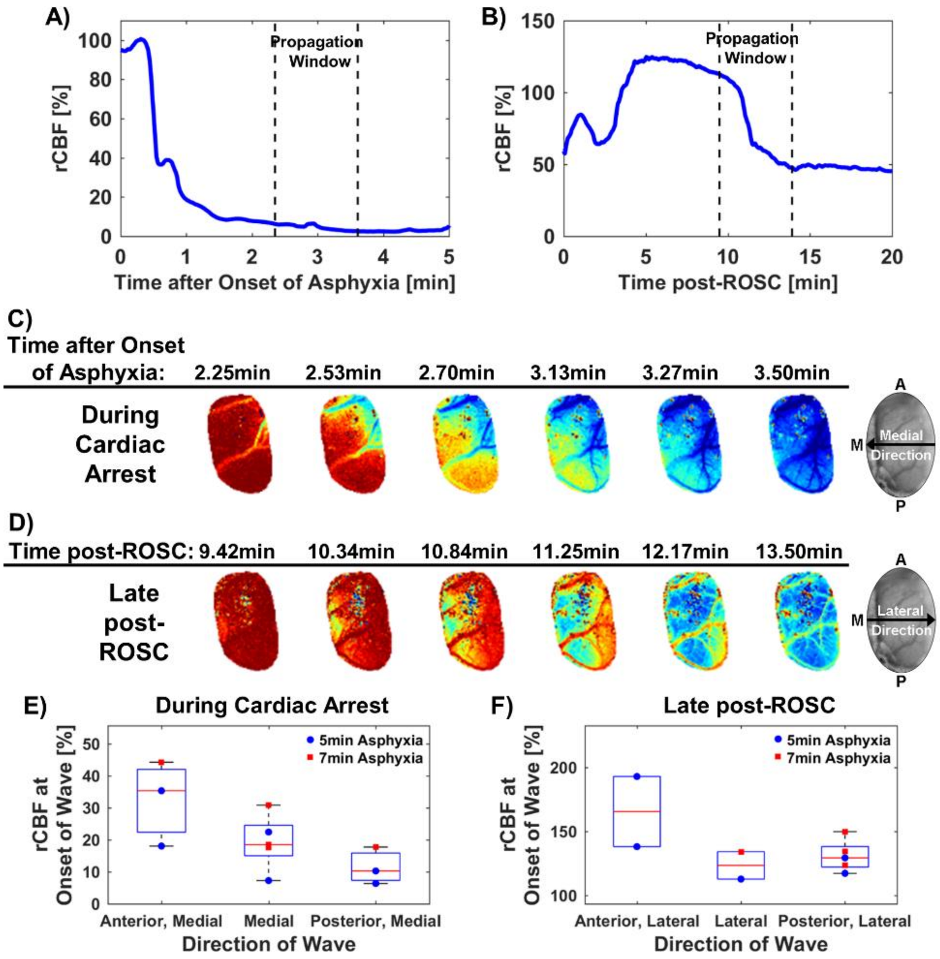

Figure 3.9: Spreading ischemia and spreading oligemia waves propagate in opposite directions. (A) A representative rCBF time course during asphyxia with the window of spreading ischemia with the spatial propagation labeled with dashed lines. (B) A representative rCBF time course post-ROSC with the window of spreading oligemia with the spatial propagation labeled with dashed lines. (C) A representative 5-min ACA experiment that shows a spreading ischemia wave propagate from the upper-right to the lower-left regions of the craniectomy. The time above each image is the time after the onset of asphyxia. The image on the right shows that all spreading ischemia waves propagate towards the medial region of the brain. (D) A representative 5-min ACA experiment that shows a spreading oligemia wave propagate from left to right within the craniectomy. The time above each image is the time post-ROSC. The image on the right shows that all spreading oligemia waves propagate towards the lateral region of the brain. (E) rCBF at the onset of spreading ischemia wave associated to directionality (n=11). (F) rCBF at the onset of spreading oligemia wave associated to directionality (n=9).

We found that the spreading hyperemia and spreading oligemia waves resembled CSD-like features. Figure 3.10A shows a rCBF time course post-ROSC. The spreading hyperemia and spreading oligemia periods are labeled with two sets of vertical-dashed lines. A hyperemia period is seen from ~3.5min to 11min post-ROSC. The spreading hyperemia and oligemia waves are shown in Figure 3.10B top and bottom, respectively. Upon comparison of a traditional CSD that was induced through KCl being applied to the brain (Figure 3.10D), there are visual similarities. First, the rCBF time courses following resuscitation from CA (Figure 3.10A) and following KCl application (Figure 3.10C) both have hyperemic periods that are followed by periods of stabilized rCBF. Furthermore, the images from the KCl experiment have a spatial increase in rCBF from right to left that is followed by a decrease in rCBF. Although the increase and decrease in rCBF are in non-similar directions during the two propagation windows post-ROSC, there is still an increase and decrease phase of rCBF that is similar to the KCl-induced spreading CBF wave.

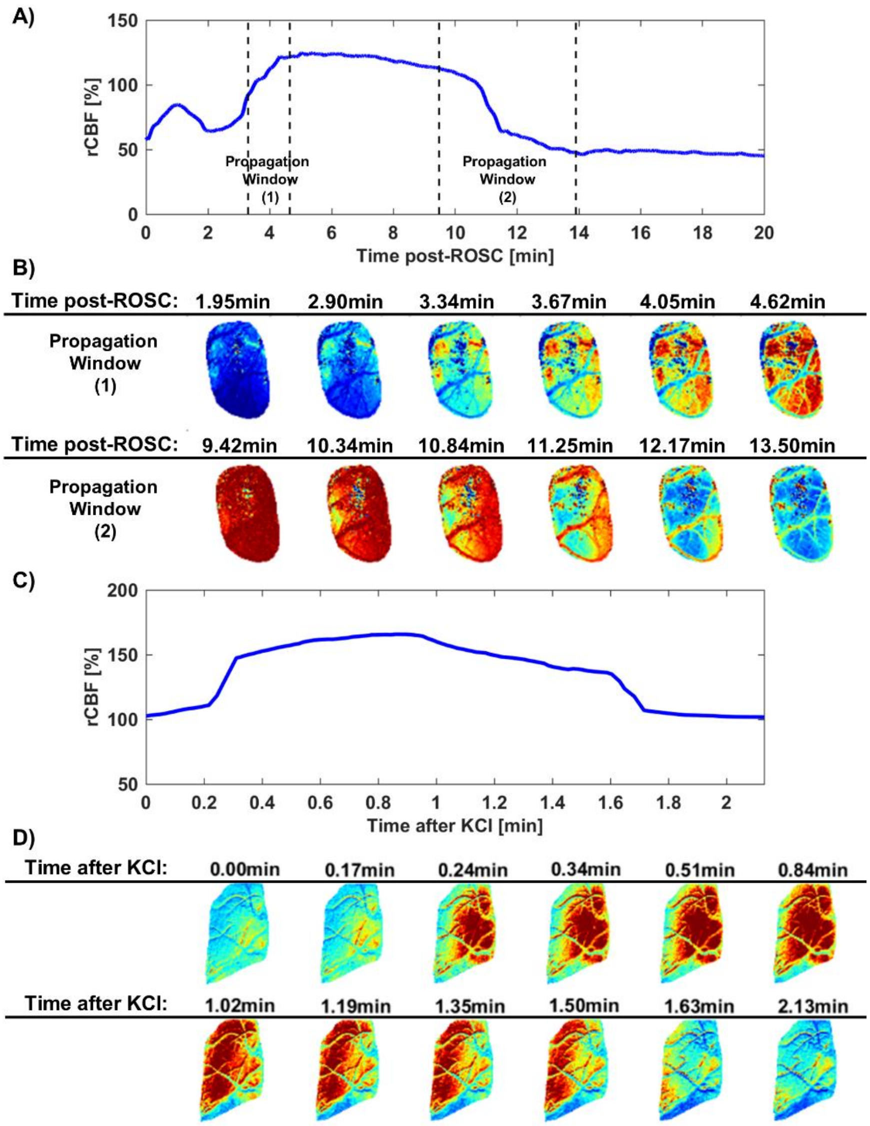

Figure 3.10: Spreading hyperemia and spreading oligemia waves resemble cortical spreading depression (CSD)-like features. (A) A representative rCBF time course post-ROSC with the windows of spreading hyperemia (1) and spreading oligemia (2) labeled with vertically-dashed lines. (B) A representative 5-min ACA experiment that shows a spreading hyperemia wave (top) and spreading oligemia wave (bottom). The time above each image is the time post-ROSC. (C) A representative rCBF time course associated with KCl-induced CSD (D) A representative KCl experiment that shows a spreading wave propagate from right to left within the craniectomy. The time above each image is the time after KCl administration.

3.5 Discussion

Spreading depolarizations (SDs) are complex phenomena related to many clinically important applications[91]. Global cerebral ischemia studies have shown that a breakdown of ion membranes leads to a spreading wave of depolarization that propagates at a rate of 2-

6mm/min[77]. However, the results presented here show for the first time that there are also spatial CBF changes in the form of a spreading ischemia wave that propagates during a similar time-point as the traditional SD wave (Figure 3.4A). The spreading ischemia wave presented here propagates at a rate of 4.76±1.10mm/min (Figure 3.4C), which is similar to previous spreading depolarization studies.

At the same time the spreading ischemia wave is visualized, vasoconstriction also occurs in the cerebral cortex vessels. Shin et al, performed a middle cerebral artery occlusion (MCAO) in the rat cortex, and visualized anoxic depolarization that was accompanied with a spreading decrease in CBF and vasoconstriction[80]. These results highlight the striking similarities between our global ischemic event through CA and a focal ischemic event through MCAO. Spreading ischemia during CA was an unexpected finding. However, spreading ischemia during CA and focal-ischemic stroke may be driven by similar underlying membrane potential changes. However, spreading ischemia may be the last event that precedes anoxic depolarization and the breakdown of membrane potentials. Future studies will need to directly relate these timings to determine the causal relationship between the two phenomena.

Preliminary data by Dr. Akbari's lab shows that the earlier the onset of SD during CA is associated with better neurological outcome 24h after resuscitation (Figure 3.1). Although the association is strong, it is unclear what the underlying mechanism is between earlier onset of SD and better neurological outcome. The data presented here suggests that total CBF prior to onset of spreading ischemia may be a potential mechanism. Our data shows that more total CBF perfusion prior to the onset of spreading ischemia is associated with worse neurological outcome (Figure 3.6). A couple hypothesis that may explain why more total perfusion prior to onset of spreading ischemia results in poor neurological outcome are presented here. The first hypothesis is associated with the fact that electrocerebral silence begins ~30s after the onset of asphyxia. After electrocerebral silence begins, the brain is utilizing little to no oxygen, while still receiving CBF. We hypothesize that increased total CBF perfusion during electrocerebral silence may result in increased free radical production[92]. The second hypothesis is associated with the fact that an earlier onset of SD may result in a larger amount of energy stores, due to less used prior to onset of SD. We hypothesize that after resuscitation, the increased energy stores may be better utilized to regain neurological function and result in better neurological outcome. Further testing of these hypotheses are needed to determine the mechanisms associated with this interesting phenomena Dr. Akbari's lab has encountered and our CBF data supports. This hyperdynamic period associated with death may potentially be modifiable through the use of therapeutics to alter neurological recovery.

The data presented here demonstrates that during CA, a spreading ischemia wave propagates from the lateral region of the brain to the medial region of the brain (Figure 3.9C). Farkas et al[79] showed that anoxic depolarization, induced through cardiac administration of KCl and subsequent CA, resulted in a propagating wave of electrical activity changes from the frontal lateral corner to the dorsal medial corner of the craniotomy[79]. These results suggest that the spreading ischemia and anoxic depolarization may be similar phenomena and even linked to one another. However, Farkas et al, also used LSI to examine CBF changes, state that "…there was no longer any detectable change in CBV (i.e., MAP, CBF, and arteriolar diameter had settled to "death" values)…". The data presented here contests this statement, as we visualize clear spatiotemporal changes in

CBF (Figure 3.4) and vessel diameter (Figure 3.5B) during the period of anoxic depolarization. Furthermore, Jarvis et al showed that when brain sections are deprived of O_2 and glucose, a propagating wave of depolarization originates in the lateral region of the brain section and finishes in the medial region of the brain section, which is in agreement with the directionality results of the spreading ischemia wave.

Interestingly, we visualized a second wave of decreasing CBF that occurred between hyperemia and stabilized hypoperfusion post-ROSC. The directionality of these waves was in the opposite direction of the spreading ischemia wave during CA. All the spreading oligemia waves propagated towards the lateral region of the brain (Figure 3.9D). Due to many previous studies lacking the capabilities to analyze post-ROSC changes, this is the first demonstration of a spatial CBF wave propagating during this time period after resuscitation. One potential hypothesis for the directionality associated with the spreading ischemia wave is based on the following. The anterior and middle cerebral arteries supply the medial and lateral regions of the brain with blood, respectively. The anterior cerebral artery is able to alter its diameter more than the middle cerebral artery. We hypothesize that a decrease in blood pressure (e.g., during CA) leads to an increased dilation of the anterior cerebral artery compared to the middle cerebral artery, which would cause the CBF delivered to the medial region remain elevated and decrease later compared to the lateral region of the brain. After CA there is cerebrovascular impairment, which leads to reduced vascular tone of cerebral vessels. We hypothesize that increased cerebrovascular impairment alters the ability of the anterior cerebral artery to change its vessel diameter and make adjustments to CBF after resuscitation, which causes the spreading wave to propagate in the opposite direction. Although these hypotheses are unfounded, new technologies may be needed to determine its association and potential clinical implications.

Cortical spreading depressions (CSDs) are seen in traumatic brain injury, focal ischemic stroke, and migraines. CSDs are characterized by a negative deflection of DC potential with a subsequent wave of increased CBF or hyperemia. The return of the DC potential coincides with the peak hyperemic response from the CSD[93]. Next, a wave of decreasing CBF occurs and remains in this decreased CBF or oligemic state for a period of time[94].. Our data suggests that in the acute period following resuscitation from CA that a CSD may occur (Figure 3.10). Within 5min after resuscitation, a spreading hyperemia wave occurs, which is followed by a spreading oligemia wave. However, the spreading hyperemia and oligemia waves propagate in dissimilar directions following resuscitation. In a traditional CSD, the spreading hyperemia and following decrease in CBF are in the same direction. Furthermore, CSDs induce the depressed EEG signal for 5 to 15min[91]. Following CA, a period of EEG silence is observed[36]. The resumption of brain electrical activity (initial EEG burst) occurs after the onset of the spreading oligemia wave, which may suggest this event is triggering the restarting of brain electrical activity.

3.6 Conclusions

SDs have been fairly characterized, and a large number of recent studies involving SDs highlight their importance. Based on previous studies and Dr. Akbari's preliminary data, we decided to conduct an exploratory study of spatiotemporal CBF changes that occur during hyperdynamic periods associated with CA and resuscitation. We focused on three main time-periods based on our previous data: (1) during CA when typical SDs occur, (2) immediately after resuscitation prior to the hyperemic peak, and (3) from the hyperemic peak to the stabilized hypoperfusion period. We visualized spreading CBF waves during each phase. Spreading wave (1) was associated with a spatial decrease in CBF that resembled a "spreading ischemia" wave seen in stroke literature[88,94]. Furthermore, we found that an increase in total CBF prior to the onset of spreading wave (1) was associated with worse neurological outcome. Spreading wave (2) was associated with a spatial increase in CBF the resembled a "spreading hyperemia" wave. Spreading wave (3) was associated with a spatial decrease in CBF that resembled the "spreading ischemia" wave, and we called the "spreading oligemia" wave since the CBF remained at a higher level[87]. We also found that waves (1) and (3) propagated in opposite directions and waves (2) and (3) resembled a well-known phenomenon called cortical spreading depression (CSD). Due to the novel preclinical CA and resuscitation model, these results show that there are complex spatiotemporal changes in CBF that occur before, during, and after CA and resuscitation, and modifying the timing of these spatial CBF changes may affect neurological outcome.

3.7 Acknowledgements

This work was supported by the Arnold and Mabel Beckman Foundation, the United States National Institutes of Health (P41EB015890), the National Science Foundation Graduate Research Fellowship Program (DGE-1321846, to C.C.), the National Center for Research Resources and National Center for Advancing Translational Sciences, National Institutes of Health, through the following grants: TL1TR001415-01 to R. H.W., R21 EB024793 to Y. A., and 5KL2TR000147 to Y.A. via UL1 TR001414. The content is solely the responsibility of the authors and does not necessarily represent the official views of the NIH.

CHAPTER 4: Summary and Conclusions

Annually, over 550,000 people in the United States suffer cardiac arrest (CA) while initial survival rates remain poor (10-30%)[1]. Approximately 85 to 90% of survivors have impaired cognitive function, which leads to decreased quality of life for survivors, increased burden on caregivers, and direct costs of over $6 billion/year[1,2]. CA causes inadequate cerebral blood flow (CBF), which results in a cascade of events that lead to neuronal cell death within three minutes[5,3,4]. Reperfusion after resuscitation from CA leads to further neuronal damage, due to reactive oxygen species and potential decoupling between CBF and metabolism[6]. Due to a lack in technologies that monitor hyperdynamic physiological changes in response to CA and resuscitation, we developed a multi-modal platform with high spatial and temporal resolution to monitor CBF, arterial blood pressure and brain electrophysiology. Using this platform, we used an asphyxial CA (ACA) translational preclinical model aimed to better understand how the brain recovers following CA and ultimately to improve neurological outcome.

We first examined temporal changes associated with CBF and the resumption of brain electrical activity after resuscitation from CA. Our results quantified the time and magnitude of the hyperemic peak and stabilized hypoperfusion post-ROSC. Furthermore, we showed that CBF and MAP are well correlated before stabilized hypoperfusion, but CBF is at a large deficit after stabilized hypoperfusion, despite normal MAP. Finally, we demonstrated that EEG bursting begins after the CBF hyperemic phase and before stabilized hypoperfusion. We demonstrated that we can predict when the initial EEG burst occurs for less severe CA well using a fixed predictive model, but using a robust predictive model is able to predict the initial EEG burst for both severities of CA. The link between hemodynamics and the resumption of brain electrical activity, suggests that clinicians may be able to utilize and develop hemodynamic-altering therapeutics that modify the beginning of neurological recovery.

Next, we examined temporal CBF and ABP pulsatility changes following resuscitation from CA. We demonstrated several key associations between acute CBF and ABP pulsatility changes immediately after resuscitation from ACA and their relationship to rCVR and short-term neurological outcome. Our study revealed that CBF pulsatility is altered significantly from baseline within 2h after resuscitation, but ABP pulsatility changes little. Furthermore, our results demonstrate that rCVR is related to changes in CBF pulsatility, but not ABP pulsatility. We also demonstrate that CBF pulsatility does not influence short-term neurological outcome, but increased ABP pulsatility is associated with worse short-term neurological outcome. Collectively, our findings indicate the importance of investigating acute CBF and ABP pulsatility immediately following resuscitation from CA. However, future studies that modify and monitor CBF and ABP pulsatility are required to assess their effects on neurological outcome.

Last, we focused on spatiotemporal changes during hyperdynamic periods of CA and resuscitation. We focused on spatiotemporal CBF changes during three hyperdynamic periods: (1) entering CA, (2) within 5min after resuscitation, and (3) from hyperemia to hypoperfusion (i.e., 5 to 20min after resuscitation). We visualized spreading CBF waves during each phase. Spreading wave (1) was associated with a spatial decrease in CBF that resembled a "spreading ischemia" wave seen in stroke literature[86,88]. Furthermore, we found that an increase in total CBF prior to the onset of spreading wave (1) was associated with worse neurological outcome. Spreading wave (2) was associated with a spatial increase in CBF the resembled a “spreading hyperemia” wave. Spreading wave (3) was associated with a spatial decrease in CBF that resembled the “spreading ischemia” wave, and we called the “spreading oligemia” wave since the CBF remained at a higher level. We also found that waves (1) and (3) propagated in opposite directions and waves (2) and (3) resembled a well-known phenomenon called cortical spreading depression (CSD). These spatiotemporal characteristics are complex, yet may have clinical importance to neurological outcome.

Collectively, these findings highlight the complex nature of the hyperdynamic cerebral response to CA and resuscitation. The multi-modal platform revealed previously unknown phenomena. Each finding presented here may lead to the development of novel therapeutic approaches to modulate hemodynamics during periods of CA and resuscitation. These modifications may ultimately lead to improvement of neurological outcome for CA survivors.

REFERENCES

1. Benjamin, E. J. *et al. Heart Disease and Stroke Statistics—2018 Update: A Report From the American Heart Association*. *Circulation* (2018).
2. Lick, C. J. *et al.* Take Heart America: A comprehensive, community-wide, systems-based approach to the treatment of cardiac arrest. *Crit. Care Med.* **39,** 26–33 (2011).
3. Jeffrey L. Saver. Time Is Brain—Quantified. *Stroke* **37,** 263–6 (2006).
4. Zivin, J. A. Factors determining the therapeutic window for stroke. *Neurology* **50,** 599–603 (1998).
5. Madl, C. & Holzer, M. Brain function after resuscitation from cardiac arrest. *Curr. Opin. Crit. Care* **10,** 213–217 (2004).
6. Lipton, P. Ischemic cell death in brain neurons. *Physiol. Rev.* **79,** 1431–1568 (1999).
7. Westhall, E. *et al.* Electroencephalography (EEG) for neurological prognostication after cardiac arrest and targeted temperature management; rationale and study design. *BMC Neurol.* **14,** 159 (2014).
8. Jia, X., Koenig, M. A., Venkatraman, A., Thakor, N. V. & Geocadin, R. G. Post-cardiac arrest temperature manipulation alters early EEG bursting in rats. *Resuscitation* **78,** 367–373 (2008).
9. Jia, X. *et al.* Improving neurological outcomes post-cardiac arrest in a rat model: Immediate hypothermia and quantitative EEG monitoring. *Resuscitation* **76,** 431–442 (2008).
10. Temple, A. & Porter, R. Predicting neurological outcome after cardiac arrest. *Contin. Educ. Anaesthesia, Crit. Care Pain* (2012).
11. Cloostermans, M. C., van Meulen, F. B., Eertman, C. J., Hom, H. W. & van Putten, M. J. a

M. Continuous electroencephalography monitoring for early prediction of neurological outcome in postanoxic patients after cardiac arrest: a prospective cohort study. *Crit. Care Med.* **40,** 2867–75 (2012).

12. Geocadin, R. G. *et al.* Neurological recovery by EEG bursting after resuscitation from cardiac arrest in rats. *Resuscitation* **55,** 193–200 (2002).
13. Taccone, F. *et al.* How to assess prognosis after cardiac arrest and therapeutic hypothermia. *Crit. Care* **18,** 202 (2014).
14. Wennervirta, J. E. *et al.* Hypothermia-treated cardiac arrest patients with good neurological outcome differ early in quantitative variables of EEG suppression and epileptiform activity. *Crit. Care Med.* **37,** 2427–2435 (2009).
15. Hickey, R. W. *et al.* Induced hyperthermia exacerbates neurologic neuronal histologic damage after asphyxial cardiac arrest in rats. *Crit. Care Med.* **31,** 531–5 (2003).
16. Lee, J. K. *et al.* Cerebral blood flow and cerebrovascular autoregulation in a swine model of pediatric cardiac arrest and hypothermia. *Crit. Care Med.* **39,** 2337–2345 (2011).
17. Sundgreen, C. *et al.* Autoregulation of cerebral blood flow in patients resuscitated from cardiac arrest. *Stroke.* **32,** 128–132 (2001).
18. Bisschops, L. L. a, Hoedemaekers, C. W. E., Simons, K. S. & van der Hoeven, J. G. Preserved metabolic coupling and cerebrovascular reactivity during mild hypothermia after cardiac arrest. *Crit. Care Med.* **38,** 1542–1547 (2010).
19. Mörtberg, E., Cumming, P., Wiklund, L., Wall, A. & Rubertsson, S. A PET study of regional cerebral blood flow after experimental cardiopulmonary resuscitation. *Resuscitation* **75,** 98–104 (2007).

20. Edgren, E. *et al.* Cerebral blood flow and metabolism after cardiopulmonary resuscitation. A pathophysiologic and prognostic positron emission tomography pilot study. *Resuscitation* **57,** 161–170 (2003).

21. Manole, M. D. *et al.* Magnetic resonance imaging assessment of regional cerebral blood flow after asphyxial cardiac arrest in immature rats. *J. Cereb. Blood Flow Metab.* **29,** 197–205 (2009).

22. Drabek, T. *et al.* Global and regional differences in cerebral blood flow after asphyxial versus ventricular fibrillation cardiac arrest in rats using ASL-MRI. *Resuscitation* **85,** 964–971 (2014).

23. Buunk, G., van der Hoeven, J. G. & Meinders, a E. Cerebral blood flow after cardiac arrest. *Neth. J. Med.* **57,** 106–12 (2000).

24. Lemiale, V. *et al.* Changes in cerebral blood flow and oxygen extraction during post-resuscitation syndrome. *Resuscitation* **76,** 17–24 (2008).

25. Pires, P. W., Dams Rabos, C. M., Martin, N. & Dorrance, A. M. The effects of hypertension on the cerebral circulation. *Am J Physiol Hear. Circ Physiol* **304,** H1598–H1614 (2013).

26. He, J. *et al.* Real-time monitoring of cerebral blood flow by laser speckle contrast imaging after cardiac arrest in rat. *Conf. Procedings IEEE Eng. Med. Biol. Soc.* 6971–6974 (2015). doi:10.14440/jbm.2015.54.A

27. Oddo, M. & Rossetti, A. O. Predicting neurological outcome after cardiac arrest. *Curr. Opin. Crit. Care* **17,** 254–259 (2011).

28. Chen, B. *et al.* Improved early postresuscitation EEG activity for animals treated with hypothermia predicted 96 hr neurological outcome and survival in a rat model of

cardiac arrest. *Biomed Res. Int.* **2013,** (2013).

29. Anstadt, M. P. *et al.* Pulsatile reperfusion after cardiac arrest improves neurologic outcome. *Ann. Surg.* **214,** 478-88; discussion 489-90 (1991).

30. O'Neil, M. P., Fleming, J. C., Badhwar, A. & Guo, L. R. Pulsatile versus nonpulsatile flow during cardiopulmonary bypass: Microcirculatory and systemic effects. *Ann. Thorac. Surg.* **94,** 2046–2053 (2012).

31. Salameh, A. *et al.* Protective Effects of Pulsatile Flow During Cardiopulmonary Bypass. *Ann. Thorac. Surg.* **99,** 192–199 (2015).

32. Aykut, K. *et al.* Pulsatile versus non-pulsatile flow to reduce cognitive decline after coronary artery bypass surgery: A randomized prospective clinical trial. *J. Cardiovasc. Dis. Res.* **4,** 127–129 (2013).

33. Allen, B. S., Ko, Y., Buckberg, G. D. & Tan, Z. Studies of isolated global brain ischaemia: III. Influence of pulsatile flow during cerebral perfusion and its link to consistent full neurological recovery with controlled reperfusion following 30 min of global brain ischaemia. *Eur. J. Cardio-thoracic Surg.* **41,** 1155–1163 (2012).

34. Dougherty, C. M. & Burr, R. L. Comparison of Heart Rate Variability Survivors and Nonsurvivors of Sudden Cardiac Arrest. *Am. J. Cardiol.* **70,** 441–448 (1992).

35. Brule, J. M. D. Van Den, Vinke, E. J., Loon, L. M. Van, Hoeven, J. G. Van Der & Hoedemaekers, C. W. E. Low spontaneous variability in cerebral blood flow velocity in non-survivors after cardiac arrest. *Resuscitation* **111,** 110–115 (2017).

36. Crouzet, C. *et al.* Cerebral blood flow is decoupled from blood pressure and linked to EEG bursting after resuscitation from cardiac arrest. *Biomed. Opt. Express* **7,** 4660–4673 (2016).

37. Obrenovitch, T. P., Chen, S. & Farkas, E. Simultaneous, live imaging of cortical spreading depression and associated cerebral blood flow changes, by combining voltage-sensitive dye and laser speckle contrast methods. *Neuroimage* **45,** 68–74 (2009).

38. Hinzman, J. M. *et al.* Inverse neurovascular coupling to cortical spreading depolarizations in severe brain trauma. *Brain* **137,** 2960–2972 (2014).

39. Jarvis, C. R., Anderson, T. R. & Andrew, R. D. Anoxic depolarization mediates acute damage independent of glutamate in neocortical brain slices. *Cereb. cortex* **11,** 249–59 (2001).

40. Mozaffarian, D. *et al. Heart disease and stroke statistics-2016 update a report from the American Heart Association*. *Circulation* **133,** (2016).

41. Schneider, A., Böttiger, B. W. & Popp, E. Cerebral resuscitation after cardiocirculatory arrest. *Anesth. Analg.* **108,** 971–979 (2009).

42. Mozaffarian, D. *et al. Heart disease and stroke statistics-2015 update : A report from the American Heart Association*. *Circulation* **131,** (2015).

43. Laver, S., Farrow, C., Turner, D. & Nolan, J. Mode of death after admission to an intensive care unit following cardiac arrest. *Intensive Care Med.* **30,** 2126–2128 (2004).

44. Soholm, H. *et al.* Prognostic value of electroencephalography (EEG) after out-of-hospital cardiac arrest in successfully resuscitated patients used in daily clinical practice. *Resuscitation* **85,** 1580–1585 (2014).

45. Robertson, C. S. Management of cerebral perfusion pressure after traumatic brain injury. *Anesthesiology* **95,** 1513–1517 (2001).

46. Ramirez-San-Juan, J. C., Ramos-García, R., Guizar-Iturbide, I., Martínez-Niconoff, G. & Choi, B. Impact of velocity distribution assumption on simplified laser speckle imaging equation. *Opt. Express* **16,** 3197–203 (2008).

47. Bruder, N., Pellissier, D., Grillot, P. & Gouin, F. Cerebral hyperemia during recovery from general anesthesia in neurosurgical patients. *Anesth. Analg.* **94,** 650–654; table of contents (2002).

48. Yang, X. Y., Zhou, S. J., Yu, Y. F., Shen, Y. F. & Xu, H. Z. Cerebral hyperaemia after isoflurane anaesthesia for craniotomy of patients with supratentorial brain tumour. *Acta Anaesthesiol. Scand.* **57,** 1301–1307 (2013).

49. Ludwig, K. A. *et al.* Using a common average reference to improve cortical neuron recordings from microelectrode arrays. *J. Neurophysiol.* **101,** 1679–1689 (2009).

50. Xu, Y., Liachenko, S. & Tang, P. Dependence of early cerebral reperfusion and long-term outcome on resuscitation efficiency after cardiac arrest in rats. *Stroke* **33,** 837–843 (2002).

51. Shaik, J. S. B. *et al.* 20-Hydroxyeicosatetraenoic Acid Inhibition by HET0016 Offers Neuroprotection, Decreases Edema, and Increases Cortical Cerebral Blood Flow in a Pediatric Asphyxial Cardiac Arrest Model in Rats. *J. Cereb. Blood Flow Metab.* **35,** 1757–63 (2015).

52. Hofmeijer, J., Tjepkema-Cloostermans, M. C. & van Putten, M. J. A. M. Burst-suppression with identical bursts: A distinct EEG pattern with poor outcome in postanoxic coma. *Clin. Neurophysiol.* **125,** 947–954 (2014).

53. Nadeau, K. P., Rice, T. B., Durkin, A. J. & Tromberg, B. J. Multifrequency synthesis and extraction using square wave projection patterns for quantitative tissue imaging. *J.*

Biomed. Opt. **20,** 116005 (2015).

54. Dunn, A. K. *et al.* Simultaneous imaging of total cerebral hemoglobin concentration, oxygenation, and blood flow during functional activation. *Opt. Lett.* **28,** 28 (2003).
55. Dunn, A. K., Devor, A., Dale, A. M. & Boas, D. A. Spatial extent of oxygen metabolism and hemodynamic changes during functional activation of the rat somatosensory cortex. *Neuroimage* **27,** 279–290 (2005).
56. Tsao, C. W. *et al.* Relations of arterial stiffness and endothelial function to brain aging in the community. *Neurology* **81,** 984–991 (2013).
57. Pase, M. P. *et al.* Association of Aortic Stiffness With Cognition and Brain Aging in Young and Middle-Aged Adults The Framingham Third Generation Cohort Study. *Hypertension* **67,** 513–519 (2016).
58. Gasecki, D. *et al.* Aortic Stiffness Predicts Functional Outcome in Patients. *Stroke* **43,** 543–544 (2012).
59. Papaioannou, V., Giannakou, M., Maglaveras, N., Sofianos, E. & Giala, M. Investigation of heart rate and blood pressure variability, baroreflex sensitivity, and approximate entropy in acute brain injury patients. *J. Crit. Care* **23,** 380–386 (2008).
60. Webb, A. J. S. *et al.* Increased cerebral arterial pulsatility in patients with leukoaraiosis: Arterial stiffness enhances transmission of aortic pulsatility. *Stroke* **43,** 2631–2636 (2012).
61. Wilson, R. H., Crouzet, C., Torabzadeh, M. & Bazrafkan, A. High-speed spatial frequency domain imaging of rat cortex detects dynamic optical and physiological properties following cardiac arrest and resuscitation. *Neurophotonics* **4,** 1 (2017).
62. Lee, D. E. *et al.* Neural correlates of consciousness at near-electrocerebral silence in

an asphyxial cardiac arrest model. *Brain Connect.* **7,** 172–181 (2017).

63. Ghijsen, M., Rice, T. B., Yang, B., White, S. M. & Tromberg, B. J. Wearable speckle plethysmography (SPG) for characterizing microvascular flow and resistance. *Biomed. Opt. Express* **9,** 3937–3952 (2018).

64. Regan, C. *et al.* Fiber-based laser speckle imaging for the detection of pulsatile flow. *Lasers Surg. Med.* **47,** 520–525 (2015).

65. Wang, D. *et al.* Fast blood flow monitoring in deep tissues with real-time software correlators. *Biomed. Opt. Express* **7,** 776 (2016).

66. Parthasarathy, A. B. *et al.* Dynamic autoregulation of cerebral blood flow measured non-invasively with fast diffuse correlation spectroscopy. *J. Cereb. Blood Flow Metab.* **38,** 230–240 (2018).

67. Shin, H. C., Jia, X., Nickl, R., Geocadin, R. G. & Thakor, N. V. A subband-based information measure of EEG during brain injury and recovery after cardiac arrest. *IEEE Trans. Biomed. Eng.* **55,** 1985–1990 (2008).

68. Jia, X. *et al.* Early electrophysiologic markers predict functional outcome asociated with temperature manipulation after cardiac arrest in rats. *Crit. Care Med.* **36,** 1909–1916 (2008).

69. Wilkens, H., Regelson, W. & Hoffmeister, F. S. The Physiologic Importance of Pulsatile Blood Flow. *N. Engl. J. Med.* **267,** 443–446 (1962).

70. Doepp, F., Reitemeier, J., Storm, C., Hasper, D. & Schreiber, S. J. Duplex sonography of cerebral blood flow after cardiac arrest-A prospective observational study. *Resuscitation* **85,** 516–521 (2014).

71. van den Brule, J. M. D., Vinke, E., van Loon, L. M., van der Hoeven, J. G. &

Hoedemaekers, C. W. E. Middle cerebral artery flow, the critical closing pressure, and the optimal mean arterial pressure in comatose cardiac arrest survivors-An observational study. *Resuscitation* **110,** 85–89 (2017).

72. Nakayama, Y., Tsumura, K., Yamashita, N., Yoshimaru, K. & Hayashi, T. Pulsatility of ascending aortic pressure waveform is a powerful predictor of restenosis after percutaneous transluminal coronary angioplasty. *Circulation* **101,** 470–472 (2000).

73. Mitchell, G. F. *et al.* Arterial stiffness, pressure and flow pulsatility and brain structure and function: The Age, Gene/Environment Susceptibility-Reykjavik Study. *Brain* **134,** 3398–3407 (2011).

74. Chuang, S. Y. *et al.* Blood Pressure, Carotid Flow Pulsatility, and the Risk of Stroke: A Community-Based Study. *Stroke* **47,** 2262–2268 (2016).

75. Sigal, I. *et al.* Imaging brain activity during seizures in freely behaving rats using a miniature multi-modal imaging system. *Biomed. Opt. Express* **7,** 3596–3609 (2016).

76. Dreier, J. P. *et al.* Terminal Spreading Depolarization and Electrical Silence in Death of Human Cerebral Cortex. *Ann. Neurol.* **83,** 295–310 (2018).

77. Dreier, J. P. The role of spreading depression, spreading depolarization and spreading ischemia in neurological disease. *Nat. Med.* **17,** 439–447 (2011).

78. Hartings, J. A. *et al.* The continuum of spreading depolarizations in acute cortical lesion development : Examining Leao's legacy. *J. Cereb. Blood Flow Metab.* **37,** 1571–1594 (2017).

79. Farkas, E., Bari, F. & Obrenovitch, T. P. Multi-modal imaging of anoxic depolarization and hemodynamic changes induced by cardiac arrest in the rat cerebral cortex. *Neuroimage* **51,** 734–742 (2010).

80. Shin, H. K. *et al.* Vasoconstrictive neurovascular coupling during focal ischemic depolarizations. *J. Cereb. Blood Flow Metab.* **26,** 1018–1030 (2006).

81. Bornstadt, D. Von *et al.* Supply-Demand Mismatch Transients in Susceptible Peri-infarct Hot Zones Explain the Origins of Spreading Injury Depolarizations. *Neuron* **85,** 1117–1131 (2015).

82. Balanca, B. *et al.* Altered hypermetabolic response to cortical spreading depolarizations after traumatic brain injury in rats Baptiste Balanc. *J. Cereb. Blood Flow Metab.* **37,** 1670–1686 (2016).

83. Hartings, J. A. *et al.* Spreading Depression in Continuous Electroencephalography of Brain Trauma. *Ann. Neurol.* **76,** 681–694 (2014).

84. Bosche, B. *et al.* Recurrent Spreading Depolarizations after Subarachnoid Hemorrhage Decreases Oxygen Availability in Human Cerebral Cortex. *Ann. Neurol.* **67,** 607–617 (2010).

85. Bolay, H. *et al.* Intrinsic brain activity triggers trigeminal meningeal afferents in a migraine model. **8,** 136–142 (2002).

86. Otori, T., Greenberg, J. H. & Welsh, F. A. Cortical Spreading Depression Causes a Long-Lasting Decrease in Cerebral Blood Flow and Induces Tolerance to Permanent Focal Ischemia in Rat Brain. *J. Cereb. Blood Flow Metab.* **23,** 43–50 (2003).

87. Lauritzen, M. *et al.* Persistent Oligemia of Rat Cerebral Cortex in the Wake of Spreading Depression. *Ann. Neurol.* **12,** 469–474 (1982).

88. Dreier, J. P. *et al.* Cortical spreading ischaemia is a novel process involved in ischaemic damage in patients with aneurysmal subarachnoid haemorrhage. *Brain* **132,** 1866–1881 (2009).

89. Dohmen, C. *et al.* Spreading Depolarizations Occur in Human Ischemic Stroke with High Incidence. *Ann. Neurol.* **63,** 720–728 (2008).

90. Crouzet, C. *et al.* Acute discrimination between superficial-partial and deep-partial thickness burns in a preclinical model with laser speckle imaging. *Burns* **41,** (2015).

91. Lauritzen, M. *et al.* Clinical relevance of cortical spreading depression in neurological disorders : migraine , malignant stroke , subarachnoid and intracranial hemorrhage , and traumatic brain injury. *J. Cereb. Blood Flow Metab.* **31,** 17–35 (2010).

92. Pham-huy, L. A., He, H. & Pham-huy, C. Free Radicals , Antioxidants in Disease and Health. *Int. J. Biomed. Sci.* **4,** 89–96 (2008).

93. Dunn, A. K., Bolay, H., Moskowitz, M. A. & Boas, D. A. Dynamic Imaging of Cerebral Blood Flow Using Laser Speckle. *J. Cereb. Blood Flow Metab.* **21,** 195–201 (2001).

94. Nakamura, H. *et al.* Spreading depolarizations cycle around and enlarge focal ischaemic brain lesions. *Brain* **133,** 1994–2006 (2018).